SEISMIC PROTECTION OF BRIDGE STRUCTURES USING SHAPE MEMORY ALLOY-BASED ISOLATION SYSTEMS AGAINST NEAR-FIELD EARTHQUAKES

A Dissertation

by

OSMAN ESER OZBULUT

Submitted to the Office of Graduate Studies of
Texas A&M University
in partial fulfillment of the requirements for the degree of

DOCTOR OF PHILOSOPHY

December 2010

Major Subject: Civil Engineering

Seismic Protection of Bridge Structures Using Shape Memory Alloy-Based Isolation Systems against Near-Field Earthquakes

SEISMIC PROTECTION OF BRIDGE STRUCTURES USING SHAPE MEMORY ALLOY-BASED ISOLATION SYSTEMS AGAINST NEAR-FIELD EARTHQUAKES

A Dissertation

by

OSMAN ESER OZBULUT

Submitted to the Office of Graduate Studies of
Texas A&M University
in partial fulfillment of the requirements for the degree of

DOCTOR OF PHILOSOPHY

Approved by:

Chair of Committee,	Stefan Hurlebaus
Committee Members,	Jose Roesset
	Monique Head
	Ibrahim Karaman
Head of Department,	John Niedzwecki

December 2010

Major Subject: Civil Engineering

ABSTRACT

Seismic Protection of Bridge Structures Using Shape Memory Alloy-Based Isolation Systems against Near-Field Earthquakes. (December 2010)

Osman Eser Ozbulut, B.S., Istanbul Technical University;

M.S., Texas A&M University

Chair of Advisory Committee: Dr. Stefan Hurlebaus

The damaging effects of strong ground motions on highway bridges have revealed the limitations of conventional design methods and emphasized the need for innovative design concepts. Although seismic isolation systems have been proven to be an effective method of improving the response of bridges during earthquakes, the performance of base-isolated structures during near-field earthquakes has been questioned in recent years. Near-field earthquakes are characterized by long period and large- velocity pulses. They amplify seismic response of the isolation system since the period of these pulses usually coincides with the period of the isolated structures.

This study explores the feasibility and effectiveness of shape memory alloy (SMA)-based isolation systems in order to mitigate the response of bridge structures against near-field ground motions. SMAs have several unique properties that can be exploited in seismic control applications. In this work, uniaxial tensile tests are conducted first to evaluate the degree to which the behavior of SMAs is affected by variations in loading rate and temperature. Then, a neuro-fuzzy model is developed to

simulate the superelastic behavior of SMAs. The model is capable of capturing rate- and temperature-dependent material response while it remains simple enough to carry out numerical simulations. Next, parametric studies are conducted to investigate the effectiveness of two SMA-based isolation systems, namely superelastic-friction base isolator (S-FBI) system and SMA/rubber-based (SRB) isolation system. The S-FBI system combines superelastic SMAs with a flat steel-Teflon bearing, whereas the SRB isolation system combines SMAs with a laminated rubber bearing rather than a sliding bearing. Upon evaluating the optimum design parameters for both SMA-based isolation systems, nonlinear time history analyses with energy balance assessment are conducted to compare their performances. The results show that the S-FBI system has more favorable properties than the SRB isolation system. Next, the performance of the S-FBI systems is compared with that of traditional isolation systems used in practice. In addition, the effect of outside temperature on the seismic response of the S-FBI system is assessed. It is revealed that the S-FBI system can successfully reduce the response of bridges against near-field earthquakes and has excellent re-centering ability.

DEDICATION

To my loving mother,

who believed in and supported me in everything that I have ever wanted to do

ACKNOWLEDGEMENTS

I would like to thank my advisor, Dr. Stefan Hurlebaus for providing me the opportunity to work with him and for his constant support and guidance throughout my study. I would like to also thank my committee members, Dr. Jose Roesset, Dr. Monique Head, and Dr. Ibrahim Karaman for their advice throughout the course of this research. I am also grateful to Dr. Paul Roschke for his support and encouragement since the beginning of my graduate study at Texas A&M University.

I also want to extend my gratitude to all of my friends for making me feel as at home as possible during my time in Bryan/College Station. Finally, I would like to thank my family for their infinite support, especially to my sisters, Sezen Kirtil and Esen Ozbulut for their encouragement given to me to continue my education overseas.

TABLE OF CONTENTS

Page

Page

Page

Page

LIST OF FIGURES

Page

Page

Page

Page

Page

Page

Page

LIST OF TABLES

Page

NOMENCLATURE

ABBREVIATIONS

AASHTO	American Association of State Highway and Transportation Officials
ANFIS	Adaptive Neuro-Fuzzy Inference System
CFPR	Carbon Fiber-Reinforced Polymer
ECC	Engineering Cementitious Composites
FIS	Fuzzy Inference System
FPS	Friction Pendulum System
IBC	International Building Code
LRB	Lead Rubber Bearing
MANSIDE	Memory Alloys for New Seismic Isolation and Energy Dissipation Devices
MTS	Material Testing System
NRB	Natural Rubber Bearing
P-F	Pure-Friction (isolation system)
PGA	Peak Ground Acceleration
RC	Reinforced Concrete
RHD	Reusable Hysteretic Damper
R-FBI	Resilient-Friction Base Isolator
S-FBI	Superelastic-Friction Base Isolator
SMA	Shape Memory Alloy

SRB	SMA/rubber-based (isolation system)

SYMBOLS

$a_{d\ max}$	Peak deck acceleration of isolated bridge
$a_{d\ max(ni)}$	Peak deck acceleration of non-isolated bridge
A_f	Austenite finish temperature
Al	Aluminum
A_s	Austenite start temperature
A_{SMA}	Cross-sectional area of SMA wires
B	Boron
Be	Beryllium
C	Carbon
c_1	Viscous damping coefficient of piers
c_b	Viscous damping coefficient of bearing
Co	Cobalt
Cu	Copper
E_A	Absorbed energy
E_H	Irrecoverable hysteretic energy
E_K	Absolute kinetic energy
$E_K^{'}$	Relative kinetic energy
E_I	Absolute input energy
$E_I^{'}$	Relative input energy

E_S	Elastic strain energy
E_{SMA}	Young's modulus of SMA wires
E_ξ	Damping energy
F_d	Design force of SMA device
Fe	Iron
F_o	Normalized yield strength
F_y	Yield strength
g	Gravity
k_1	Stiffness of piers
k_b	Initial stiffness of bearing
k_{SMA}	Initial lateral stiffness of SMA device
L_{SMA}	Length of SMA wires
m_1	Mass of pier
m_2	Mass of deck
M_d	Austenite stabilization temperature
M_f	Martensite finish temperature
Mn	Manganese
M_s	Martensite start temperature
Nb	Niobium
Ni	Nickel
R	Radius of the concave surface of FPS
Ta	Tantalum

T_b	Natural period of the isolated bridge
Ti	Titanium
T_{shift}	Additive period shift
u_1	Displacement of pier
u_2	Displacement of deck
$\ddot{u}_g$	Ground acceleration
u_d	Design displacement of SMA device
$u_{d\ max}$	Peak deck drift of the isolated bridge
$u_{d\ max(ni)}$	Peak deck drift of the non-isolated bridge
u_y	Yield displacement
$V_{b\ max}$	Peak base shear of the isolated bridge
$V_{b\ max(ni)}$	Peak base shear of the non-isolated bridge
W_d	Weight of the deck
Zn	Zinc
z	Hysteretic dimensionless quantity
α	Ratio of the post yielding to the elastic stiffness
ε_y	Yield strain of SMA wire
μ	Coefficient of friction

1. INTRODUCTION

1.1 Problem Description

Bridges play an important role in the transportation network on which goods and people are transported, and their failure will not only result in an interruption of this basic need but also impede the relief and rescue efforts. In recent years, the damaging effects of near-field motions on highway bridges have revealed the limitations of conventional design methods and emphasized the need of innovative design strategies. Numerous bridges were damaged or collapsed during the 1994 Northridge, 1995 Kobe, 1999 Duzce and 1999 Chi Chi earthquakes (Housner and Thiel, 1995; Bruneau, 1998; Roussis et al., 2003; Hsu and Fu, 2004). In the most recent 2008 Winchuan earthquake, many highway bridges were either severely damaged or completely collapsed in China, leading to not only significant economic losses but also large loss of lives due to the transportation supply disruption and the lack of access to medical care (Qiang *et al.*, 2009).

Seismic isolation has been the most commonly used method over the past years, although numerous strategies have been proposed, to improve the response of bridge structures during earthquakes (Ibrahim, 2008). Seismic isolation is essentially based on the idea of decoupling the support of a structure from the horizontal motions of the ground by placing flexible interfaces between the structure and its support. It reduces the

---

This dissertation follows the style of *Journal of Structural Engineering.*

lateral forces that act on the superstructure by shifting the fundamental period of the structure away from the predominant period of the ground motion and providing additional damping. A variety of devices including rubber isolation systems that combine laminated rubber bearings and some mechanical dampers as well as sliding-type isolation systems that filter out earthquake forces via the discontinuous sliding interfaces have been developed and used for seismic isolation.

Although seismic isolation systems have been proven to be an effective method of reducing seismic response of structures, the performance of base-isolated structures against near-field earthquakes has been questioned in recent years (Jangid and Kelly, 2001; Shen *et al.*, 2004; Liao *et al.*, 2004). Near-field earthquakes are characterized by long period and large velocity pulses in the velocity time history. Since the period of these pulses usually coincides with the period of isolated structures, ground motions with near-field characteristics amplify the seismic response of the isolation system. Another characteristic of the near-field motions that adversely influences base isolation systems is that the ground motion normal to the fault trace is richer in long-period spectral components than that parallel to the fault. Isolation bearings experience large deformations due to this normal component of the near-field motions (Deb, 2004). To accommodate large isolator displacements, the size of the isolation device and the required seismic gap significantly increases. Besides these requirements, the need for flexible utility connections adds extra cost (Panchal and Jangid, 2008). Furthermore, if an adequate seismic gap is not provided, undesirable pounding effects may occur.

In order to reduce large displacement response of isolated bridge structures during near-field earthquakes, several researchers have proposed the use of supplemental dampers. Some studies are focused on the use of passive devices for additional energy dissipation (Makris and Zhang, 2004; Soneji and Jangid, 2007; Dicleli, 2007), while a considerable number of studies have explored the effectiveness of semi-active devices for mitigating the response of isolated bridges (Erkus *et al.*, 2002; Iemura and Pradono, 2005; Guo *et al.*, 2009). However, a smart isolation system that can reduce the large isolation level deformations that are observed during near-field excitations while still offer the potential benefits of seismic isolation such as reductions in superstructure acceleration response and base shear is still being pursued by researchers.

1.2 Scope of Research

Over the past decade, shape memory alloys have received considerable attention as a smart material that can be employed in vibration control of civil structures (DesRoches and Smith, 2004; Song et al., 2006). SMAs are a class of metallic alloys that can recover their original shape after experiencing large strains. This study explores the feasibility and effectiveness of SMA-based isolation systems in order to mitigate the response of bridge structures against near-field ground motions. Seismic isolation systems are typically rubber-based bearings or sliding-type bearings. Rubber isolation bearings have considerable lateral flexibility and lengthen the natural period of the structure in order to avoid resonance with the predominant frequency contents of the ground motions, while sliding-type bearings provide discontinuous sliding interfaces to

filter out lateral forces exerted by an earthquake. In general, a favorable isolation device should have (i) adequate energy dissipation capacity to reduce seismic demand on piers, (ii) a good re-centering mechanism to avoid excessive bearing deformations and instability, (iii) no need for bearing replacement even after a strong earthquake (i.e., no residual deformation on the bearing after the excitation), and (iv) high durability against cyclic loads. SMAs have considerable energy dissipation capacity and re-centering ability that can be exploited for use in a base isolation system. Moreover, superelastic SMAs can fully recover their deformations after an excitation and have substantial resistance to fatigue and corrosion.

Although the appealing properties of SMAs suggest that an SMA-based seismic isolation device can accomplish the above-mentioned auspicious isolator characteristics, there is a need for a comprehensive study to prove this idea by addressing several questions such as (1) What are the influences of dynamic loading and outside temperature on the behavior of SMAs, (2) Can a simple, accurate, and computationally efficient model for simulating the mechanical response of SMAs considering rate- and temperature-dependence be developed, (3) What are the optimal parameters for an SMA-based isolation system, (4) Is a rubber-based or a sliding-based SMA isolation system more viable, (5) How does the temperature dependence of mechanical response of SMAs affect the seismic performance of the SMA-based isolation systems?

The objective of this dissertation is to address the concerns and problems presented above with reference to the use of SMAs as an isolation system component for seismic protection of bridge structures against near-field earthquakes.

1.3 Organization of the Dissertation

This dissertation is organized into the following sections:

Section 1 presents the description of research problem and the scope of the research.

Section 2 provides a concise overview of mechanical properties of shape memory alloys and modeling techniques for SMAs. Also, a comprehensive literature review is presented for passive vibration control applications using SMAs.

Section 3 presents tensile tests conducted to evaluate the effects of temperature, strain rate, and strain amplitude on mechanical behavior of superelastic NiTi wires.

Section 4 discusses the neuro-fuzzy modeling of temperature- and rate-dependent behavior of superelastic NiTi SMAs.

Section 5 investigates the optimum design parameters of a superelastic-friction base isolator (S-FBI) that consists of a steel-Teflon sliding bearing and a superelastic SMA device for seismic protection of bridges subjected to near-field earthquakes.

Section 6 explores the effectiveness of an SMA/rubber-based (SRB) isolation system that consists of a laminated rubber bearing and an SMA device for protecting highway bridges against near-field earthquakes.

Section 7 compares the performances of the superelastic-friction base isolator and the SMA/rubber-based isolation system using energy-based concepts.

Section 8 presents a comparative study of the performances of various isolation systems such as lead rubber bearings, friction pendulum system, resilient-friction base

isolators and the superelastic-friction base isolators for a multi-span continuous bridge under near-field ground motions.

Section 9 explores the effects of temperature on the performance of the superelastic-friction base isolator at length.

Section 10 presents conclusions along with recommendations for the use of SMAs as a seismic isolation component based on the findings of this study.

2. SHAPE MEMORY ALLOYS: AN OVERVIEW

2.1 Introduction to Shape Memory Alloys

The term smart materials usually refers to materials that have unique and interesting characteristics and can be employed in conventional structural design to improve performance of the structure. Shape memory alloys are a smart class of metals that exhibit several extraordinary properties. SMAs have two main phases which have different crystal structure. One is called *martensite* that is stable at low temperatures and high stresses and the other is called *austenite* that is stable at high temperatures and low stresses. Austenite, also named as parent phase, generally has a cubic crystal structure while martensite has a less-ordered crystal structure. Martensite can exist in two forms depending on crystal orientation direction: *twinned* (self-accommodated) martensite or *detwinned* martensite. Figure 2-1 shows schematic representation of different phases of shape memory alloy materials. The key characteristic of SMAs is a result of reversible phase transformations between martensite and austenite phases. These solid-to-solid phase transformations, called martensitic transformations, occur by shear lattice distortion with no diffusive process involved. The transformations can be temperature-induced (shape memory effect) or stress-induced (superelasticity).

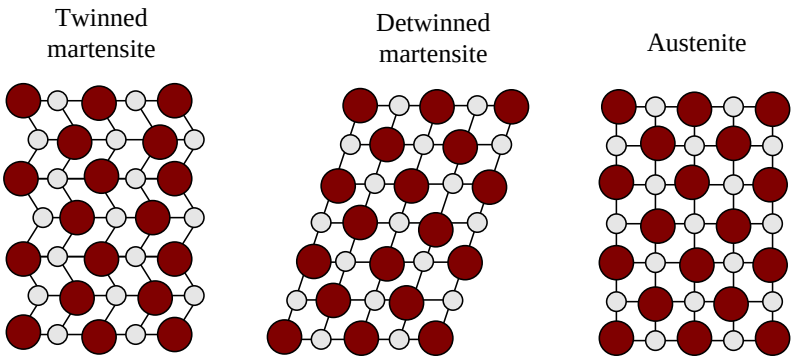

Figure 2-1 Different phases of shape memory alloys

Figure 2-2 illustrates the martensite fraction in an SMA material as a function of temperature in the absence of applied stress. There are four characteristic temperatures at which phase transformations occur: (1) the austenite start temperature A_s, where the material starts to transform from twinned martensite to austenite, (2) austenite finish temperature A_f, where the material is completely transformed to austenite, (3) martensite start temperature M_s, where austenite begins to transform into twinned martensite, (4) martensite finish temperature M_f, where the transformation to martensite is completed. Note that all of these transformation temperatures would increase with applied stress.

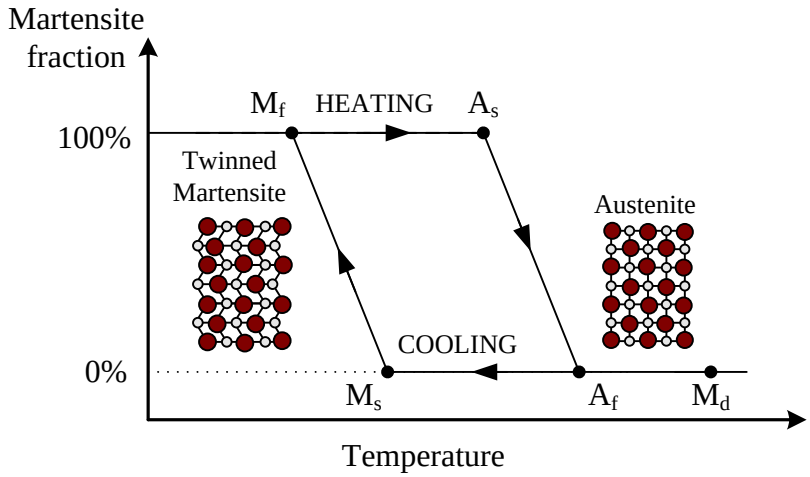

Figure 2-2 Martensite fraction-temperature diagram of SMAs

2.1.1 Shape Memory Effect

Shape memory effect is the ability of SMA material to recover its original shape after being deformed through a thermal cycling. If the temperature is below M_f, the SMA is in its twinned martensite phase. When a stress above a critical level is applied, the material transforms into detwinned martensite phase and retains this phase upon the removal of the load. It can regain its initial shape when the SMA material is heated to a temperature above A_f. Heating the material above A_f results in the formation of the austenite phase and a complete shape recovery. By a subsequent cooling, the SMA transforms to initial twinned martensite phase without any residual deformation. Figure 2-3 illustrates the shape memory effect on a stress-strain curve and a temperature diagram.

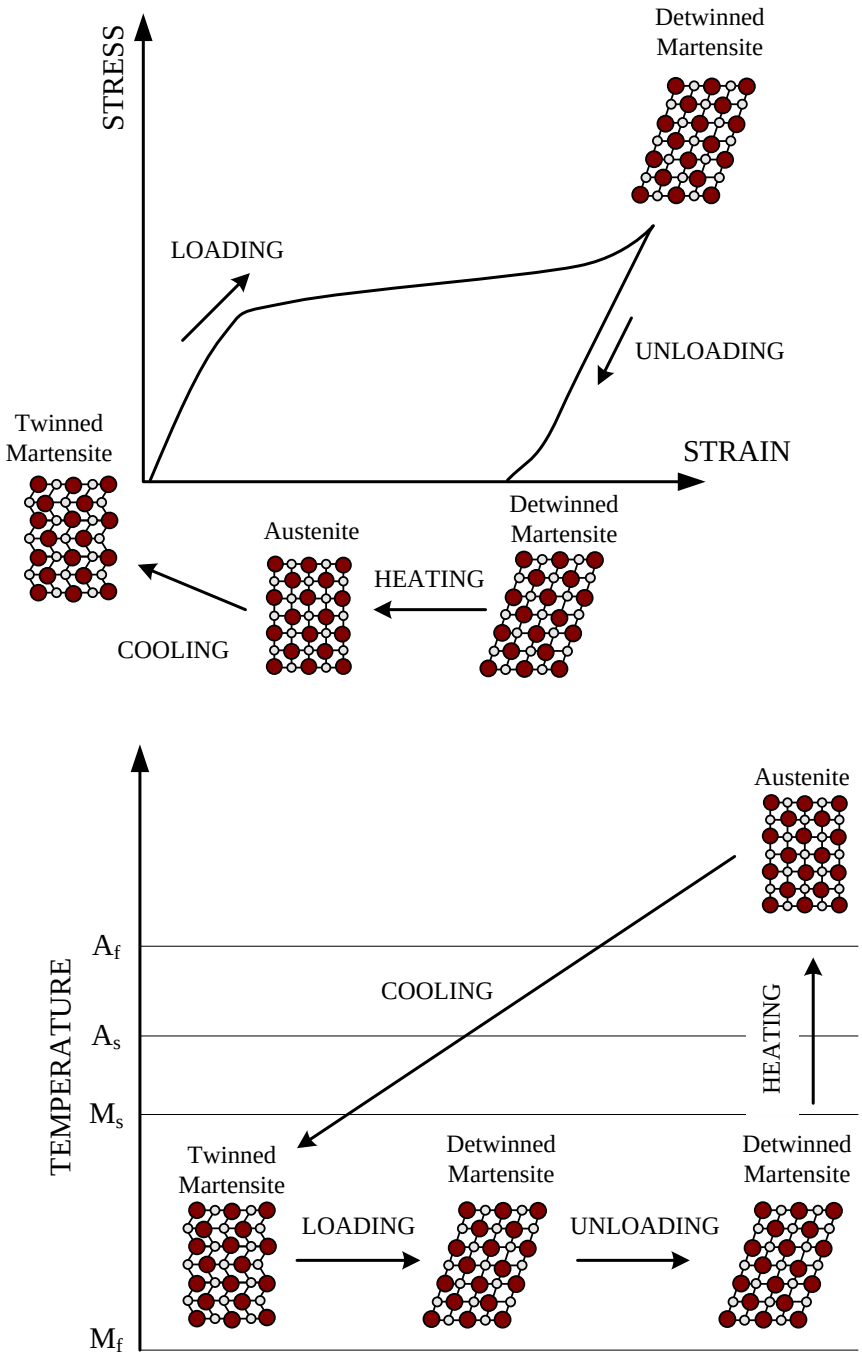

Figure 2-3 Shape memory effect

2.1.2 Superelastic Effect

Superelastic effect is described as the recovery of large strain as a result of the stress-induced martensitic phase transformations under constant temperature. SMA is in its austenite phase at relatively high temperatures (temperatures above A_f). When a sufficiently high stress is applied to the material in the austenite phase, the SMA transforms into the detwinned martensite. When the load is released, a reverse transformation to the austenite state takes place which results in complete shape recovery and a substantial hysteretic loop. A stress-strain curve and a temperature diagram demonstrating superelastic effect of SMAs are shown in Figure 2-4. Note that if the temperature is below A_f but above A_s, there will be only a partial shape recovery. Also, if the temperature is above a critical temperature named M_d, the material is stabilized in the austenite phase and the martensitic transformations cannot be induced by an applied load.

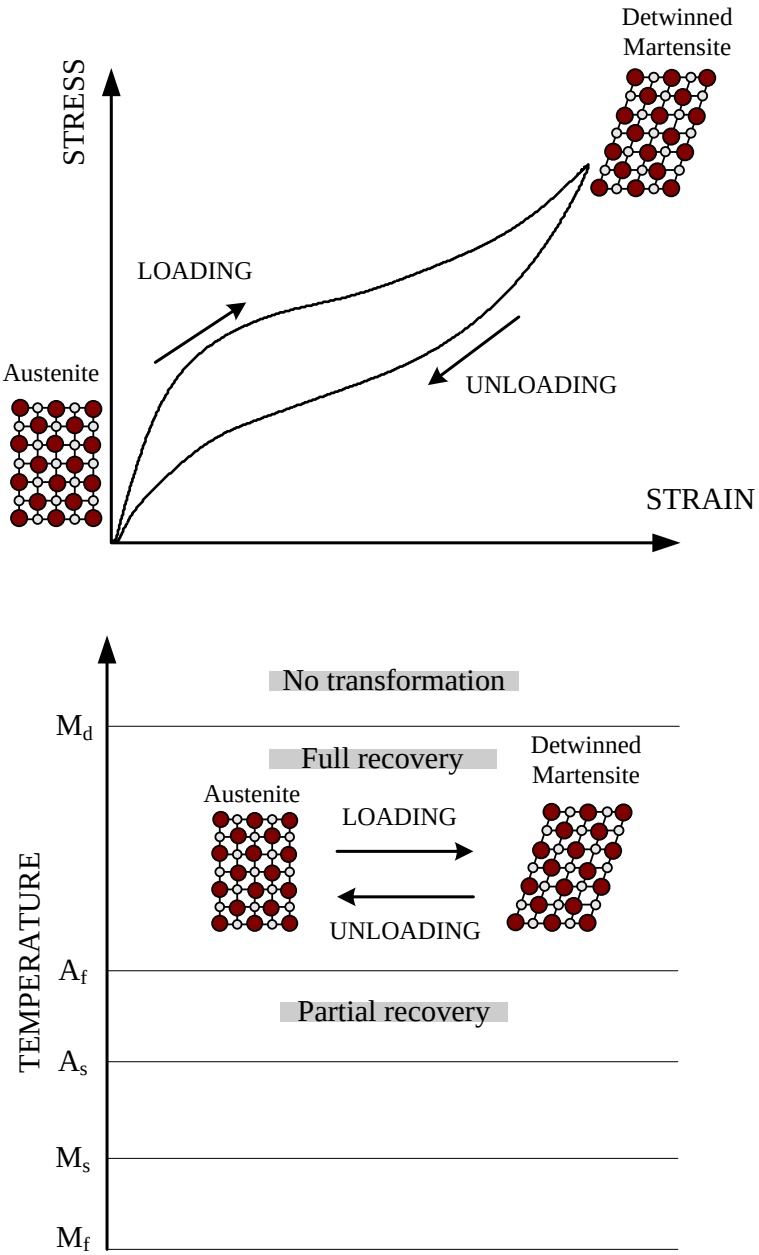

Figure 2-4 Superelastic effect

2.1.3 Commonly-used Shape Memory Alloys

Since the discovery of nickel-titanium (*NiTi*) in 1963, a large number of alloys have been investigated for shape memory behavior. However, two alloy systems, NiTi-based alloys and copper (Cu)-based alloys, have been mostly used in commercial applications in the past decades. Iron-based alloys have also attracted the interest of researchers in recent years.

2.1.3.1 NiTi-based alloys

Among various SMA compositions, the NiTi alloy has been the most widely studied and has become the most important material for commercial applications. This binary system is based on an almost equiatomic compound of nickel and titanium. Increasing the nickel composition above 50 atomic percentage (at.%) decreases the transformation temperature. Hence, the range of phase transformation temperatures can be adjusted by altering the composition of the alloys. The NiTi can achieve fully recoverable strains up to 8% and can be obtained in various forms such as wires, bars, tubes and plates. One of the important characteristics of the NiTi alloy is its excellent corrosion resistance. This feature of NiTi alloys together with their biocompatibility aspects has lead to the use of NiTi in various medical applications.

The addition of a third metal to NiTi to compose a ternary can result in desirable properties for specific applications. For example, *NiTiCu* has lower hysteresis associated with phase transformations, which makes them a better choice for actuator applications. On the other hand, the addition of Niobium (Nb) to the NiTi results in wider thermal hysteresis. The alloy *NiTiNb* shows minimal response to large

temperature changes and is preferred for coupling applications. It is also possible to obtain SMAs for applications operating at high temperatures by adding a third element such as palladium, platinum, hafnium and gold to the NiTi. In this way, transformation temperatures can be shifted anywhere in the range of 100-800 °C (Lagoudas, 2008).

2.1.3.2 Copper-based alloys

The copper-based alloys have the advantage that they are composed of relatively cheap materials and it is easier to machine them. However, because of the larger demand for NiTi alloys from industry, especially for biomedical devices, the price of the NiTi has decreased considerably over the past decade. Also, the recoverable strains for Cu-based alloys are limited to 2-4% strain levels and they have a long term aging problem at room temperatures due to martensite stabilization. The main Cu-based alloys are based on the binary alloys *CuAl* and *CuZn*. Among the commercially available Cu-based alloys, *CuZnAl* has the largest ductility whereas *CuZnNi* is less sensitive to aging effect and stabilization. The transformation temperatures of these alloys can be altered by varying the aluminum or nickel content. Although the transformation temperatures of NiTi alloys can also be adjusted by alloying and thermomechanical treatments, Cu-based alloys tend to have somewhat higher temperature range of transformation. For example, *CuAlBe* alloy exhibits superelastic behavior at a temperature range of -65 °C to 180 °C, which make them attractive for outdoor seismic application in cold regions. Recently, several researches investigated *CuAlMn*-based SMAs for enhanced ductile behavior and shape memory properties (Sutou *et al.*, 2008).

2.1.3.3 Iron-based alloys

As an alternative to NiTi-based alloys and copper-based alloys, ferrous SMAs such as *FeMnSi, FeNiC* and *FeNiCoTi* have been developed due to their lower cost. However, a ferrous alloy that exhibit superelastic effect at room temperature was not available until most recently. Tanaka *et al.* (2010) obtained a ferrous alloy showing a superelastic strain up to 15% at room temperature. The composition of the alloy is Fe-28Ni-17Co-11.5Al-2.5Ta-0.05B at.%, and the alloy is named as NCATB. The alloy has a tensile strength over 1 GPa. Also, austenite finish temperature A_f of the NCATB is -62 °C, which indicates a superelastic SMA device made of NCATB can be used safely in cold regions for outdoor seismic applications. Once the NCATB alloy is commercialized, the unique characteristics of the alloy such as high strength, large superelastic strain and high damping capacity might be exploited in various applications.

2.2 Mechanical Characteristics of Shape Memory Alloys

Since most of the seismic applications of SMAs rely on the superelastic effect of the SMAs, the mechanical properties of the superelastic SMAs are discussed in this section. The sensitivity of these properties to various factors such as temperature, strain rate, cyclic loading, and thermomechanical treatment is also examined. The superelastic SMAs that are considered for civil engineering applications includes the NiTi alloy and the Cu-based alloys. The mechanical characteristics of these alloys are discussed separately below.

2.2.1 Characteristics of NiTi Alloy

NiTi shape memory alloys have appealing mechanical characteristics such as considerable energy dissipation capacity, excellent re-centering ability, high strength, good fatigue resistance and high corrosion resistance. However, there are a number of parameters that influence the mechanical properties of the NiTi SMAs. Therefore, a complete understanding of the mechanical behavior of the NiTi is required before employing it in seismic applications. Many researchers have conducted experiments to investigate the mechanical characteristics of superelastic NiTi SMAs. The following discussion outlines the effects of cyclic loading, strain-rate and temperature on the behavior of the NiTi SMA.

2.2.1.1 Cycling loading

Due to the cyclic nature of the seismic loads, it is important to characterize the behavior of SMAs under repeated loading conditions. Some researchers have studied the effect of cyclic loading on NiTi wires with a diameter of 1-2 mm (Wolons *et al.*, 1998; Dolce and Cardone, 2001; Gall et al., 2001; Tamai and Kitagawa, 2002; DesRoches *et al.*, 2004; Malecot *et al.*, 2006). They found that there is a considerable decrease in forward phase transformation stress level with the number of loading cycles. Specifically, the greatest variation was noted between the first and second cycle. The reason for this reduction in forward transformation stress resides in small levels of localized slip that assist the forward transformation (DesRoches *et al.*, 2004). No significant variation or only a slight decrease was observed in the reverse transformation stress. Therefore, hysteresis loop area, i.e. the dissipated energy reduces with increasing

number of loading cycles. Another effect of the cyclic loading is the increase in residual deformation. However, the material tends to have a stabilized behavior after a given number of cycles. Figure 2-5 shows the stress-strain curves for the cyclic tensile tests performed on 2 mm diameters NiTi wires (Malecot *et al.*, 2006).

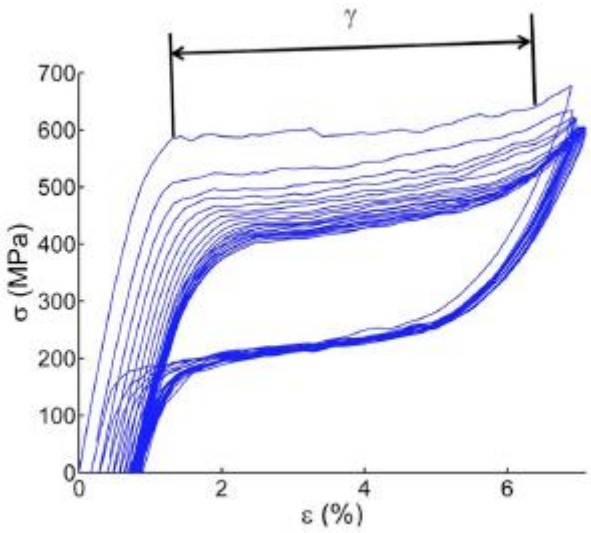

Figure 2-5 Results of cyclic tensile tests on NiTi wires (Malecot *et al.*, 2006)

The cyclic behavior of large diameter NiTi bars has been also investigated by several researchers. McCormick *et al.* (2007b) carried out experimental tests on 12.7 and 19.1 mm bars. DesRoches *et al.* (2004) tested 25.4 mm diameter bar. Similar results were obtained for bars as compared to the cyclic behavior of wires. Nevertheless, smaller reductions in forward transformation stress were observed for bars.

2.2.1.2 Strain rate effects

Although martensitic phase transformations are time-independent phenomena, experimental tests conducted at different loading rates have revealed that the strain rate has a significant influence on the mechanical behavior of NiTi shape memory alloys. The reason of the rate-dependent behavior is complex coupling between stress, temperature and rate of heat generation during stress induced phase transformations (Azadi et al, 2006). During the forward phase transformations, the material releases energy in the form of heat, while it absorbs energy in the case of unloading. The material may not have enough time to transfer latent heat to the environment during loading with high strain rates. As a result, the temperature of the material changes and this, in turn, alters the shape of the hysteresis loops and the transformation stresses (Wu *et al.*, 1996).

In the past studies, different conclusions were made about the effect of loading rate on the transformation stresses and the energy dissipated. Wolons *et al.* (1998) and Ren *et al.* (2007) reported an increase in the reverse transformation stress without a significant change in the forward transformation stress and a decrease in the energy dissipated with the increased strain rates. Dolce and Cardone (2001) and DesRoches *et al.* (2004) noticed an increase in both forward and reverse transformation stresses with increasing strain rates. Since smaller increases were observed in the forward transformation stress, a reduction in the energy dissipated was reported. On the other hand, Tobushi *et al.* (1998) observed a decrease in the reverse transformation stress and an increase in the forward transformation stress, which resulted in larger energy

dissipation for higher strain rates. Dayananda and Rao (2008) found that hysteresis loop shifts upward and the energy dissipated increases with increase in strain rates. Soul *et al.* (2010) reported that the dissipated energy slightly increases for a low frequency region (for frequencies less than 0.05 Hz), whereas it considerably decreases for a high frequency region (for a frequency range of 0.05 Hz -3 Hz).

The inconsistency in the findings of the previous studies about the strain rate effects on the superelastic behavior of NiTi SMAs can be attributed to factors such as using materials with different composition, testing at various ranges of strain rates, and experimental conditions. Since the SMA material employed in seismic applications will be subjected to dynamic effects, it is important to evaluate the effect of strain rate on the material used before actual application.

2.2.1.3 Temperature effects

Since phase transformations of SMAs are not only dependent on mechanical loading but also on temperature, change in the temperature significantly affects superelastic behavior of NiTi wires. Note that it is not only the testing temperature that influence the behavior but also its position with respect to transformation temperatures. A number of experimental studies have been conducted to investigate the effects of temperature on superelastic SMAs (Piedboeuf *et al.*, 1998; Dolce and Cardone, 2001; Chen and Song, 2006; Churchill *et al.*, 2009). It was reported that the critical stress that initiates the phase transformation noticeably changes with temperature. In particular, an increase in temperature corresponds to a linear increase in transformation stress. Also, it was found that the equivalent viscous damping linearly decreases with an increase in the

temperature. Figure 2-6 illustrates stress-strain curves of superelastic NiTi wires that were tested at various temperatures by Chang *et al.* (2006). Note that the superelastic behavior was observed in responses above 0 °C, and residual strains occurred in responses above 40 °C for the material tested. The upward shift of the hysteresis curves as temperature increases can clearly be seen in the figure.

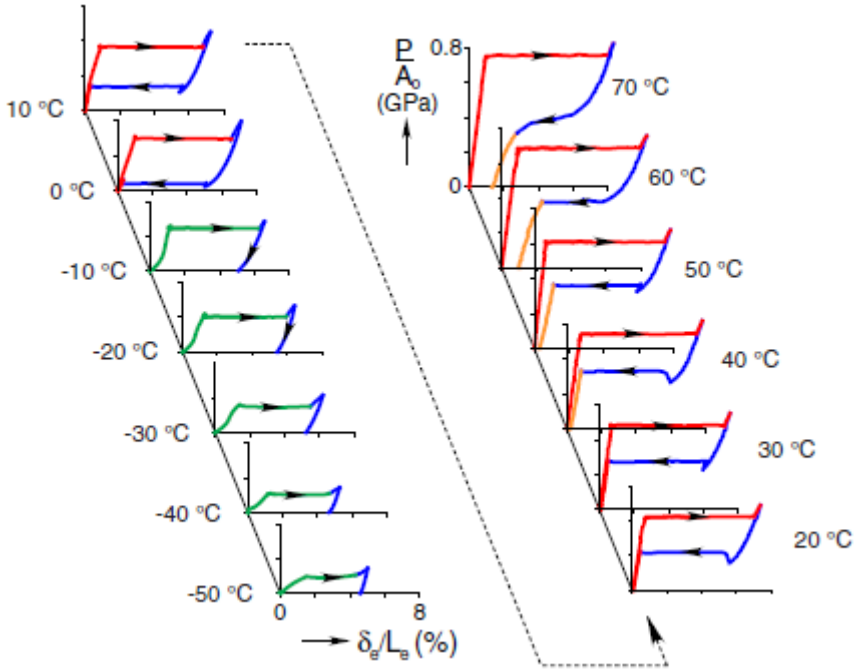

Figure 2-6 Stress-strain curves of NiTi wires at different temperatures (Churchill *et al.*, 2009)

2.2.2 Characteristics of Cu-based Alloys

Since the Cu-based alloys are cheaper and easier to machine, superelastic Cu-based SMAs with various compositions have been characterized by several researchers. Nevertheless, only a few of them have been investigated for potential seismic

applications. Among them, *CuZnAlNi* shape memory alloy bars were explored by Moroni *et al.* (2002) for their use as energy dissipation device. They conducted cyclic tests under tension-compression loading and evaluated their damping properties. However, the *CuAlBe* alloy has been the most commonly considered Cu-based SMA for seismic applications. The effects of cycling loading, strain rate, temperature and grain size on mechanical properties of the superelastic CuAlBe alloy are discussed below.

2.2.2.1 Cycling loading

The effect of cyclic loading on mechanical response of the CuAlBe wires has been studied by a number of researchers (Casciati and Faravelli, 2004; Montecinos *et al.*, 2006; Ozbulut *et al.*, 2007; Zhang *et al.*, 2008; Torra *et al.*, 2009). It was found that there is a decrease in forward transformation stress and hysteresis loop area with increasing number of loading cycles. However, it was reported that a stable behavior can be obtained after the first 10 load cycles. Also, no remnant strain occurred after many series of loading cycles. In a most recent study, Casciati and Marzi (2010) conducted an exhaustive set of experimental tests to investigate the fatigue lifetime of the CuAlBe SMAs for seismic applications. They concluded that the fatigue life of the CuAlBe is strongly dependent to the thermo-mechanical history of the material and strain amplitude. The fatigue life of the specimens subjected to a preliminary thermo-mechanical treatment was found to be satisfactory for strain amplitudes below 3%. Also, a reduced fatigue life was recorded for the specimens tested at higher temperatures.

2.2.2.2 Strain rate effects

Studies that explore the effects of strain rate on mechanical properties of CuAlBe SMAs have remained few in number. Among them, Malecot *et al.* (2006) performed tensile tests at four different strain rates, Araya *et al.* (2008) carried out cyclic tests at three different frequencies and Zhang *et al.* (2008) tested the CuAlBe wires at two different loading rates. No significant influence of strain rate on the shape of hysteresis curve and energy dissipation capacity was reported in the findings of these studies.

2.2.2.3 Temperature effects

Several studies have been conducted to evaluate the influence of temperature on the mechanical response of the CuAlBe alloys (Torra *et al.*, 2004; Araya *et al.*, 2008; Casciati and van der Eijk, 2008). In such a study, Ozbulut *et al.* (2007) carried out tensile tests on the CuAlBe wires at 0 °C, 25 °C, and 50 °C. They found that modulus of elasticity, secant stiffness and phase transformation stresses increase with increasing temperature. Also, a decrease in equivalent viscous damping was observed as the temperature increases. Zhang *et al.* (2008) investigated the behavior of the CuAlBe SMAs at cold temperatures. In particular, they compared the behavior of the CuAlBe wires tested at -50 °C, -25 °C, 0 °C and 23 °C. They reported a slight decrease in equivalent viscous damping and an increase in forward transformation stress for higher temperatures. No clear pattern for the variation of elasticity modulus with temperature was observed. Figure 2-7 illustrates the dependence of mechanical behavior of the CuAlBe wires on temperature.

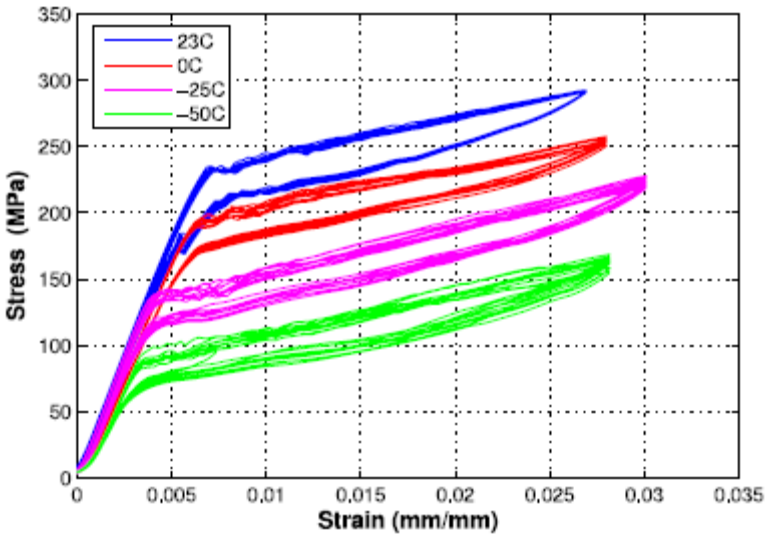

Figure 2-7 Stress-strain curves of CuAlBe wires at different temperatures (Zhang *et al.*, 2008)

2.2.2.4 Grain size effects

The size, shape, and crystallographic orientation of grains have a considerable influence on the superelastic behavior of Cu-based SMAs. The grain size in Cu-based SMAs is of larger magnitude than that for NiTi alloys. Therefore, elastic stress concentrations on grain boundaries are easily relaxed by plastic deformation in NiTi whereas elastic stress concentrations easily occur at grain boundaries of Cu-based alloys. This is why the mechanical behavior of NiTi alloy is only slightly influenced by grain size and orientation. On the contrary, large grain sizes cause intergranular brittle fractures in Cu-based SMAs due to stress concentrations on grain boundaries (Brailovski *et al.*, 2003).

Araya *et al.* (2008) investigated grain size effects on the mechanical behavior of the CuAlBe SMA wires. They found that the maximum stress and forward

transformation stress increase as the grain size decreases. Also, an increase in equivalent viscous damping was present with increased grain size. Similarly, Boroschek *et al.* (2007) found that a coarse grain size leads to smaller secant stiffness and higher energy loss for the CuAlBe alloys. However, very large grain sizes cause brittle fracture and need to be avoided.

2.3 Modeling of Shape Memory Alloys

In order to explore all potential applications of SMAs, a reliable model that describes highly complex behavior of the material has been pursued by many researchers. SMA models have been developed by either following a microscopic or a macroscopic approach. The first approach actually aims to describe phenomena in either microscopic or mesoscopic level. At microscopic level, models employ continuum mechanics to relate deformation, strain, and stress at particular points for a small material volume. The models that describe the behavior of SMA at mesoscopic level also use continuum mechanics as main description tool but combine it with multiscale modeling. The microscopic approach has been studied in the work of many researchers such as Sun and Hwang (1993), Goo and Lexcellent (1997), Levitas *et al.* (1998), Patoor *et al.* (1998), Hall and Govindjee (2002).

Macroscopic models attempt to capture the SMA response at the macroscopic level using phenomology. Some of these models rely heavily on thermodynamic principles, while others are developed by setting material constants of a model to match experimental data. A large number of macroscopic models have been proposed to

capture mechanical response of SMA due to their simplicity and relative accuracy (Boyd and Lagoudas, 1996; Liang and Rogers, 1990; Auricchio and Lubliner, 1997; Auricchio, 2001; Ikeda *et al.*, 2004). This section does not aim to provide an exhaustive review of all models that describe constitutive behavior of SMAs in the existing literature. Rather, it introduces some of the constitutive models of superelastic SMAs that have been proposed to describe the behavior of SMA in seismic applications.

One of the first models developed to explore potential use of SMAs as a passive damping device was presented by Graesser and Cozzarelli (1991). They modified a one-dimensional model of hysteresis to allow for the simulation of hysteresis behavior of SMAs. This model is capable of both shape memory effect and superelastic effect but does not incorporate loading rate and temperature effects.

Wilde *et al.* (2000) extended the Graesser–Cozzarelli model to incorporate strain hardening behavior of SMAs after phase transformation completion. The model was further improved by Zhang and Zhu (2007) for better numerical stability and computation efficiency. However, these models still did not consider rate and temperature effects.

Ren *et al.* (2007) modified the Graesser–Cozzarelli model to capture the strain-rate-dependent hysteretic behavior of superelastic SMA wires. The proposed model divides the hysteresis loop into three parts and employs different parameters for each part.

Brinson (1993) proposed a one-dimensional constitutive model to describe both shape memory and superelastic effects of SMAs. The formulation of the model is based

on an internal variable approach with the assumption of non-constant material functions. The Brinson model was modified by Sun and Rajapakse (2003) and Prahlad and Chopra (2003) to consider frequency dependent behavior of SMAs.

Another model that has been frequently used to represent SMAs in seismic applications was introduced by Fugazza (2005). It is a modified version of a uniaxial constitutive model proposed by Auricchio and Sacco (1997). The model is simple enough to implement into simulations and capable of reproducing partial and complete transformation patterns. However, drawbacks of the model are rate- and temperature-independence and assumption of same elastic properties between austenite and martensite.

Auricchio *et al.* (2007) studied a viscous model that is based on the inclusion of a direct viscous term in the evolutionary equation for the martensite fraction in order to account for strain rate effects on the response of superelastic SMAs. In another study, they proposed a thermomechanical model that considers actual martensite fraction as single variable (Auricchio et al, 2008). This model is also rate-dependent and has the ability to account for elastic properties between austenite and martensite.

Zhu and Zhang (2007a) focused on a thermomechanical constitutive model to simulate rate-dependent behavior of superelastic SMAs. The derivation of the model is based on a mechanical law, an energy balance equation and a transformation kinetics rule. The model was able to predict stress-strain curves of SMAs reasonably well under various loading rates, yet it was temperature-independent.

One of the very few models that considers both rate- and temperature dependent behavior of SMAs was proposed by Motahari and Ghassemieh (2007). The formulation of the model is based on Gibbs free energy and the volume fraction of detwinned martensite. The model uses an evolution function which describes the relationship between stress and strain with linear segments. This makes the implementation of the model easier in numerical analyses.

2.4 Seismic Applications of Shape Memory Alloys

Many researchers have explored the use of SMAs in a wide range of seismic applications. Although a few researchers have investigated the shape memory effect for active vibration control techniques (Shahin *et al.*, 1997; McGavin and Guerin, 2002), the SMAs considered most widely for structural applications do not involve heating and active control but, rather, exhibit the superelastic effect. Besides possessing unique re-centering ability and considerable energy dissipating capacity, superelastic SMAs have also favorable properties such as the ability to undergo large deformations, good fatigue resistance and excellent corrosion resistance. In this section, a comprehensive review is provided for passive vibration control applications using SMAs.

2.4.1 Applications to Buildings

2.4.1.1 SMA-based devices

Shape memory alloy-based devices have been studied by a large number of researchers for vibration control of building structures (Krumme *et al.*, 1995; Higashino and Aizawa, 1996; Salichs *et al.*, 2001; Suduo *et al.*, 2007; Zuo *et al.*, 2008). Clark *et*

al. (1995) designed two different types of dampers using SMAs. The configuration of their devices consists of multiple loops of superelastic wire wrapped around cylindrical support posts. The first design type utilizes a single layer of 100 loops of NiTi wire, while the second configuration uses 70 loops of pre-tensioned wires in three layers. The reduced-scale devices were tested to characterize the behavior of the devices at different temperatures and loading frequencies. Also, numerical analysis of a six story steel frame equipped with the SMA damper was performed. Aizawa *et al.* (1998) further investigated the performance of the SMA damper developed by Clark *et al.* (1995) under earthquake excitations by performing shake table tests on the six story steel frame studied earlier.

Dolce *et al*. (2000) developed an SMA-based passive control device that is intended to serve as a bracing system in buildings or isolation devices for buildings and bridges as the final product of a European research project, named MANSIDE project (Memory Alloys for New Seismic Isolation and Energy Dissipation Devices). The device employs pre-tensioned superelastic wires that are placed on the device so that they are only strained in tension for re-centering capability and supplemental martensitic bars or austenitic wires used for additional energy dissipation. By changing the number and characteristics of the two groups of SMA elements, the desired performance of the device can be accomplished. Experimental tests of the full-scale prototype of braces and isolation devices were carried out to demonstrate the capability of the device.

Han *et al.* (2005) developed an SMA damper that can simultaneously work in tension, compression and torsion. The damper utilizes superelastic NiTi wires that are

subjected to tensile strains for all loading cases. To verify effectiveness of the damper for tensile, compressive and torsional motion, analytical and experimental studies were carried out on three reduced-scale dampers.

Ma and Cho (2008) proposed an SMA-based damper that consists of pre-tensioned superelastic SMA wires which provide energy dissipation capacity and two pre-compressed springs which supply restoring force. Numerical studies were conducted to validate the expected behavior of the device. The results revealed that a 1-meter-long damper can attain an equivalent damping ratio of 12% with a displacement stroke of 30 mm and full re-centering capability. Van de Lindt and Potts (2008) proposed an SMA-based device as shown in Figure 2-8 for mitigating seismic response of wood frame structures. The device consists of an inner tube and an outer tube. Two studs are connected to the inner tube and one stud is connected to the outer tube. The SMA wires were installed between these studs and prestrained.

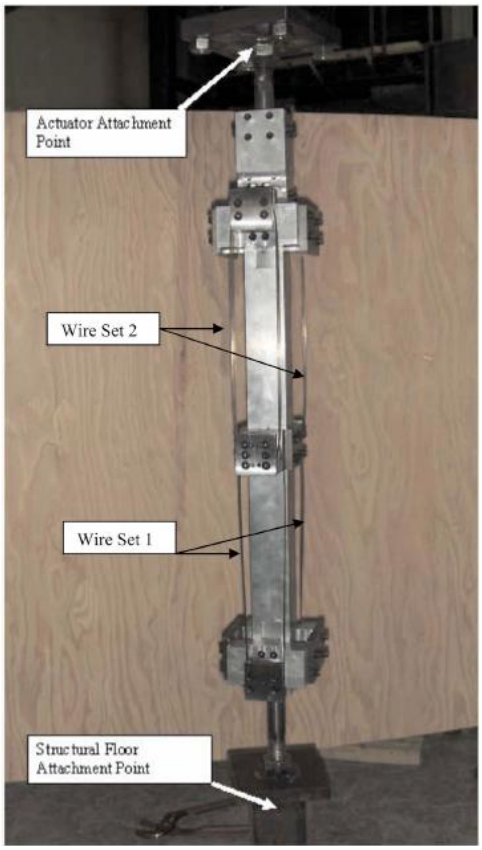

Figure 2-8 SMA response modification device (Van de Lindt and Potts, 2008)

Li *et al.* (2008) designed two types of SMA-based devices where SMA wires are always subjected to elongation and investigated the performance of the devices by performing shake table tests on a five-story steel frame. Zhang and Zhu (2007) investigated an SMA-based device, termed reusable hysteretic damper (RHD). The device comprises two blocks that slide past each other and superelastic NiTi wires attached to the sliding blocks. The hysteretic behavior of the damper can be tuned by adjusting the inclination angle of the wires, the pretension level, and the friction coefficient of the sliding surface. In another study, Zhu and Zhang (2008) studied the

performance of a similar device based on the same concept as the RHD. In this configuration, the energy dissipation capacity of the device was enhanced by adjusting the normal force at contact surface of sliding blocks with applied bolts.

Yang *et al.* (2010) proposed a hybrid device which combines re-centering SMA wires with energy-absorbing steel struts. The device also utilizes two high strength steel tubes to guide the movement of SMA wires and struts. Speicher *et al.* (2009) designed a tension/compression device for seismic retrofit of buildings as shown in Figure 2-9. The device makes use of NiTi helical springs or NiTi Belleville washers in compression. The results of cyclic loading tests suggested that helical springs have good re-centering and damping characteristics while Belleville washers can be used for energy dissipation purposes in an SMA device.

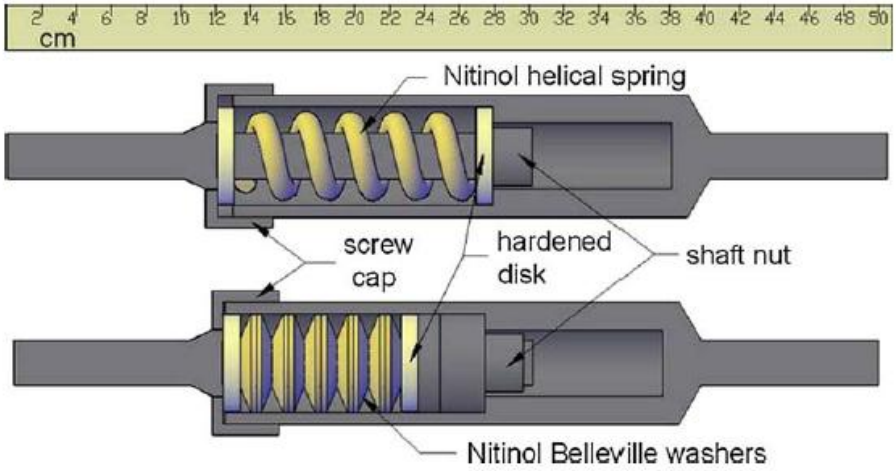

Figure 2-9 SMA tension/compression device (Speicher *et al.*, 2009)

2.4.1.2 SMA bracing systems

Several studies have considered the use of SMAs as diagonal braces in frame structures (Saadat *et al.*, 2001; Han *et al.*, 2003; McCormick *et al.*, 2007a; Lafortune *et al.*, 2007). Some researchers conducted theoretical studies in order to demonstrate the efficacy of SMA-bracing systems. Auricchio *et al.* (2006) investigated the effectiveness of using large diameter NiTi bars as a bracing system for steel structures and compared the SMA braces with buckling-restrained steel braces. The outcome of numerical studies showed that SMA bracing systems can satisfactorily limit the interstory drifts in steel buildings and significantly reduce the residual drifts. Zhu and Zhang (2007b) compared the performance of an SMA braced frame system that employs the reusable hysteretic damper described above and buckling-restrained brace frames. They carried out nonlinear time history analyses of three-story and six-story frame buildings and found that the SMA-braced frame can effectively reduce the story drifts while eliminating the residual drift problem. Torra *et al.* (2007) studied the feasibility of using SMA dampers for seismic protection of light buildings, such as single or double floor family houses. Numerical analyses on a structure with installed diagonal SMA bracing system made of either NiTi or CuAlBe shape memory alloys were performed.

A few researchers carried out experimental tests on building structures with SMA braces. Bartera and Giacchetti (2004) experimentally studied the response of a single story reinforced concrete frame that had been upgraded by different types of bracing systems. They used a high damping rubber pad and an SMA device as supplemental energy dissipation devices in series with steel braces. Free vibration and forced

vibration tests were carried out to evaluate dynamic response of braced frames. Both dissipating bracing systems suppress vibration of the frame by adding a significant amount of damping. Dolce *et al.* (2005b) performed shake table tests on reduced-scale reinforced concrete frames with and without special braces. In particular, they considered energy dissipating steel braces and re-centering SMA braces as passive control braces. They found that both bracing systems can significantly ameliorate the response of the reinforced concrete frames subjected to seismic excitations.

Boroschek *et al.* (2007) explored the use of SMA braces that consist of CuAlBe wires in steel frame buildings. Shake table tests were conducted on a three-story steel frame upgraded with SMA braces and shown in Figure 2-10. The results indicated a substantial reduction in the peak relative displacements and peak accelerations of the frame.

Ozbulut and Roschke (2010) also examined the potential use of SMA as bracing elements in tall structures. They carried out a multiple-objective numerical optimization that simultaneously minimizes displacements and accelerations of the structure in order to optimize SMA bracing elements within the structure. After design of an optimal SMA damping system was complete, full-scale experimental shake table tests were conducted on a large-scale steel frame that was equipped with the optimal SMA devices.

Figure 2-10 A three-story steel frame model with SMA braces (Boroschek *et al.*, 2007)

2.4.1.3 SMA beam-column connectors

There are several studies that investigated the use of SMAs as beam-column connection elements. Ocel *et al.* (2004) experimentally evaluated the performance of partially restrained steel beam-column connections using martensitic SMAs. Four large diameter NiTi bars were used to connect the beam flange to the column flange and serve

as the primary moment transfer mechanism. Two SMA-based full-scale connections were tested under quasi-static and dynamic cyclic loading. The SMA bars were heated above the transformation temperature to initiate shape memory effect after the initial test. It was observed that the SMA connection was able to recover 76% of the beam tip displacement.

Ma *et al.* (2007) studied a self-centering beam-to-column connection using superelastic SMAs. The connection consist of an extended end-plate, long shank SMA bolts, continuity plates, beam-flange ribs and web stiffeners. The steel I-beam and column were connected by the extended end-plate and eight long shank superelastic NiTi bolts. The SMA connection was modeled in the finite element program ANSYS and numerical simulations were performed to predict the behavior of the connection. The connection was found to have good energy dissipating characteristics and ability to recover 94% of its total deformation. Also, no local buckling of the connecting beam, typically observed in traditional connections, occurred during the whole loading history.

Sepulveda *et al.* (2008) performed an experimental investigation on a partially restrained steel beam-column connection using CuAlBe shape memory alloys. A prototype of the connection was cyclically tested at 0.25 Hz and 1 Hz. Stable cycles with equivalent damping ratios up to 5.5% were obtained for the deformation of connection with negligible residual strains at the SMA bars.

Youssef *et al.* (2008) explored the feasibility of using superelastic SMAs as reinforcement in beam-column joints of reinforced concrete structures. They tested two large-scale beam-column joint specimens. One specimen was reinforced with regular

steel rebars, while the other was reinforced with NiTi longitudinal rebars in conjunction with steel rebars. The results demonstrated that SMA-reinforced beam-column joints had lower energy dissipation capacity and lower bond strength to concrete compared to those of steel joints; yet, they recovered most of its post-yield deformation whereas steel joint experienced large residual drifts. This indicates that an SMA joint can remain functional even after a strong earthquake. The same researchers also developed a numerical model that can simulate the behavior of SMA-reinforced concrete beam-column joints in another study (Alam *et al.*, 2008).

DesRoches *et al.* (2010) also studied the seismic performance of steel frames with beam-to-column connections that incorporate SMA bars. They considered a superelastic SMA connection with re-centering capability and a martensitic SMA connection with energy dissipation capacity. Numerical models of both connections were developed in a finite element framework and validated using full-scale experimental test results. Then, the models were implemented to carry out nonlinear time history analyses of three- and nine-story moment-resisting frames. SMA connections were found to be most effective in controlling structural response under high levels of seismic intensity. In a companion paper, the researchers carried out a probabilistic seismic demand analysis to assess statistically the efficacy of utilizing SMA connections in steel moment-resisting frames (Ellingwood *et al.*, 2010).

2.4.1.4 SMA-based isolation devices

Dolce *et al.* (2007b) investigated the performance of an SMA-based isolation device for seismic protection of building structures by performing shake table tests on

reduced-scale reinforced concrete frames. Two types of SMA-based isolation system were considered. One included three steel-PTFE sliding bearings and an SMA device developed in MANSIDE project, while the other combined the first isolation device with a steel hysteretic component. The performances of the SMA-based isolation systems were compared with rubber-based and steel-based isolation devices.

Cardone *et al.* (2006) further studied the behavior of above described SMA-based isolation system by equipping a three-story reinforced concrete structure with an SMA-based isolation system and performing *in situ* release tests. The superstructure was moved to up to 140 mm, corresponding to the maximum displacement produced by a strong earthquake with 0.30g PGA, and suddenly released. The results of the release tests proved the excellent performance of the isolation system. A model of the isolated building was developed and the model parameters were calibrated with the results of the experimental tests. Numerical simulations were conducted using the developed model to investigate the effects of various factors on the seismic performance of SMA-based isolation system.

2.4.2 Applications to Bridges

2.4.2.1 SMA restrainers

Multiple frame bridges subjected to strong earthquakes can experience large relative hinge displacements that lead to unseating of their superstructure. Several researchers proposed using SMAs as unseating prevention devices to overcome some of the limitations of traditional devices such as steel cable restrainers, steel rods, and shock transmission units. Andrawes and DesRoches (2005) evaluated the effectiveness of

SMA restrainers in preventing the unseating of a typical multiple frame reinforced box girder bridge. SMA restrainers, designed as a tension-only device, were represented with the 12.7 mm diameter superelastic NiTi rods. The performance of the SMA restrainers was compared with that of traditional steel cable restrainers. The results of nonlinear dynamic analyses showed that SMA restrainers provides significant reduction in relative hinge openings compared to steel restrainers without increasing the ductility demand on the bridge frames. The effect of ambient temperature on the performance of SMA restrainers was assessed in another study by the same researchers (Andrawes and DesRoches, 2007a). Andrawes and DesRoches (2007b) also carried out a sensitivity study to compare the effectiveness of SMA restrainers with other retrofit devices including steel restrainer cables, metallic dampers, and viscoelastic dampers.

A few experimental studies were conducted to examine the feasibility of SMA restrainers. Johnson *et al.* (2008) performed shake table tests to determine the effects of SMA restrainers on seismic response of multiple-frame concrete bridges and to compare the performance of SMA restrainers to that of steel restrainers. The test specimen which simulates an in-span hinge within a multi-span concrete box girder bridge consists of two concrete blocks supported by elastomeric bearing pads. Padgett *et al.* (2009) studied the efficacy of SMA restrainers by testing a four-span, one-quarter scale, concrete bridge on a shake table. SMA restrainers were composed of bundled superelastic NiTi wires and connected at the deck-abutment interface as shown in Figure 2-11. The results of these experimental studies verified the favorable behavior of SMA restrainers as unseating prevention devices.

Figure 2-11 Experimental test setup and SMA restrainer (Padgett *et al.*, 2009)

Choi *et al.* (2009) suggested the use of SMA bars in bending as seismic restrainers for bridges. They first studied the bending behavior of NiTi bars with a diameter of 25.4 mm by performing single and double bending tests. Then, they carried out dynamic analyses of a three-span simply supported steel bridge with SMA restrainers installed perpendicular to the deck beside expansion bearings. They found that SMA bending bars restrain deformation of the columns and prevent pounding at the abutments.

2.4.2.2 SMA dampers for cable-stayed bridges

Application of shape memory alloys in vibration mitigation of stay cables have been studied by several researchers. Casciati *et al.* (2008) studied the feasibility of an SMA wire-steel cable system that consists of a steel cable with superelastic SMA wire wrapped several times around the cable. In particular, Cu-based pre-stressed SMA wire with a diameter of 1 mm was wrapped once, three times, five times around the cable in different configurations. The results of experimental tests on a scaled model steel cable

showed that SMA wire decreases the amplitude of vibrations and increases the fundamental frequencies and damping coefficient. Also, increasing the number of times the SMA wire wrapped around the cable increased the damping ratio of the system. Faravelli *et al.* (2010) proposed a hybrid control solution which combines wrapped SMA wires and an open-loop control strategy to further improve the response of stay cables when they are subjected to strongly nonlinear vibrations.

Li *et al.* (2004) conducted a theoretical study on the vibration mitigation of a combined cable-SMA damper system. It was found that an SMA damper is capable of simultaneously suppressing the cable vibration dominated by the first few modes, yet it was noted that the performance of the SMA damper considerably depends on various design characteristics of the damper. In another study, Liu *et al.* (2007) carried out experimental investigations on the combined stay cable model-SMA damper system to verify the numerical analysis.

Zuo and Li (2009) developed an SMA damper using superelastic SMA wires and numerically and experimentally investigated the effectiveness of the damper on the vibration mitigation of a cable subjected to free and forced vibrations. A scaled model cable-stayed bridge was considered as experimental test platform. The results showed that SMA dampers can both reduce the vibration decay time and decrease the in-plane acceleration response.

Sharabash and Andrawes (2009) explored the performance of superelastic SMA dampers for the seismic control of cable-stayed bridges. They developed a 3-D finite element model of a bridge including effects of soil-structure interaction. SMA dampers

were assumed to be in the form of cables consisting of bundled SMA wires and implemented at the deck-pier and deck-tower connections. They conducted a sensitivity analysis to evaluate the effect of variations of SMA damper characteristics on the bridge response and to determine the optimum distribution of SMA dampers between pier and tower connections. The results revealed that SMA dampers are able to significantly decrease maximum bridge displacement, the tower's base shear and the tower's base moment.

2.4.2.3 SMA reinforcement

One of the reasons for bridge failures occurred during past earthquakes is large lateral displacements of reinforced concrete (RC) bridge columns imposed by strong ground motion. This leads to permanent deformations and severe damage in the structure. Shape memory alloys have been considered as an alternative to traditional steel reinforcement in bridge columns in order to reduce permanent displacements and damage in concrete bridge columns. Saiidi and Wang (2006) tested concrete column specimens with SMA longitudinal reinforcement in the plastic hinge zone on a shake table to determine the effectiveness of SMA bars. They also evaluated the performance of an SMA-reinforced column that was repaired using engineering cementitious composites (ECC). The test results showed that SMA-reinforced columns were capable of recovering nearly all of the post-yield deformations and that the use of ECC reduced the concrete damage substantially. Saiidi *et al.* (2009) also studied the cyclic response of concrete bridge columns using SMA bars and ECC. For comparison purposes, they

tested a column specimen with conventional concrete and steel reinforcement and a column specimen with conventional concrete and SMA bars.

Andrawes *et al.* (2010) investigated the feasibility of using spirals made of SMAs for seismic retrofitting of RC bridge columns. They conducted uniaxial compression tests on concrete cylinders confined with 12-loop NiTi martensitic wires with a diameter of 3mm as shown in Figure 2-12. Using the experimental results, they developed an analytical model to represent the behavior of RC columns retrofitted with SMA spirals. The performance of the SMA retrofitted column was compared with that of carbon fiber-reinforced polymer (CFPR) retrofitted column. The analytical results showed that RC columns retrofitted with SMA spirals outperformed CFPR retrofitted columns in terms of enhancing the strength and effective stiffness and reducing the residual deformations.

Figure 2-12 Concrete specimen with SMA spirals (Andrawes *et al.*, 2010)

2.4.2.4 SMA-based isolation devices

The development of new base isolation systems based on superelastic behavior of SMAs has recently attracted interest of several researchers. Wilde *et al.* (2000) proposed a base isolation system that is composed of a laminated rubber bearing and an SMA device for protecting elevated highway bridges from the hazard of earthquakes. They compared the performance of the proposed isolation system with a laminated rubber bearing that has a lead core. Choi *et al.* (2006) developed a new isolation system for seismic protection of bridges using elastomeric bearings and SMA wires. Analytical studies on a multi-span steel bridge illustrated that the combination of an SMA-rubber bearing effectively decreases relative displacement between deck and pier when compared with a conventional lead-rubber bearing. Dolce *et al.* (2007a) studied the performance of three different sliding-type isolation systems that employ rubber, steel or shape memory alloys as auxiliary device. They proposed two design procedures, the displacement and force approach, to design isolation systems.

Casciati and Faravelli (2009) introduced an innovative isolation device in which a sliding system is coupled with inclined CuAlBe shape memory alloy bars that function for energy dissipating and re-centering purposes. In another study, Casciati *et al.* (2009) investigated the performance of the developed SMA isolation device for a seismically-excited highway bridge benchmark problem. It was found that the SMA isolation device can largely reduce peak displacement response while increasing peak base shear and overturning moment.

3. EXPERIMENTAL TESTS ON SUPERELASTIC SMAs

3.1 Introduction

As discussed in Section 2, the mechanical response of SMAs is highly dependent on temperature and loading-rate. When SMAs are used as an isolation system component for seismic protection of bridges, they will experience both temperature changes and dynamic loads. Therefore, it is essential to consider the degree to which behavior of SMAs is affected by variations of loading rate and temperature.

In this study, a neuro-fuzzy model, described thoroughly in the next section, is employed to capture the superelastic behavior of NiTi shape memory alloys (Ozbulut and Hurlebaus, 2010a). In order to develop a fuzzy model of superelastic SMAs, experimental data are needed. In this section, first, uniaxial tensile tests that are performed on NiTi superelastic wires at various loading rates and ambient temperature are presented. Then, the effects of temperature, strain rate, and strain amplitude on mechanical behavior of superelastic NiTi wires are evaluated.

3.2 Experimental Procedure

3.2.1 Material and Specimen

The material used in this research is NiTi wires with a diameter of 1.5 mm obtained from SAES Smart Materials. The alloy chemical composition has 55.8% nickel by weight and the balance titanium. The austenite start and finish temperatures are specified by manufacturer as A_s = -10ºC and A_f = 5°C, respectively. The test samples are obtained by cutting the wire into pieces with a length of 305 mm.

3.2.2 Experimental Apparatus

An MTS (Material Testing System) servo-hydraulic load frame as shown in Figure 3-1 is used to conduct tests at various frequencies and temperatures. The MTS load frame is equipped with a heating/cooling chamber to create desired environmental temperatures. An insulated thermocouple is placed inside the chamber to monitor the temperature. For experiments below room temperature, cooling is provided by liquid nitrogen. A temperature controller that operates a cryogenic grade, on/off solenoid valve is used to alter the flow of nitrogen gas into the environmental chamber enclosing the sample.

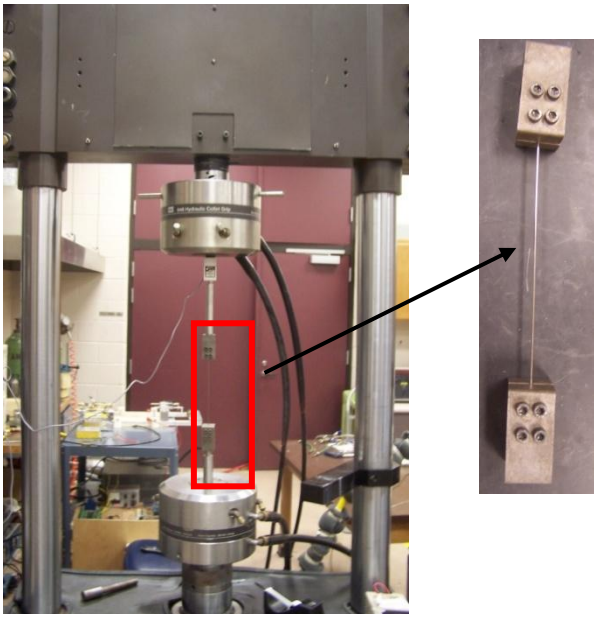

Figure 3-1 MTS loading frame and test specimen

3.2.3 Testing Procedure

In order to collect data for modeling superelastic behavior of SMA, a thorough experimental testing program is followed. Specifically, a large number of sinusoidal tensile tests are performed under displacement control with a constant frequency. The wires are tested at five strain amplitudes. The frequency of loading ranges from 0.05 Hz to 2 Hz that is the frequency range of most of the seismic events. These strain amplitudes and loading frequencies yield a strain-rate ranging from 0.0004 s^{-1} to 0.24 s^{-1}. The amplitude and frequency of sinusoidal deformations on the specimen are set for each test by using computer software that controls the MTS frame. The tests are performed at various temperatures. Since the material loses completely its superelastic behavior under A_s temperature of the material that is -10ºC, the temperature range for the tests is selected to be 0-40ºC. Table 3-1 summarizes the levels of three independent variables that are temperature, strain amplitude and loading frequency. The tests are conducted for each combination of these variable levels. Before formal tests, in order to stabilize hysteretic loops (Dolce and Cardone, 2001), a training test procedure that consists of 10 load cycles with strain amplitude of 6% at 0.04 Hz and at room temperature is applied to all samples. The tensile tests are conducted for 3 cycles in each case; however, as shown from Figure 3-2 which illustrates two test results at different conditions, since the obtained hysteresis loops are stable, only the last cycle is plotted in the figures for the purpose of clarity in the next sections.

Table 3-1 Experimental conditions

Variables						
Temperature	0 ºC	10 ºC	23 ºC	30 ºC	40 ºC	
Strain amplitude	2%	3%	4%	5%	6%	
Frequency	0.05 Hz	0.1 Hz	0.5 Hz	1 Hz	1.5 Hz	2 Hz

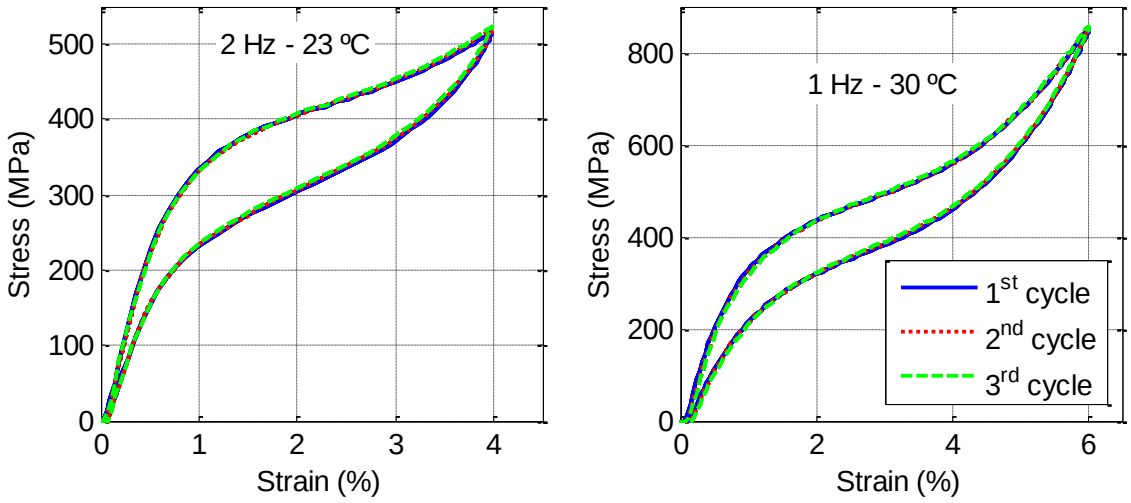

Figure 3-2 Hysteresis loops of superelastic SMA wires for 1st, 2nd, and 3rd loading cycles

3.3 Experimental Results

3.3.1 Temperature Effects

In this section, the temperature dependence of superelastic behavior of NiTi wires is investigated by comparing the experimental tests conducted at different temperatures. Figure 3-3 shows strain-stress curves of NiTi wires at a particular loading frequency at different temperatures. They are plotted for a maximum strain of 5% since

SMA wires significantly lose their superelastic behavior at 6% strain at 0 ºC. It can be observed that at each loading rate, hysteresis loops of SMA shifts upward as temperature increases. Also, it is seen that at 0ºC, SMA wires show completely superelastic behavior at high loading rates (i.e. over 0.5 Hz), whereas there is about 1% residual strain at slower frequencies.

Energy dissipated per cycle, equivalent viscous damping and secant stiffness for each experiment are computed in order to evaluate the test results in a quantitative way. Equivalent viscous damping is computed as dissipated energy per cycle (the area inside the hysteresis loop) divided by the product of 4π and maximum strain energy (the area under a complete cycle). The secant stiffness is calculated as the ratio of the difference between maximum and minimum force on the wire and the difference between maximum and minimum deformation of the wire.

Figure 3-4 illustrates the variation of energy dissipation with temperature at different loading rates. It can be observed that the energy dissipation decreases as temperature increases, especially at high loading rates (over 0.5 Hz). The maximum decrease is observed to be about 30% for a frequency of 2 Hz. Nevertheless, there is no significant change in dissipated energy with test temperature especially at low frequencies. The dissipated energy only decreases 5% when temperature increases from 0 ºC to 40 ºC for loading frequencies of 0.05 Hz and 0.1 Hz.

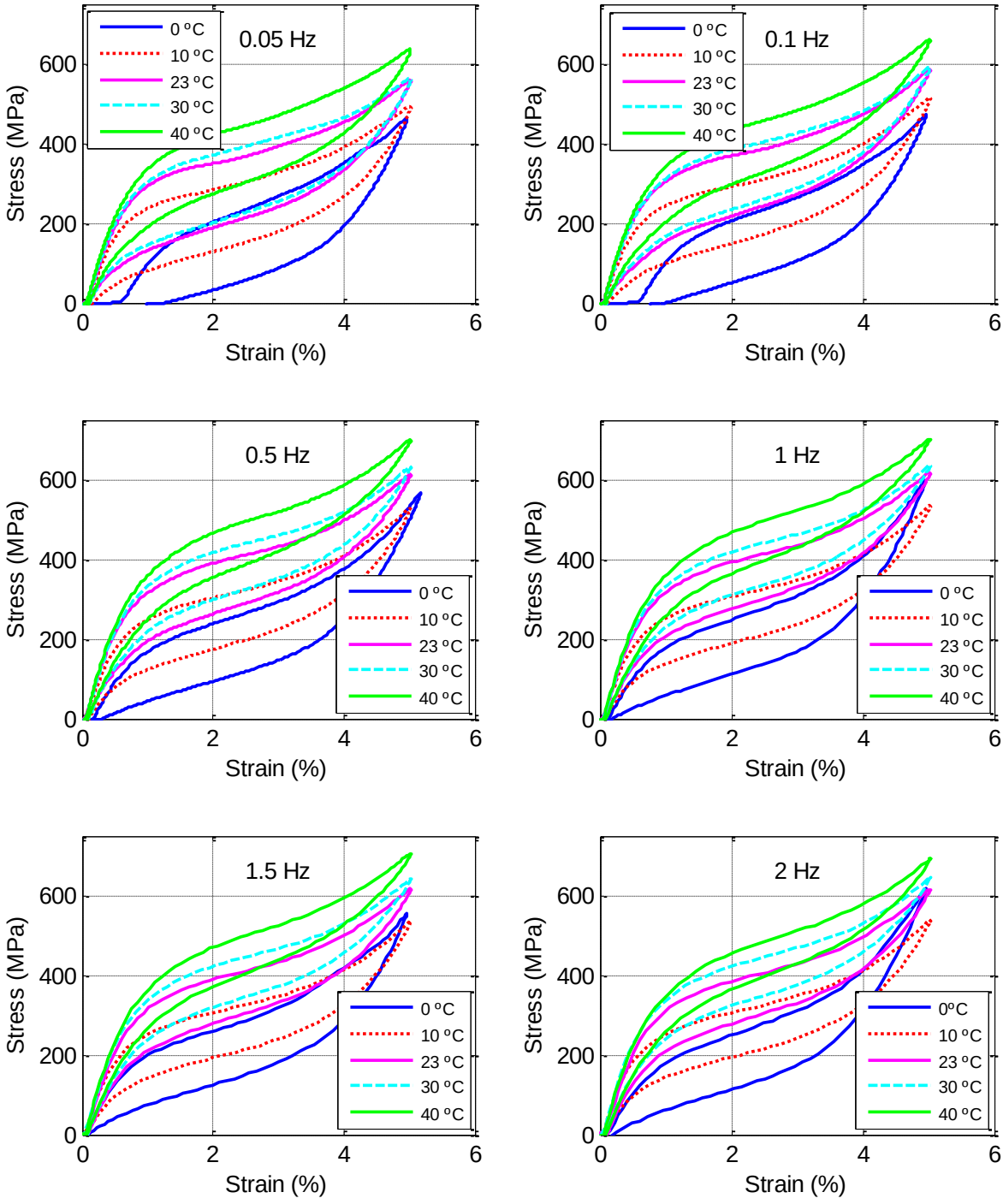

Figure 3-3 Experimental strain-stress curves of NiTi wires at various temperatures and loading frequencies

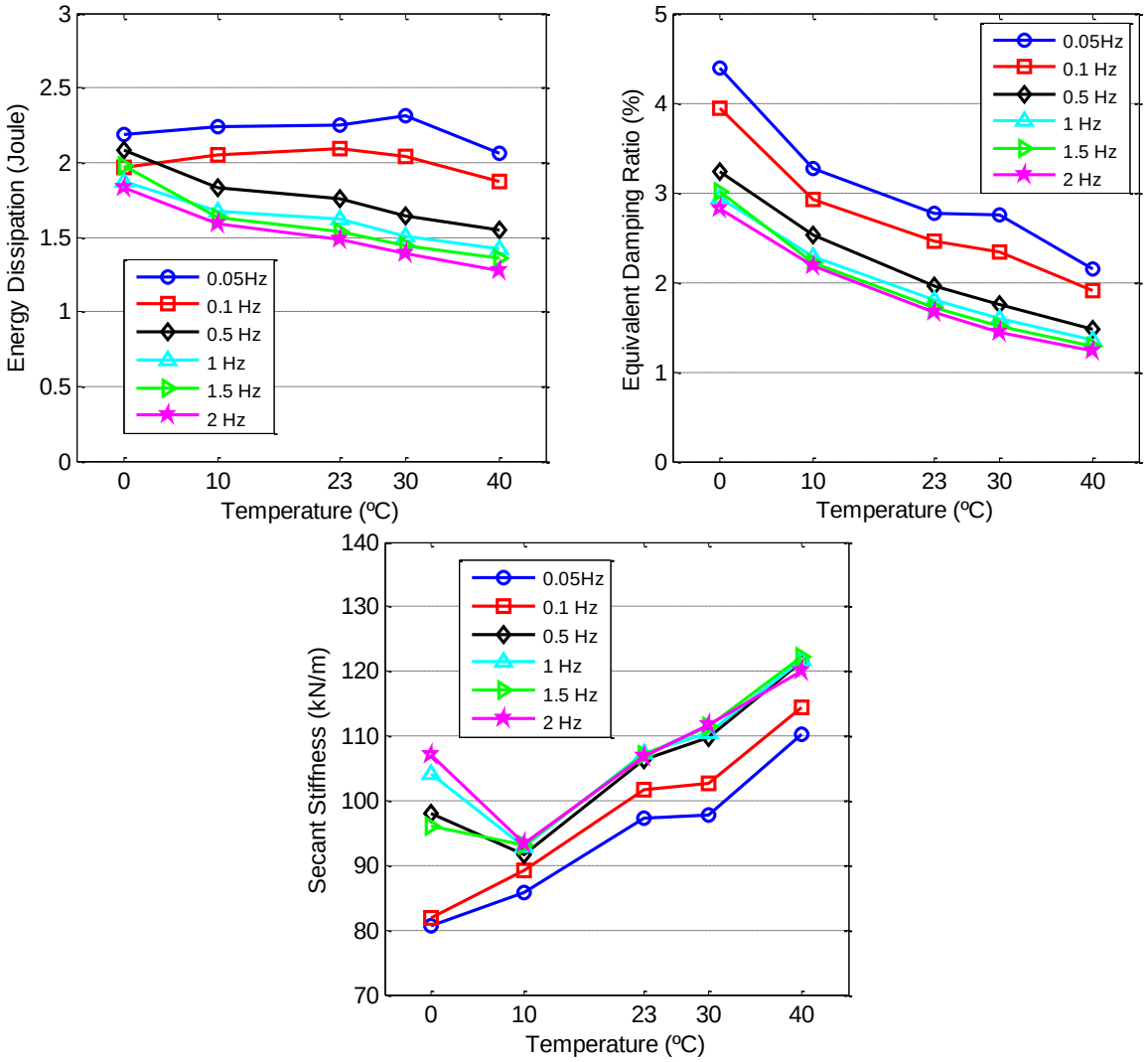

Figure 3-4 Energy dissipation, equivalent viscous damping and secant stiffness of NiTi wires as a function of temperature at different loading frequencies

The change of equivalent viscous damping and secant stiffness of SMA wires with temperature are given also in Figure 3-4. As shown in the figure, equivalent viscous damping decreases with increasing temperature. Despite the slight decrease in dissipated energy with temperature, the increase in secant stiffness at higher temperatures, results in higher strain energy per cycle and decreases the equivalent

viscous damping. As temperature increases from 0 ºC to 40 ºC, the equivalent viscous damping reduces 44% and 43% for slowest (0.05 Hz) and highest (2 Hz) loading rates, respectively. It can be seen that the secant stiffness increases by about 30% with the increasing temperature at each loading frequency. Furthermore, it is observed that the secant stiffness increases considerably at 0 ºC at high loading rates due to significant strain hardening which is a result of the complete transformation to the martensite phase and the further elastic deformation in this phase.

3.3.2 Strain Rate Effects

Figure 3-5 shows the stress-strain curves for superelastic NiTi wires at room temperature and at the other test temperatures for various loading frequencies. The results for 0ºC is plotted for maximum strain of 5% while for all the other test temperatures, stress-strain curves are given for 6% strain.

As can be seen from the figure, loading frequency considerably influences the stress-strain relation of NiTi wires. Especially, there is a noticeable difference between measured loops at low frequencies (0.05-0.1 Hz) and those at higher frequencies (0.5 Hz- 2 Hz). In general, the initial elastic stiffness is almost the same at each loading rate, but the upper plateau and lower plateau stress levels during phase transformations increase as the frequency is increased. Since the lower plateau stress level increases more, the hysteresis loop narrows and, as a result, energy dissipation reduces.

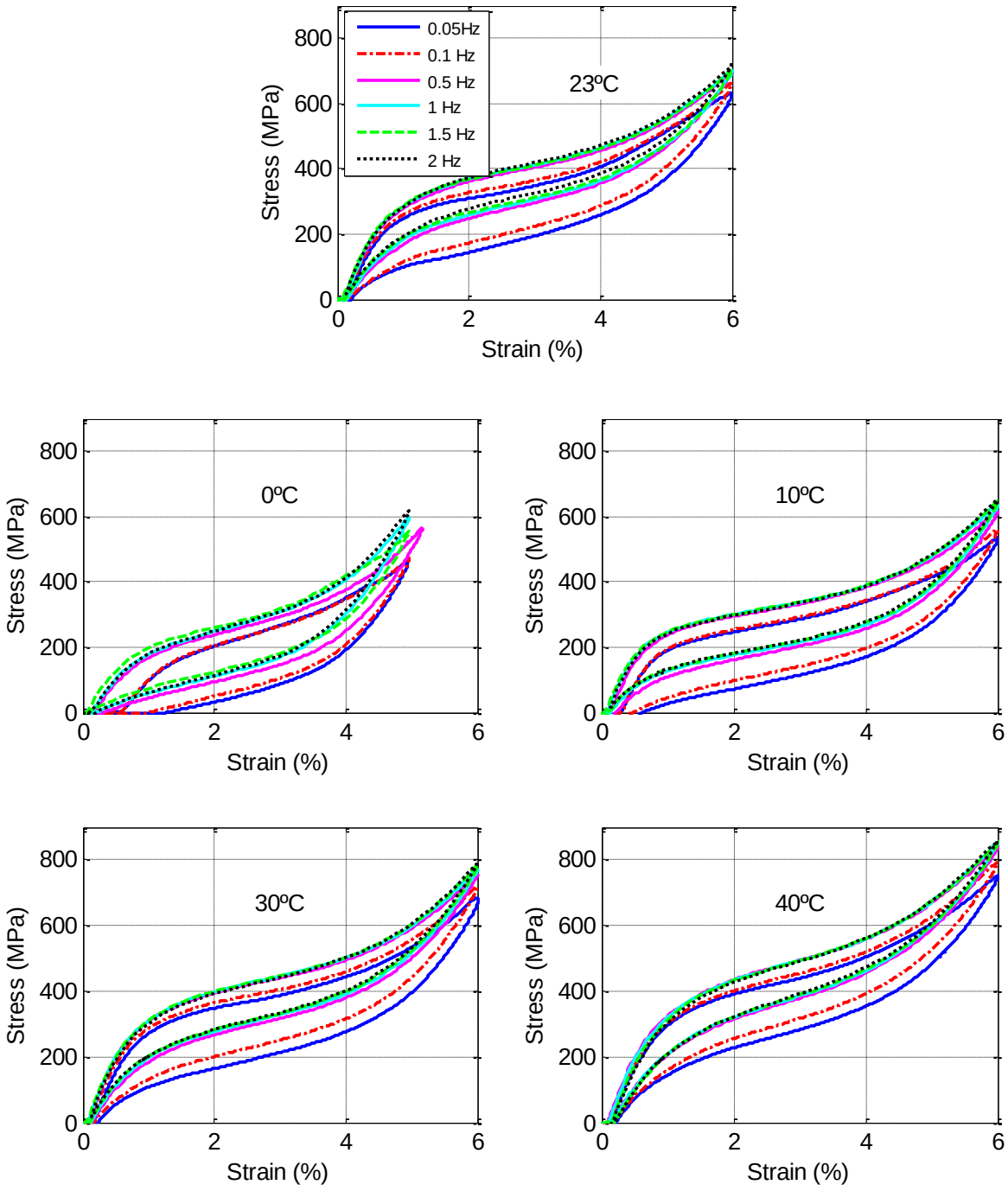

Figure 3-5 Experimental strain-stress curves of NiTi wires at various temperatures and loading frequencies

When SMAs are used for seismic applications, it is important to evaluate the effects of dynamic loading on damping properties of the material. Figure 3-6 shows the variation of energy dissipated per cycle, equivalent viscous damping, and secant stiffness with loading frequency at various temperatures using a semi-log axis for frequency. It is observed that dissipated energy decreases between a minimum of 28% for the test temperature of 10ºC and a maximum of 40% for the test temperature of 30ºC when the loading frequency increases from 0.05 Hz to 2 Hz. Similarly, as the frequency increases from 0.05 Hz to 2 Hz, the equivalent viscous damping decreases between 35% and 47% for different test temperatures. This shows higher loading rates markedly affect the material response and its damping capability.

However, the dissipated energy decreases only between 12% and 17%, and the equivalent viscous damping decreases between 13% and 17% for different test temperatures, when frequency is increased from 0.5 Hz to 2 Hz. This indicates that the effect of loading rate on the behavior of NiTi wires is particilarly significant over the range of smaller frequencies. Also, the secant stiffness increases almost linearly by about 9% with increasing loading frequency at each test temperature.

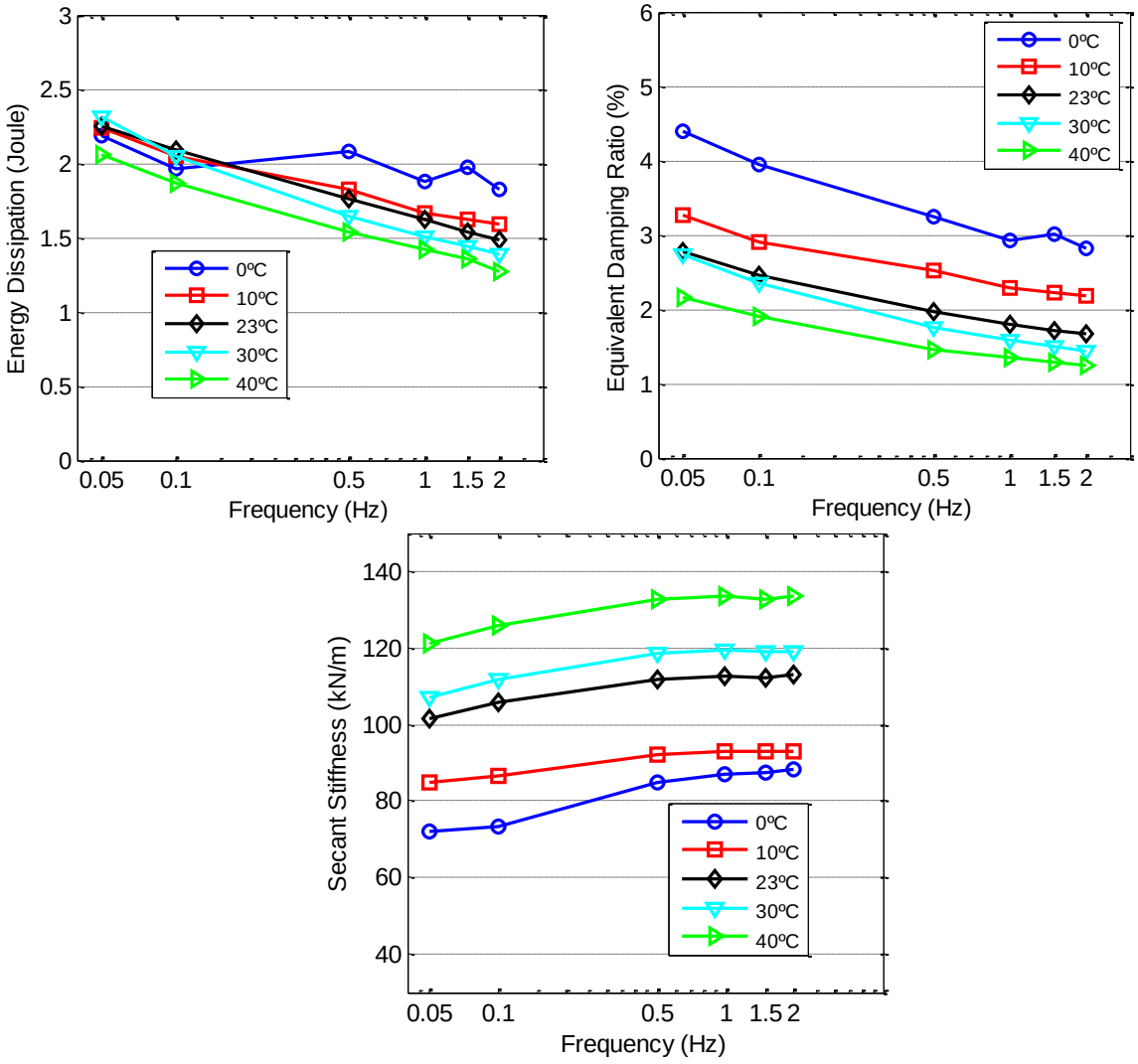

Figure 3-6 Energy dissipation, equivalent viscous damping and secant stiffness of NiTi wires as a function of loading frequency at different temperatures

3.3.3 Strain Amplitude Effects

Figure 3-7 shows the stress-strain curves of NiTi wires for increasing strain amplitudes at 0.1 Hz, and the variation of equivalent viscous damping with strain amplitude. The test results at room temperature are presented in the figure. It is clear

that energy dissipation per cycle increases for higher strain amplitudes. However, equivalent viscous damping is usually highest at about 3-4% strain amplitude, and decreases to some extent for larger strain amplitudes. That is due to strain hardening effects at higher level of strains as observed in previous studies (Dolce and Cardone, 2001; DesRoches *et al.*, 2004).

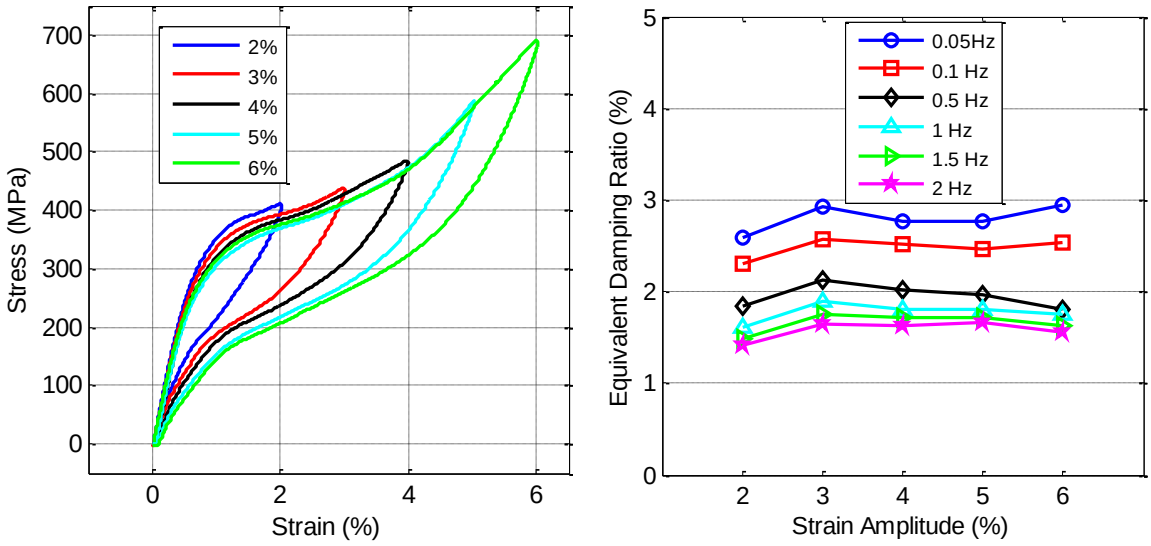

Figure 3-7 Experimental strain-stress curves of NiTi wires at various strain amplitudes, and equivalent viscous damping as a function of strain amplitude

3.4 Closure

In order to create a fuzzy model of SMA wires that is capable of simulating hysteretic behavior of SMAs at different conditions, a set of experimental data that is representative of SMA behavior at these conditions is needed. Therefore, uniaxial tensile tests are performed on NiTi shape memory alloy wires using an MTS servo-

hydraulic load frame. Also, the effects of temperature, strain rate and strain amplitude on the mechanical response of superelastic SMAs were evaluated.

The results show that the loading frequency and temperature considerably affect the behavior of superelastic SMAs. In particular, an increase in either temperature or loading frequency shifts the hysteresis loop upward. It is noted that the effect of the temperature is more pronounced than the influence of loading frequency.

The area of the hysteresis loop, which represents the energy dissipation of superelastic SMAs, narrows with increasing temperature or loading frequency. As a consequence, as the temperature increases from 0 ºC to 40 ºC, there is a decrease of 44% and 43% in the equivalent viscous damping for slowest (0.05 Hz) and highest (2 Hz) loading rates, respectively. Similarly, the equivalent viscous damping decreases between 35% and 47% for different test temperatures as the frequency increases from 0.05 Hz to 2 Hz.

The results indicate that the effects of temperature and strain rate on the superelastic behavior of NiTi wires are significant. Therefore, an analytical model that is used to represent behavior of SMAs should consider these effects. In the next section, a temperature- and rate-dependent neuro-fuzzy model is developed in order to capture the response of superelastic SMAs in numerical simulations that are performed to investigate potential use of SMAs as an isolation system component.

4. NEURO-FUZZY MODELING OF TEMPERATURE- AND STRAIN-RATE-DEPENDENT BEHAVIOR OF SMAs

4.1 Introduction

Although there are a significant number of models that employ different theories and principles to capture the behavior of SMAs, only a few of them are suitable and practical for seismic applications. That is because some of the SMA constitutive models are too complicated and numerically expensive to implement into simulations, whereas simplified models do not include loading rate and/or temperature effects that influence considerably the behavior of SMAs (Motahari and Ghassemieh, 2007).

In this section, a neuro-fuzzy model is developed to simulate the superelastic behavior of NiTi shape memory alloys. This model is capable of capturing rate- and temperature-dependent material response while it remains simple enough to carry out numerical simulations. First, a background information on neuro-fuzzy modeling is provided. Then, three major steps in developing a fuzzy model, namely, data selection, ANFIS training and model validation are clearly explained for a fuzzy model of superelastic NiTi wires.

4.2 Neuro-Fuzzy Modeling

Neural networks and fuzzy systems are among the soft computing methodologies that can be used to handle complex nonlinear systems. Hybrid combinations of these two methods can lead to better technologies that take advantage of the strengths of each methodology. Specifically, fuzzy models can represent nonlinear systems by encoding

expert knowledge directly using rules with linguistic labels, rather than complex differential equations describing the behavior of the systems; while neural networks can be used to tune the membership functions that quantitatively represent linguistic labels in a fuzzy system (Nguyen *et al.*, 2003).

Among various types of fuzzy inference sytems, the Sugeno (or Takagi-Sugeno-Kang) method of fuzzy inference is more suitable for modeling. The Sugeno-type FIS (Takagi and Sugeno, 1983) can map a set of input variables to a single output. Figure 4-1 illustrates the flowchart of a fuzzy inference system. The first step of a fuzzy inference process is to fuzzify the inputs by defining membership functions to each input variable. The decision for the number and type of member functions is also made in this step. Then, a fuzzy rule base is used to relate the inputs and output. A typical rule in a Sugeno fuzzy model has the form:

Rule i: *IF* x_1 *is* A_{i1} *and* x_2 *is* A_{i2} *…and* x_n *is* A_{in}

THEN $y_i = c_{i0} + c_{i1} x_1 + c_{i2} x_2 + \ldots + c_{in} x_n$

where x_1, x_2, …, x_n are antecedent variables (inputs); y is the consequent variable (output) of rule i; A_{i1}, A_{i2}, …, and A_{in} are membership functions defined over the domains of the respective antecedents; and c_{i0}, c_{i1}, …, c_{in} are constant coefficients that characterize the linear relationship of the i^{th} rule in the rule set, (i = 1, 2, … , r). The final output of a Sugeno model is the weighted average of all rule outputs, computed as:

$$y = \frac{\sum_{i=1}^{r} w_i y_i}{\sum_{i=1}^{r} w_i} \qquad (4\text{-}1)$$

where w_i is the matching degree of the i^{th} rule. Upon defining fuzzy rules, a fuzzy inference engine is employed to evaluate the rules using a fuzzy inference mechanism in order to decide on the output for a given input set. Finally, a defuzzification method is used to obtain a non-fuzzy discrete value.

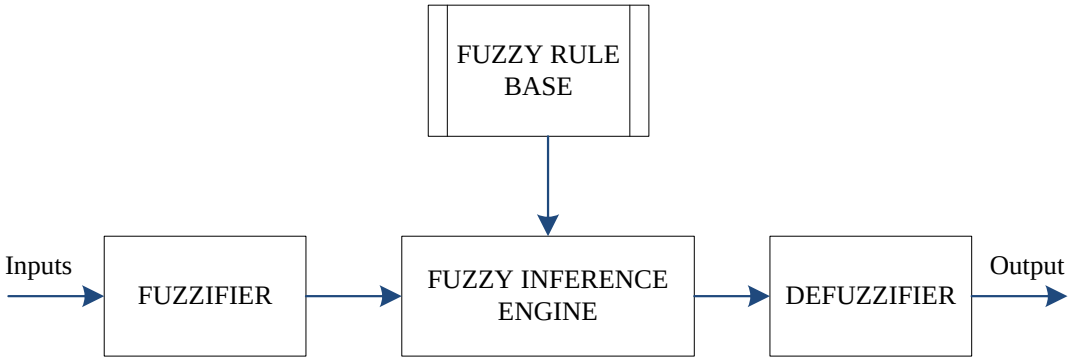

Figure 4-1 Flowchart of a fuzzy inference system

The adaptive neuro-fuzzy inference system (ANFIS) is a soft computing approach that combines fuzzy theory and neural networks (Jang *et al.*, 1997). Specifically, ANFIS employs neural network strategies to develop a Sugeno-type FIS whose parameters (membership functions and rules) cannot be predetermined by user's knowledge. Using a set of input-output data pairs, ANFIS can learn information about the data set and build a model that approximates the real data.

To present the ANFIS architecture, suppose a Sugeno-type fuzzy inference system with two inputs, x_1 and x_2, and one output, y and a rule base which contains two fuzzy rules as follows:

Rule 1: $IF\ x_1\ is\ A_{11}\ and\ x_2\ is\ A_{12}\ ,\ THEN\ y_1 = c_{10} + c_{11}\,x_1 + c_{12}\,x_2$

Rule 2: *IF* x_1 *is* A_{21} *and* x_2 *is* A_{22} *, THEN* $y_2 = c_{20} + c_{21} x_1 + c_{22} x_2$

ANFIS architecture to implement these two rules is shown in Figure 4-2. In the figure, a circle indicates a fixed node, while a square represents an adaptive node. There are five layers in an ANFIS architecture. Each node in *Layer 1* specifies appropriate fuzzy sets to each antecedent parameter using membership functions. The output of each node in this layer is given by:

$$\begin{aligned} O^1_i &= A_{i1}(x_1) \qquad \text{for } i = 1, 2 \\ O^1_i &= A_{(i-2)2}(x_2) \qquad \text{for } i = 3, 4 \end{aligned} \tag{4-2}$$

where A_{1i} and A_{2i} are membership functions for fuzzy sets x_1 and x_2, respectively. Membership functions such as Gaussian, triangular, trapezoidal, etc. can be used to define fuzzy sets.

$$O^2_i = w_i = A_{i1}(x_1) \times A_{i2}(x_2) \qquad i = 1, 2 \tag{4-3}$$

Layer 2 consists of fuzzy neurons with an aggregation operator such as AND/OR to obtain firing strengths, which represent the degree to which the antecedent part of a fuzzy rule is satisfied. Hence, the outputs of the second layer, O^2_i, are the products of the corresponding degrees obtained from Layer 1:

Layer 3 is a normalizer. It contains fixed nodes which compute the ratio of the firing strengths of the each rule to the sum of the firing strengths of all rules as:

$$O^3_i = \overline{w_i} = \frac{w_i}{\sum_i w_i} \qquad i = 1, 2 \tag{4-4}$$

Layer 4 computes the contribution of i^{th} rule towards the final output. Thus, the output of this layer is given by:

$$O^4{}_i = \overline{w_i} y_i = \overline{w_i}(c_{i0} + c_{i1}x_1 + c_{i2}x_2) \qquad i = 1, 2 \tag{4-5}$$

Layer 5 consists of a single node which computes the overall output by summing all incoming signals. The output of the model is given by:

$$O^5{}_i = y = \sum_{i=1}^{2} \overline{w_i} y_i = \overline{w_1} y_1 + \overline{w_2} y_2 = \frac{\sum_{i=1}^{2} w_i y_i}{\sum_{i=1}^{2} w_i} \tag{4-6}$$

ANFIS utilizes a hybrid learning technique to adjust the parameters of an initial FIS. In particular, the gradient descent method is used to determine antecedent parameters (the parameters associated with input membership functions A_{in}), and the least square estimation is used to tune consequent parameters (the parameters of the output, i.e., c_{i0}, c_{i1}, c_{i2}). The detailed information on hybrid learning algorithm is available in Jang (1993).

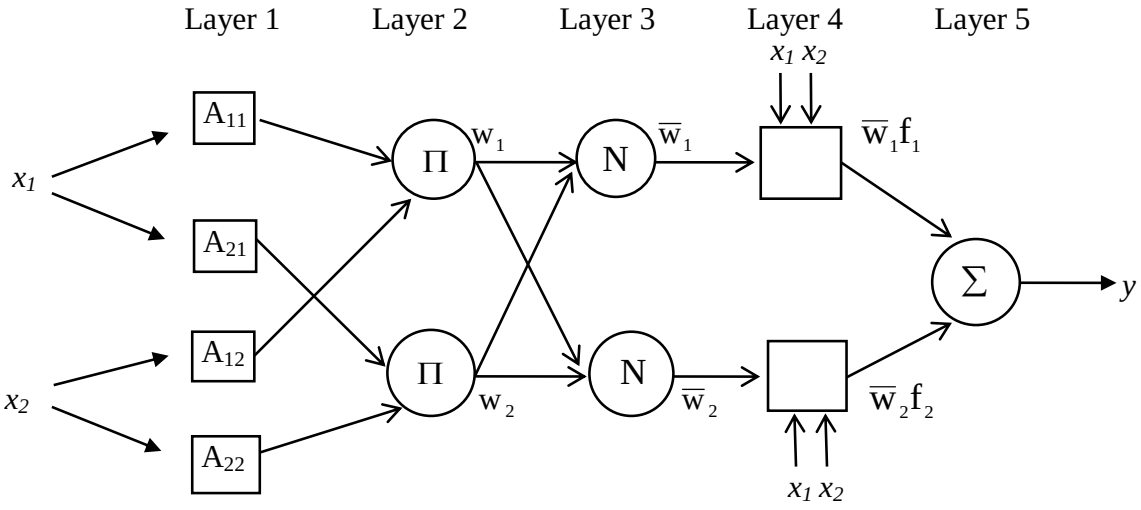

Figure 4-2 ANFIS scheme for two-input Sugeno-type fuzzy model

In this study, ANFIS is used to develop a fuzzy model of NiTi wires that considers loading rate and temperature effects. The following sections explain each step in developing the fuzzy model of superelastic SMAs.

4.3 Initial FIS and Data Selection

For modeling the complex nonlinear behavior of superelastic SMAs considering temperature and rate effects, it is possible to select various inputs to the model under construction. However, using a large number of inputs both impair the transparency of the model and increase the complexity of computation necessary for building the model (Jang, 1996). Here, strain and strain rate on the wire and temperature are selected as input variables. Then, a Sugeno-type FIS that has three antecedent (input) variables and one output is created as shown in Figure 4-3. This initial FIS has random parameters and has no knowledge about the behavior of superelastic SMAs.

Data obtained from experimental tensile tests is concatenated to form training, checking and validation data sets for ANFIS simulations. Training and checking data sets are employed in order to tune parameters of initial FIS, and validation data are used to validate the final FIS. Also, employing checking data avoids overfitting of model during training. Since the goal is to obtain a model that captures dynamic behavior of NiTi shape memory alloy wires at different temperatures, the test results at loading frequencies ranging from 0.5 Hz to 2 Hz and at temperatures ranging from 0ºC to 40 ºC are used. Upon concatenation of these data sets, every third data point is used for training, and the rest similarly is saved as checking and validation data sets. A fourth-

order central difference method is used to calculate strain rate data from measured strain data. Each of training, checking and validation data sets are composed of 17,090 data points. Note that the selected data points should sufficiently cover the universe of discourse of each input variable yet, excessive number of data points should be avoided in order to reduce the time for model construction. More information on setting input/output data sets can be found in Jang (1996) and Buragohain and Mahanta (2008).

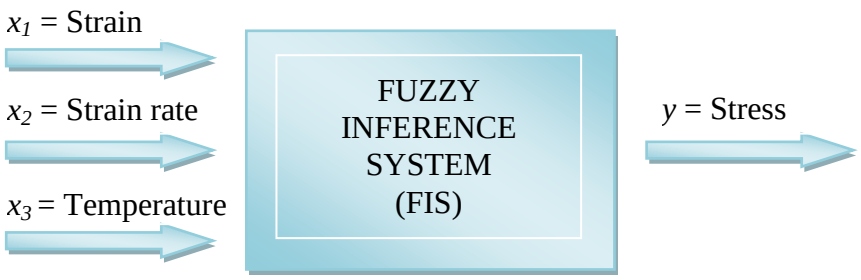

Figure 4-3 Fuzzy inference system with its inputs and output

4.4 ANFIS Training

ANFIS modifies the membership functions and rules of the generic FIS during a procedure called training in order to predict correct stress level for given inputs. Here, different types and numbers of membership functions are used to define each input variable of the initial FIS. Then, these parameters are tuned by ANFIS during training to achieve best results. After several trials, three Gaussian membership functions are assigned to strain (A_{11} (x_1), A_{21} (x_1), and A_{31}(x_1)) and two Gaussian membership functions are chosen for both strain rate (A_{12} (x_2) and A_{22} (x_2)) and temperature (A_{13} (x_3) and A_{23} (x_3)). The Gaussian membership function is defined as:

$$A(x_i) = \exp\left(\frac{-(x-c)^2}{2\sigma^2}\right) \tag{4-7}$$

where c and σ are the parameters that control the shape of the membership function, and x is the antecedent parameter. For the chosen number of membership functions, a total of twelve if-then rules are employed to map input characteristics to a single-valued output. A total of 200 epochs are used to adjust parameters of the membership functions in ANFIS.

Figure 4-4 shows the membership functions of FIS before and after training with ANFIS. As seen in the figure, initial membership functions for strain and strain rate are considerably adjusted by ANFIS. The plots in Figure 4-5 show the inputs of the developed FIS together with the experimental and predicted stress. Note that just a part of stress data is shown in order to better evaluate the performance of the fuzzy model. It can be seen that ANFIS prediction of stress closely follows the experimental training data.

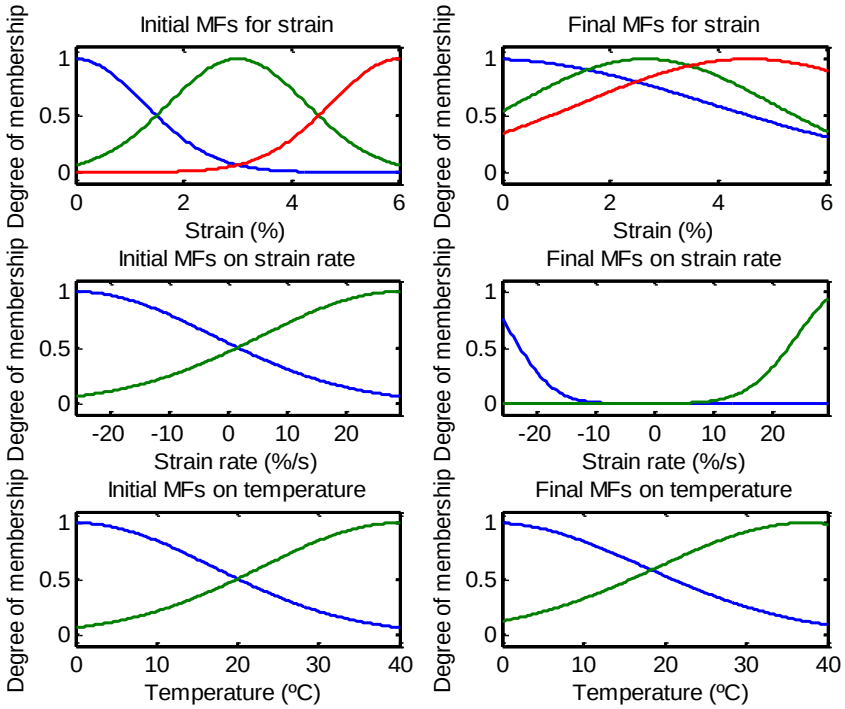

Figure 4-4 Initial and final membership function of FIS

Figure 4-6 shows the variation of stress in NiTi wires versus two input variables of the fuzzy model. The first plot illustrates the surface of predicted stress versus strain and strain rate, while the second stress surface is plotted versus strain and temperature. It is clear that stress changes nonlinearly with a variation in any of three input variables. Also, excessive strain hardening at 0 ºC for high strain amplitudes, which is discussed earlier, can be easily observed in the second plot.

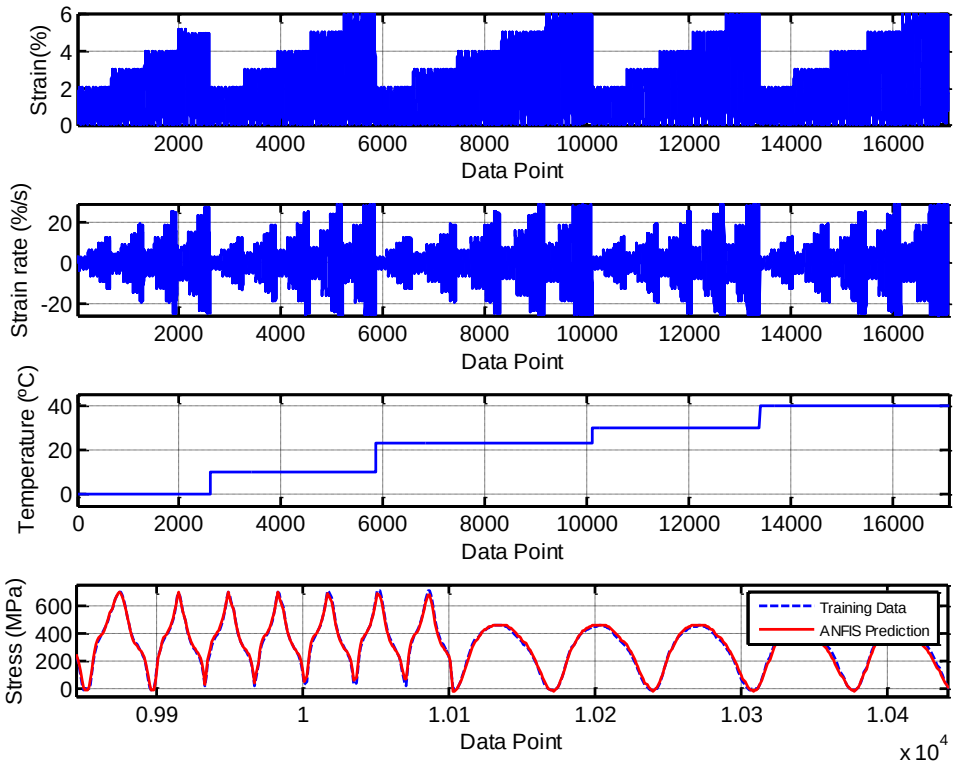

Figure 4-5 Experimental input data and, measured and predicted stress

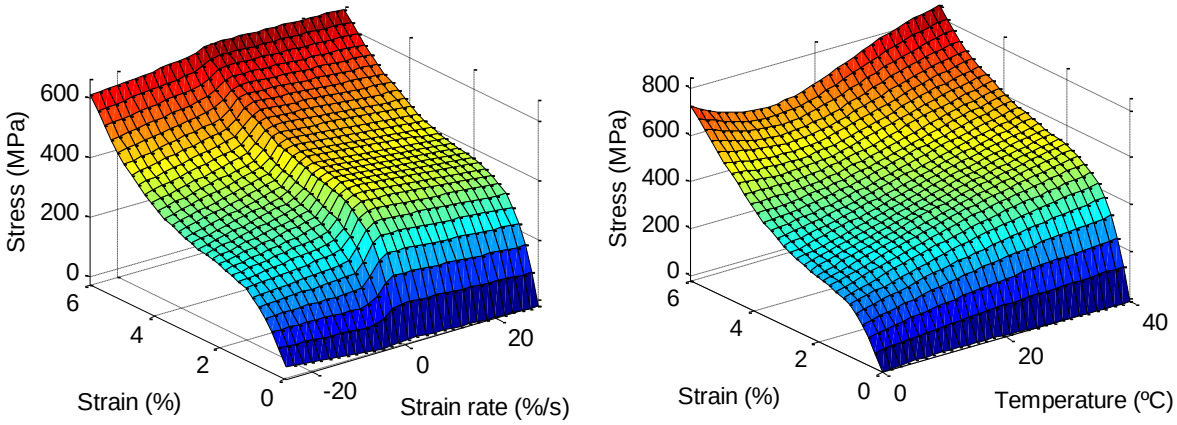

Figure 4-6 Surfaces of stress of the fuzzy model

4.5 Model Validation

Model validation is the process of presenting a data set that is not used during training to the developed FIS to see how well the trained FIS is reproducing the experimental data. Here, the developed FIS is validated using the validation data set described above. Figure 4-7 illustrates several strain-stress curves of NiTi wires for both experimental tests and fuzzy model at different temperatures, loading rates and strain amplitudes. In particular, experimental test results obtained for (i) a loading frequency of 1 Hz at 0 ºC and 4% maximum strain, (ii) a loading frequency of 1.5 Hz at 10 ºC and 5% maximum strain, (iii) a loading frequency of 2 Hz at 30 ºC and 6% maximum strain, and (iv) a loading frequency of 0.5 Hz at 40 ºC and 3% maximum strain are compared with the results of the fuzzy model. It can be seen that the neuro-fuzzy model of NiTi wires successfully reproduces the experimental hysteresis loops at each condition.

4.6 Closure

In this section, a fuzzy model with three inputs (strain, strain rate and temperature) and a single output (stress) is created. The initial arbitrary parameters of the fuzzy model are adjusted by ANFIS in order to successfully map given inputs to correct stress value. It is shown that the model can satisfactorily predict strain-stress loops of superelastic SMAs for given loading frequency and temperature. Since the developed model has the ability of simulating material response at dynamic loading rates and at different temperatures, the model can be used to investigate all potentialities of SMAs for seismic applications.

In the next sections, developed fuzzy model is implemented into numerical simulations in order to explore the feasibility of SMA-based isolation systems.

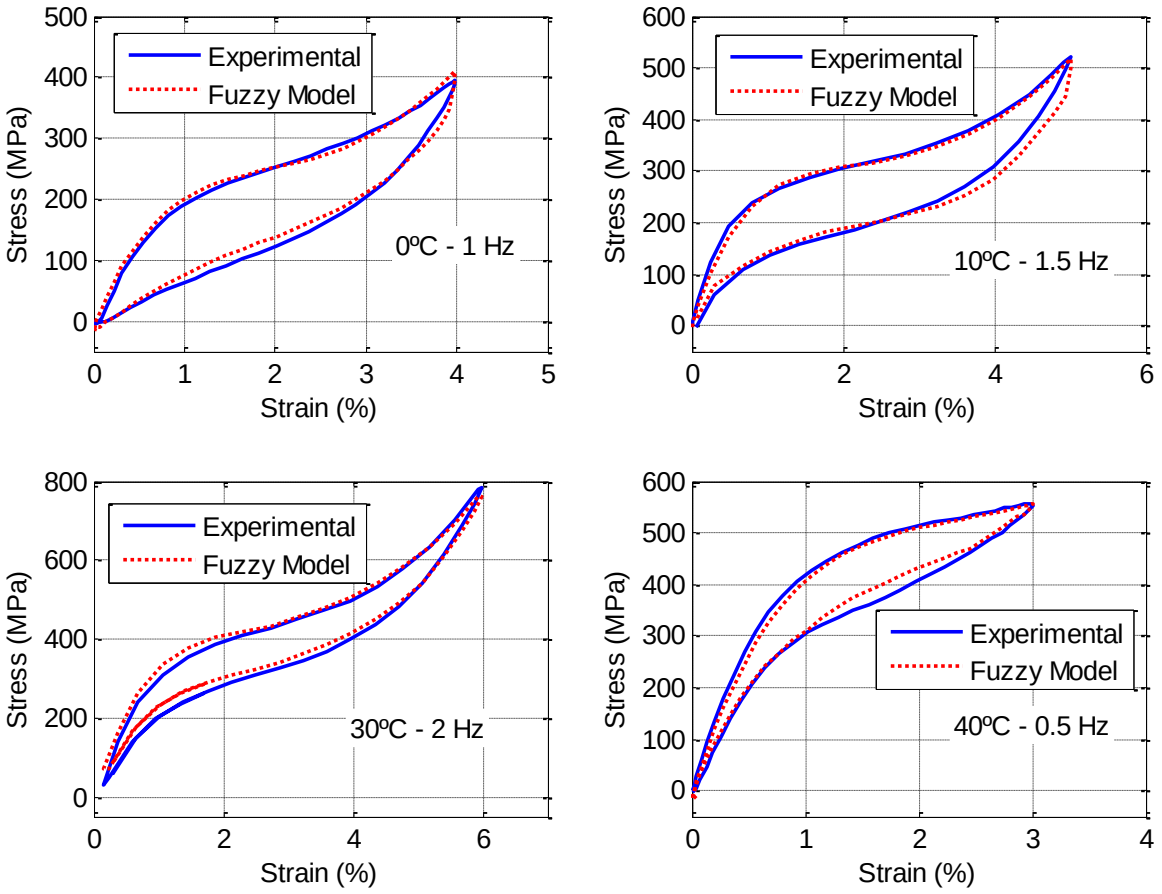

Figure 4-7 Model validation: Hysteresis loops at various conditions for experimental results and ANFIS prediction

5. SUPERELASTIC-FRICTION BASE ISOLATORS

5.1 Introduction

The focus of this section is to investigate the optimum design parameters of a superelastic-friction base isolator (S-FBI) that is installed between piers and superstructure on a bridge to reduce structural responses during near-field earthquakes. The S-FBI system consists of a steel-Teflon sliding bearing that filters out the earthquake forces by providing frictional sliding interfaces and a superelastic SMA device that provides a re-centering mechanism and absorbs seismic energy through hysteresis of SMA elements (Ozbulut and Hurlebaus, 2010b).

First, the model of a three-span continuous bridge with the S-FBI system is developed as a two-degrees-of-freedom system. In order to generate near-field earthquakes that are used as external excitations in the simulations, the time domain response spectral matching of six historical records is performed with the program RspMatch2005. Next, a sensitivity analysis is performed to evaluate the optimum values of design parameters of the S-FBI system for mitigating the response of the highway bridges against near-field earthquakes. Also, the effect of the outside temperature on the performance of the S-FBI system is investigated. In order to assess the benefits of the S-FBI system, the performance of a bridge isolated by an optimal S-FBI system is compared with the response of a comparable non-isolated bridge and same bridge isolated by the P-F isolation system.

5.2 Model of Isolated Bridge Structure

A three-span continuous bridge shown in Figure 5-1 is selected for the sensitivity analysis (Wang *et al.*, 1998). The deck of the bridge has a mass of 771.12×10^3 kg, and the mass of each pier is 39.26×10^3 kg. The bridge has a total length of 90 m, and each pier is 8 m tall. The moment of inertia of piers and Young's modulus of elasticity are given as 0.64 m^4 and 20.67×10^9 N/m^2, respectively. The fundamental period of the non-isolated bridge in the longitudinal direction is 0.45 s. The isolated bridge is modeled as a two-degree-of-freedom system with the S-FBI system. It is assumed that required separation distance between bridge deck and abutment is provided, i.e., pounding effects are avoided. Since the isolation systems installed at the abutment and pier have similar characteristics and therefore, the seismic response of the bridge at the abutment and pier have the same trend, only an internal span is modeled. It is also assumed that the bridge superstructure and piers remain elastic during seismic excitation and the assumption is reasonable in the context of base isolation. The equations of motion are given as

$$\begin{aligned} &m_1\ddot{u}_1(t) + c_1\dot{u}_1(t) + k_1u_1(t) - F_{IS}(u_1, \dot{u}_1, u_2, \dot{u}_2, t) = -m_1\ddot{u}_g(t) \\ &m_2\ddot{u}_2(t) + F_{IS}(u_1, \dot{u}_1, u_2, \dot{u}_2, t) = -m_2\ddot{u}_g(t) \end{aligned} \tag{5-1}$$

where m_1, m_2 and u_1, u_2 are the masses and displacements of the pier and deck, respectively, c_1 and k_1 represent the coefficient of damping and stiffness of piers, and $\ddot{u}_g$ is the ground acceleration. F_{IS} denotes the restoring force of the S-FBI system. Hence, F_{IS} is the sum of the nonlinear force of the SMA device and frictional resistance force of steel-Teflon sliding bearings.

In order to analyze dynamic response of structures with sliding systems, two different numerical models, namely conventional friction and continuous hysteretic models, have been used by researchers in the past. In a conventional model, the frictional force of the isolation system is evaluated by solving a different set of equations for sliding and non-sliding phases (Bozzo and Barbat, 1995). On the other hand, the hysteretic model is a continuous model, and the frictional force can be obtained from a modified viscoplastic model developed by Constantinou *et al.* (1990). Although in terms of computational efficiency and applicability to general computer code the two models are found to have relative advantages and disadvantages, it is also observed that both models predict the seismic response of sliding isolation systems similarly (Jangid, 2005a). Here, the hysteretic model is used to simulate the force of the sliding bearings (Constantinou *et al.*, 1990). The frictional force at a sliding interface is given by

$$F_f = \mu W Z \tag{5-2}$$

where μ represents the coefficient of friction, W is the normal load carried by the bearing interface, and Z is a hysteretic dimensionless quantity computed from following equation

$$Y\dot{Z} + \gamma|\dot{u}_b\|Z|Z|^{n-1} + \beta\dot{u}_b|Z|^n - \dot{u}_b = 0, \tag{5-3}$$

where Y is the yield displacement of the sliding bearing chosen as 0.0005 m and, γ, β, and n are dimensionless parameters that control the shape of the hysteretic curve and have the values of 0.9, 0.1 and 1, respectively. Also, $u_b = u_2$-u_1 is the deformation of the sliding bearings. The fuzzy model described in previous section is used to compute the instantaneous force from the SMA elements.

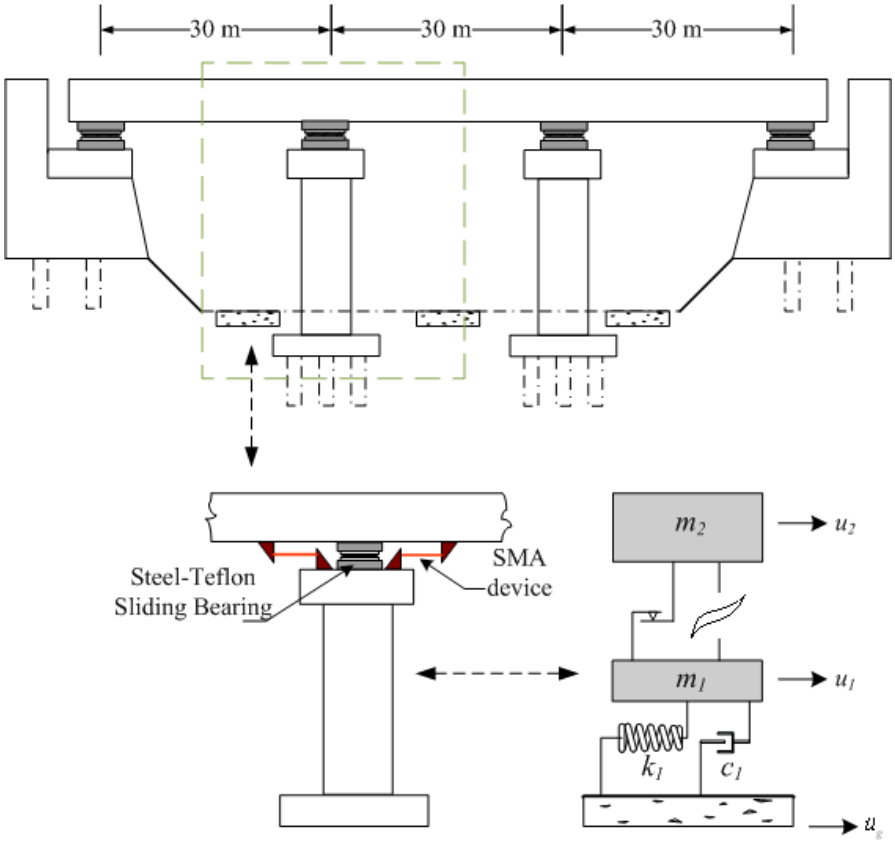

Figure 5-1 Model of a three-span isolated bridge

5.3 Ground Motions Used for Analyses

Selection and modification of ground motion records that are used in dynamic time history analyses have a significant influence on the results of the analyses. The ground motion records mainly fall into three categories: (i) artificial accelerograms, (ii) synthetic accelerograms generated from seismological source models and (iii) real accelerograms recorded during earthquakes (Bommer and Acevedo, 2004). Several programs developed to generate seismic records belong to the first two categories

mentioned above are freely available to engineers. Nevertheless, it has been pointed out that the strong-motion accelerograms generated by using these methods have several drawbacks such as having unreasonably high energy content or requiring definition of many parameters to characterize earthquake source (Bommer and Acevedo, 2004). Since real accelerograms do not possess these shortcomings by definition and are increasingly available via digital seismic networks, they are becoming the most attractive option for dynamic time-history analyses. However, selection and scaling of real records for dynamic analysis of structures requires special attention. A review on different strategies used for selection of real ground motion records can be found in (Iervolino and Manfredi, 2009). An evaluation of the earlier works related to record selection points out that the spectral shape is the most important ground motion characteristic in modification of real records (Iervolino *et al.*, 2009).

A variety of methods have been proposed to modify a historical time history so that its response spectrum is compatible with a given target spectrum (Preumont, 1984). One approach used commonly for generating response spectrum compatible ground motions is to adjust Fourier amplitude spectra in the frequency domain. Although it is a straight-forward method and provides a close match to the target spectrum, it also has significant potential problems such as distorting the energy characteristics of accelerograms and producing very unrealistic seismic demands (Naeim and Lew, 1994). Hancock *et al.* (2006) have proposed an alternative approach that performs spectral matching in time domain using wavelets. The method, known as RspMatch2005, can simultaneously match spectra at multiple damping values while preserving the non-

stationary character of the reference time history. Unlike the spectral matching in the frequency domain, RspMatch2005 does not corrupt the velocity and displacement time histories and avoids creating ground motions with unrealistic energy content. In this study, the program RspMatch2005 is used to generate spectrum compatible real ground motion records for dynamic time history analyses of the isolated bridge.

A response spectrum constructed as per the International Building Code (IBC, 2000) for a site in southern California, assuming firm rock conditions is selected as the target spectrum (Malhotra, 2003). A total of six historical California earthquakes which present near-field characteristics are selected as seed accelerograms. The characteristics of the ground motions such as magnitude, the closest distance to the fault plane, peak ground acceleration and velocity, and significant duration are given in Table 5-1. Figure 5-2 shows the target response spectrum used in the analysis and response spectra of selected ground motions for 5% damping level.

Table 5-1 Description of the ground motions used in the analyses

Earthquake	Magnitude (M_w)	Distance (km)	PGA (g)	PGV (cm/s)	Duration (s)
1979 Imperial Valley	6.5	1.0	0.44	109.8	8.5
1986 N. Palm Springs	6.0	8.2	0.59	73.3	4.5
1994 Sylmar	6.7	6.2	0.90	102.8	9.0
1971 San Fernando	6.6	2.8	1.22	112.5	3.8
1992 Landers	7.3	1.1	0.72	97.6	13.1
1989 Loma Prieta	6.9	6.1	0.56	94.8	10.2

The selected seed accelerograms are adjusted using RspMatch2005 in order to simultaneously match 5%, 10% and 25%-damped response spectra. Figure 5-3 shows the spectrally matched response spectrum of Landers and Loma Prieta earthquakes for different damping levels. Note that spectral misfit is reduced significantly for all damping levels.

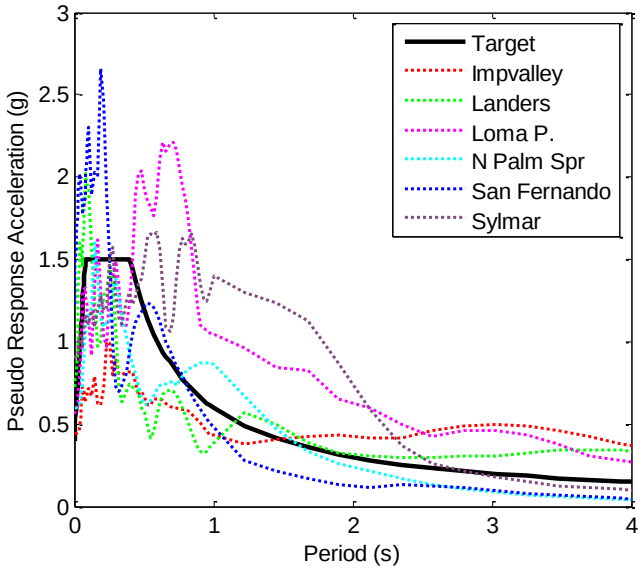

Figure 5-2 The target response spectrum compared to response spectra of the selected ground motions

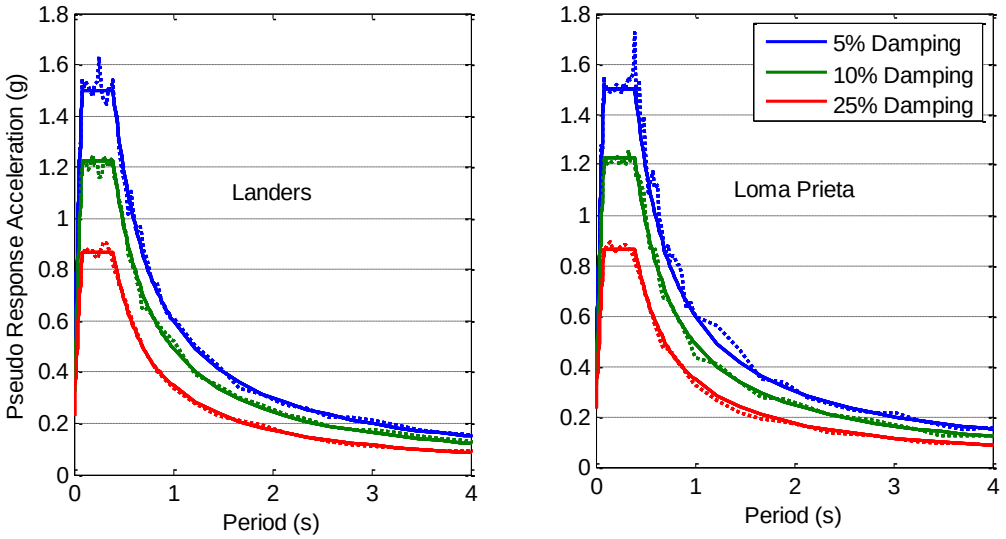

Figure 5-3 The spectrally matched response spectra of Landers and Loma Prieta earthquakes for different damping levels

5.4 Sensitivity Analysis

In this section, the optimum design parameters of the S-FBI system for seismic protection of bridges against near-field earthquakes are investigated. Figure 5-4 shows the typical force-deformation curves of the sub-components of the S-FBI system, i.e. the SMA device and steel-Teflon sliding bearing and the combined hysteresis.

Although the cost of SMA material has decreased significantly in the past decade (Ocel *et al.*, 2004), it has been one of the impediments to actual implementation. Yet, economically feasible solutions can be attained with Ni-Ti based SMAs if they are used in small devices or applied to selected region of structures (Janke *et al.*, 2005). The SMA device considered in this study has a straightforward design, which avoids extra

fabrication costs. It simply consists of multiple loops of superelastic NiTi wires wrapped around two wheels.

The S-FBI system is characterized by the natural period of the isolated bridge T_b, the forward transformation displacement of the SMA device u_y, and the friction coefficient of sliding bearings μ. The natural period of the isolated bridge can be computed as

$$T_b = 2\pi\sqrt{\frac{m_d}{\sum \alpha k_{SMA}}}, \tag{5-4}$$

where m_d is the mass of the bridge deck and αk_{SMA} denotes post forward transformation stiffness of the SMA device. Here, α which represents the ratio of post forward transformation stiffness and initial stiffness of the SMA device is taken as 0.1 and the forward transformation strain of SMA wires is chosen to be 1%, which are typical values for NiTi shape memory alloy wires. Hence, the design of the S-FBI system requires the specification of three parameters: T_b and u_y (to determine the area and the length of SMA wires) and μ.

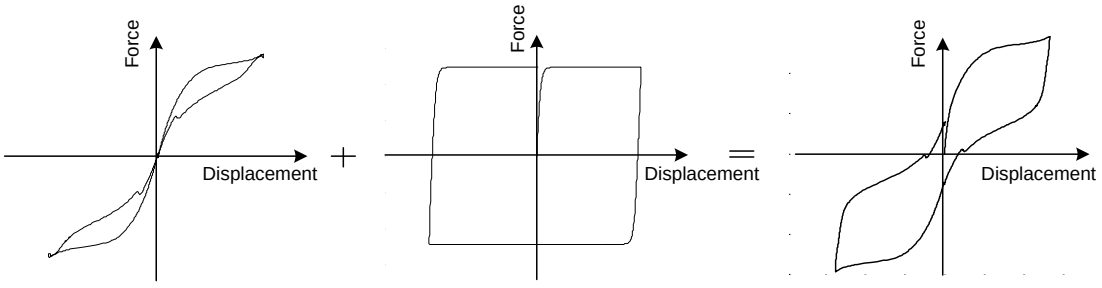

Figure 5-4 Force-deformation curves of the S-FBI system and its sub-components

5.5 Results of Sensitivity Analysis

In order to evaluate the effects of these design parameters of the S-FBI system on the seismic response of the bridge, nonlinear time-history analyses are performed by solving the governing equations of motion of the isolated bridge. As external excitation, the six near-field ground motion records described above are employed. The response quantities evaluated here are peak relative displacement of the deck, peak absolute acceleration of the deck and peak base shear normalized by the weight of the deck.

5.5.1 Effect of Isolation Period T_b

Figure 5-5 illustrates the variation of peak response quantities with the natural period of the isolated bridge for various earthquakes. The values of μ and u_y are selected as 0.10 and 30 mm, respectively. It can be seen that the peak deck acceleration rapidly decreases when the isolation period increases. On the other hand, the peak deck drift starts to increase for some excitation cases with the increasing isolation period. Also, the peak normalized base shear decreases when the isolation period increases from 2.0 s to about 3.5 s. However, for the higher values of isolation period, it remains nearly constant.

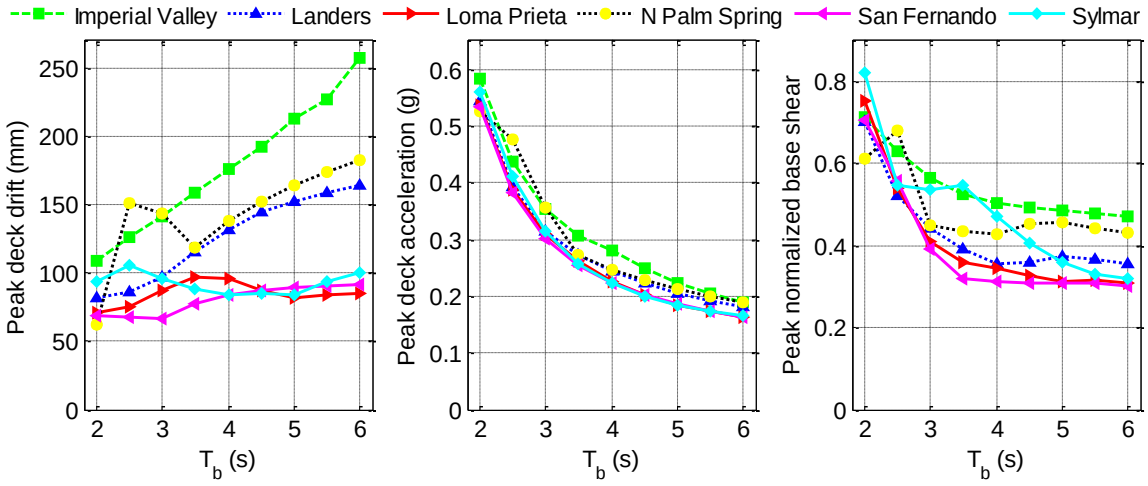

Figure 5-5 Variations of peak response quantities with the natural period of the isolated bridge

5.5.2 Effect of Friction Coefficient of Sliding Bearings μ

The variation of peak response quantities for different values of the friction coefficient of the sliding bearings is shown in Figure 5-6 considering T_b = 4.0 s and u_y = 30 mm. It can be seen that increasing the friction coefficient regularly decreases the peak deck drift while increasing the peak deck acceleration. However, note that the increase in the peak deck acceleration occurs almost at a constant rate while the rate of the decrease in the peak deck drift reduces at larger values of μ. Moreover, for most excitation cases, the peak normalized base shear initially decreases with an increase in μ and then it tends to increase for higher values of μ.

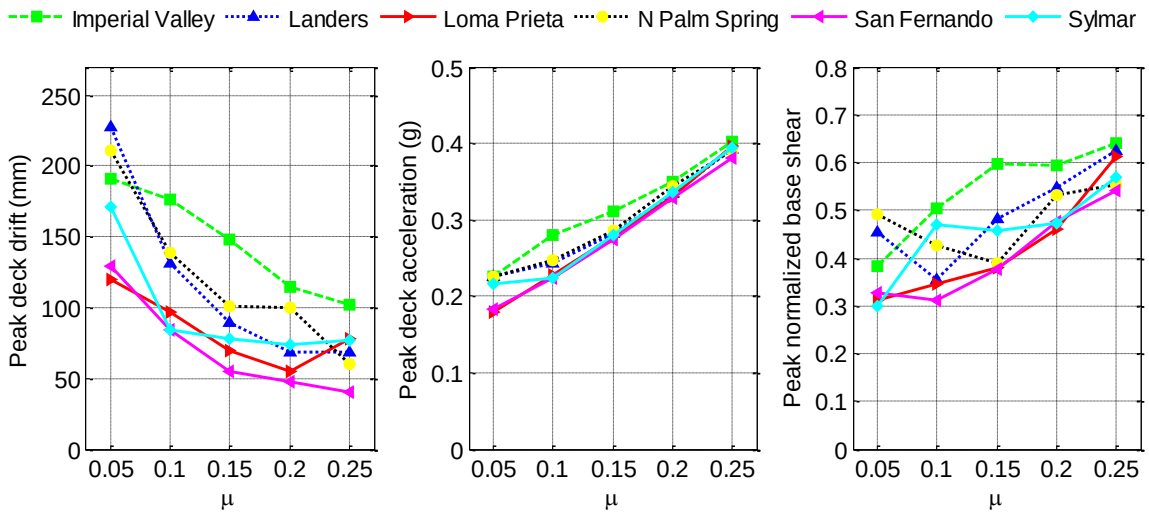

Figure 5-6 Variation of peak response quantities with friction coefficient of sliding bearings

The effect of interaction between the isolation period T_b and the friction coefficient of sliding bearings μ is examined through three-dimensional (3-D) plots shown in Figure 5-7 through Figure 5-9 . Each of these 3-D plots presents the variation of peak response quantities of the isolated bridge with respect to isolation period and friction coefficient simultaneously for different near-field earthquakes. As shown in Figure 5-7, the peak deck drift has large values for small values of the friction coefficient and reduces with an increase in the friction coefficient almost for all isolation periods. However, the rate of this reduction rapidly decreases and the surface becomes substantially flat when the friction coefficient is over 0.15 for most of the excitations. Also, there exists an increase in the peak deck drift for the increasing values of isolation period, yet; the isolation period seems to have negligible effect when the friction coefficient is large. It can be seen from Figure 5-8 and Figure 5-9 that the peak deck

acceleration and normalized base shear attain high values for small values of isolation period for various friction coefficient values. The larger values of isolation period ameliorate the acceleration response of the deck and decrease the normalized base shear. Note that the highest values of peak deck acceleration and normalized base shear is observed for the smallest T_b and largest μ while peak deck drift has its largest value for the largest T_b and smallest μ.

It can be concluded from the observations in Figure 5-5 through Figure 5-9 that the optimal value of isolation period T_b which effectively reduces the deck drift and simultaneously control superstructure acceleration is between 3.5s and 4s. Also, the optimum value of the friction coefficient μ of an S-FBI system used for seismic response control of bridges against near-field earthquakes is in the vicinity of 0.15. Increasing μ over 0.15 reduces deck displacement slightly more at an expense of considerable increase in peak acceleration response of the deck and peak normalized base shear.

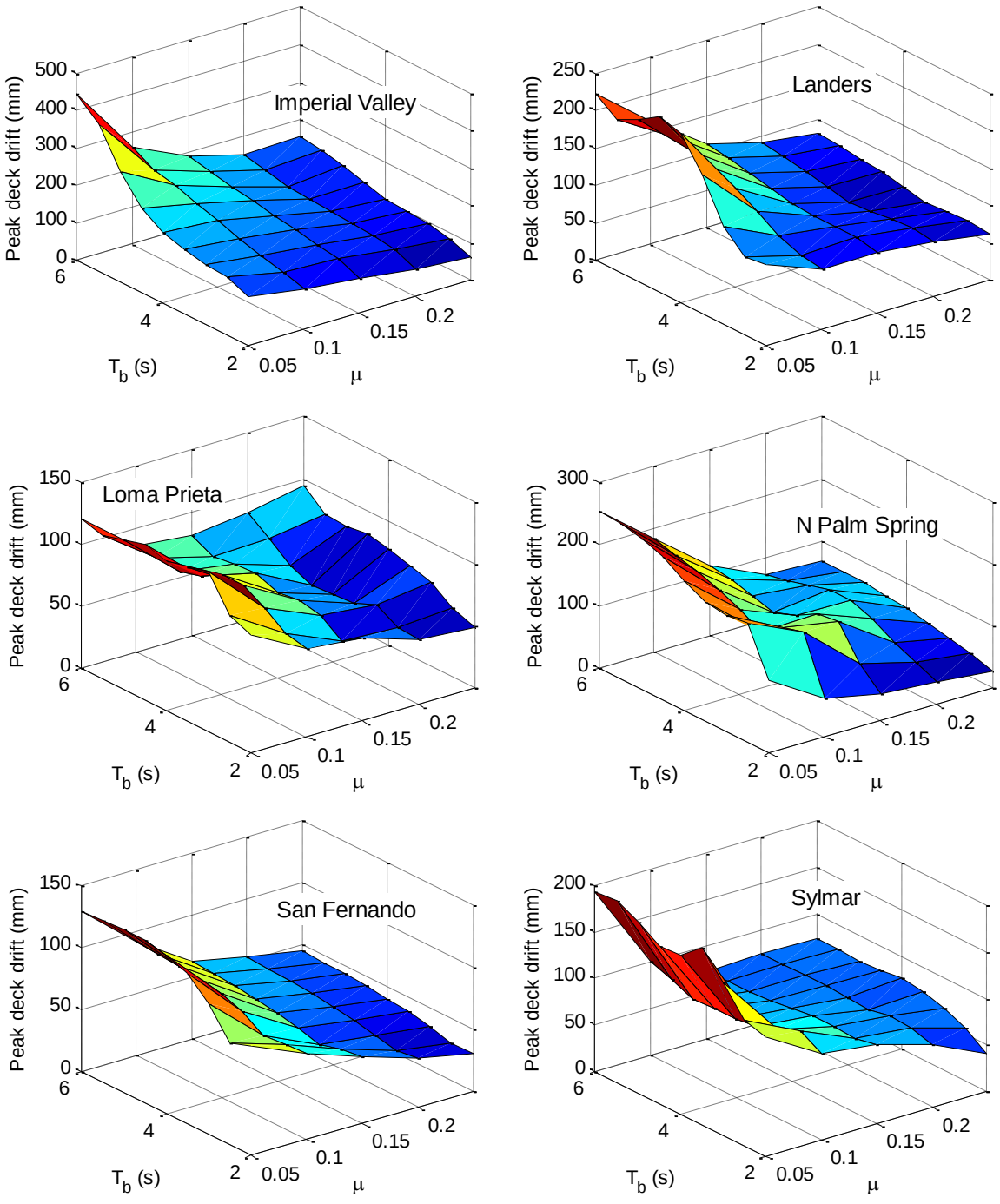

Figure 5-7 Variations of peak deck drift with isolation period and friction coefficient

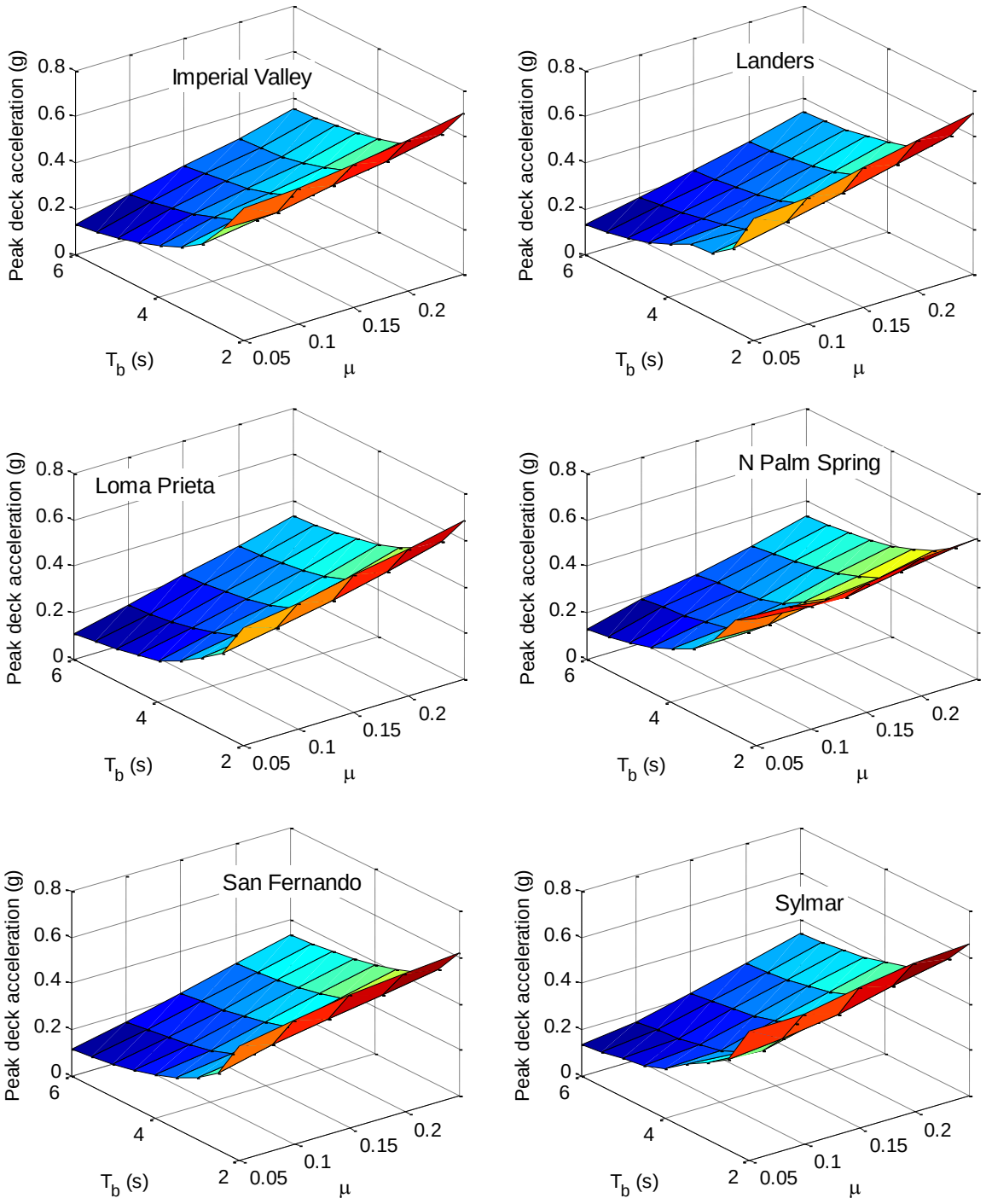

Figure 5-8 Variations of peak deck acceleration with isolation period and friction coefficient

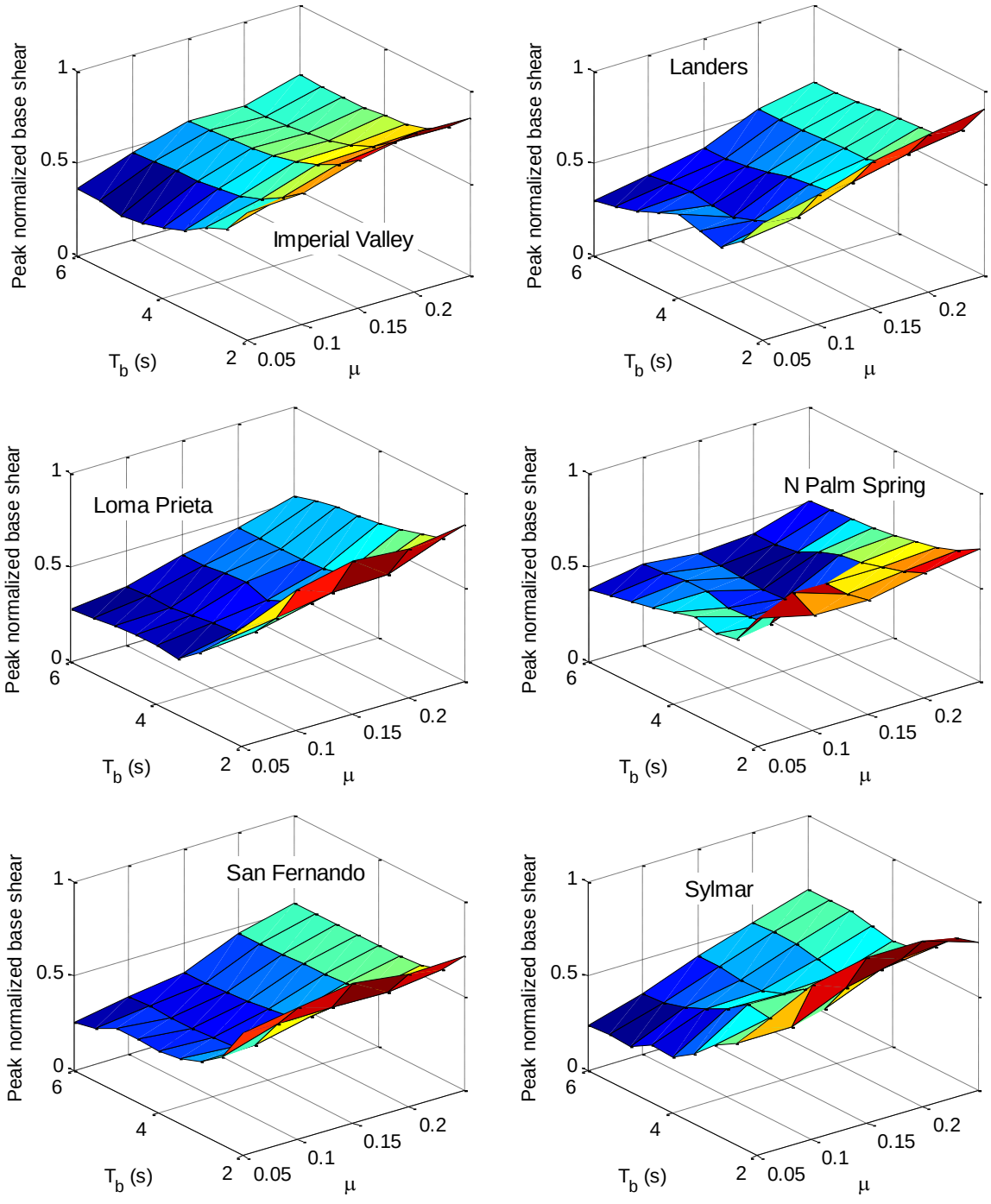

Figure 5-9 Variations of peak normalized base shear with isolation period and friction coefficient

5.5.3 Effect of Forward Transformation Displacement of the SMA Device u_y

Figure 5-10 shows the effect of forward transformation displacement of the SMA device on the peak response quantities for different near-field ground motions. The results are obtained for T_b = 4.0 s and μ = 0.10. It is observed that there is not a considerable change in the peak response of the isolated bridge for different values of u_y. Nevertheless, a moderate increase in peak deck acceleration and a modest decrease in peak deck drift for some excitation cases are present. Also, there is a slight increase in peak normalized base shear for some earthquakes for higher values of u_y. Since the larger values of u_y imply longer SMA wire length, the value of u_y can be kept small (between 20-30 mm) without any performance degradation in order to reduce the amount of SMA material needed. Note that further reducing the forward transformation displacement (u_y < 20 mm) results in large strain values for SMA wire. Since the maximum superelastic strain is about 6% for NiTi wires and significant strain hardening occurs for the larger strain values, the seismic demand on piers may considerable increase for very small values of u_y.

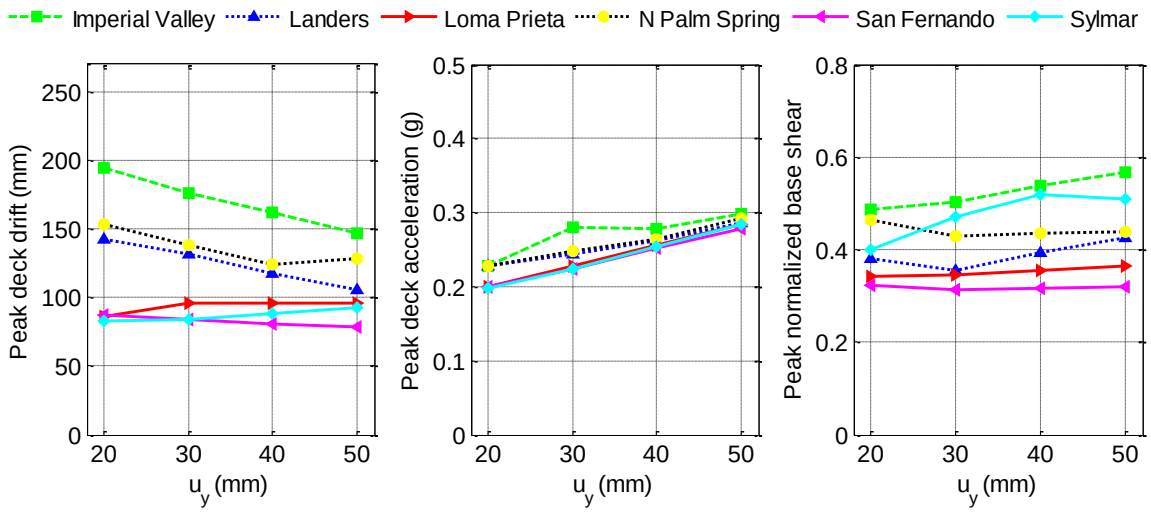

Figure 5-10 Variations of peak response quantities with forward transformation displacement of the SMA device

5.5.4 Effect of Ambient Temperature

Since the mechanical properties of both SMA wires and steel-Teflon sliding bearings are considerably influenced by environmental temperature changes, the effect of outside temperature on the performance of the S-FBI system is investigated. In order to consider the temperature effect on the friction coefficient of steel-Teflon bearings, the friction coefficient is computed as

$$\mu = \mu_{\max} - \Delta\mu \exp(-a|\dot{u}_b|), \tag{5-5}$$

where μ_{max} is the coefficient of friction at very high velocities, $\Delta\mu$ is the difference between the coefficient of friction at very high and very low velocities, and a is a constant. Dolce *et al.* (2005a) specified the parameters μ_{max}, $\Delta\mu$, and a for different combination of bearing pressure, condition of interface and temperature. Here, the values of μ_{max}, $\Delta\mu$, and a for three different temperatures and for a 28.1 MPa bearing

pressure and non-lubricated bearing interface are approximated from the study of Dolce *et al.* (2005a) and given in Table 5-2. The fuzzy model described earlier is used to predict the force of the SMA device at different temperatures. The values of T_b and u_y are selected as 4.0 s and 30 mm, respectively.

Table 5-2 Model parameters for different temperatures

T (°C)	μ_{max} *(%)*	$\Delta\mu$ *(%)*	*a (m/s)*
0	11.07	6.78	23.3
20	10.26	7.13	22
40	9.86	7.11	18.7

The influence of temperature changes on peak response quantities of the isolated bridge is illustrated in Figure 5-11 . It can be seen that the effectiveness of the S-FBI system in reducing peak deck drift mostly increases with an increase in temperature. As temperature reduces to 0°C compared to a reference temperature of 20°C, the peak deck drift experience a maximum of 31% increase for the San Fernando earthquake; yet, the increase is in the range of 2-10% for all other cases. On the other hand, there is a maximum of 19% reduction in peak deck drift when the outside temperature rises to 40°C from its reference value. It is also observed that peak deck acceleration attains larger values as temperature increases. In particular, it changes about $\pm 10\%$ when temperature differs ± 20°C from the reference temperature of 20°C. Furthermore, seismic demand on piers experience an increase when temperature increase to 40°C

compared to reference temperature, while it reduce as temperature drops to 0°C for all cases except the San Fernando and Loma Prieta earthquakes. Note that the changes in the peak base shear are in the range of 2-19%. Overall, it can be concluded that a ±20°C variation in environmental temperature compared to the reference temperature of 20°C does not significantly affect the performance of the S-FBI system.

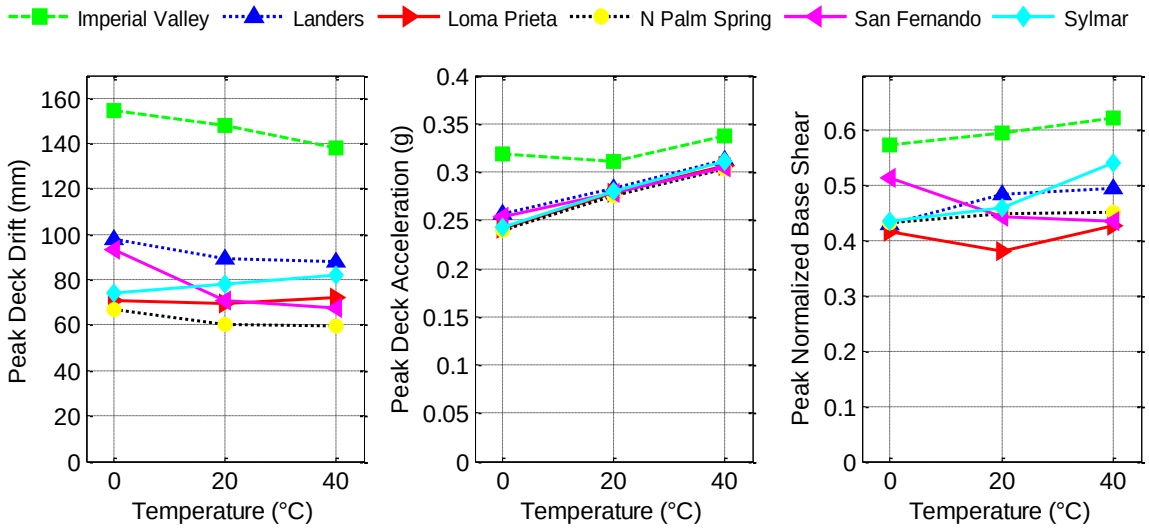

Figure 5-11 Variations of peak response quantities with environmental temperature

5.5.5 Time Histories of Response Quantities

The time histories of various response quantities of the bridge isolated by the S-FBI system, and the force-deformation curves of the SMA device and the steel-Teflon sliding bearings as well as the overall S-FBI isolation system are illustrated in Figure 5-12 Figure 5-13 , and Figure 5-14 for the Imperial Valley earthquake. The same results are presented for the Loma Prieta earthquake in Figure 5-15 Figure 5-16, and Figure

5-17. The peak values of each response quantity are also given in the figures. The S-FBI system parameters T_b, u_y, μ are specified as 4.0 s, 30 mm, and 0.10, respectively. In order to serve as a benchmark for evaluating effectiveness of the S-FBI system, the responses of the bridge isolated by pure-friction (P-F) base isolation system with a friction coefficient of 0.10 are also shown in the figures mentioned above. Moreover, the peak values of each response quantity of the non-isolated bridge are provided in Table 5-3 for the same comparison purposes.

It can be seen that the isolation of bridge with the S-FBI system significantly decreases the peak deck acceleration when compared with the non-isolated bridge. Note that as compared to P-F system, the bridge isolated by the S-FBI system produces 63% and 66% more reduction in the peak deck acceleration for Imperial Valley and Loma Prieta earthquakes, respectively. Also, in comparison with the non-isolated bridge, peak normalized base shear experiences 69% and 73% decreases for Imperial Valley earthquake and 82% and 85% decreases for Loma Prieta earthquake when the bridge is isolated by the S-FBI system or the P-F system, respectively. Moreover, the S-FBI system successfully reduces the peak bearing deformations and recovers the deformations after the seismic event. On the other hand, the P-F system experience excessive deformations and has large residual deformations since it lacks re-storing force capability.

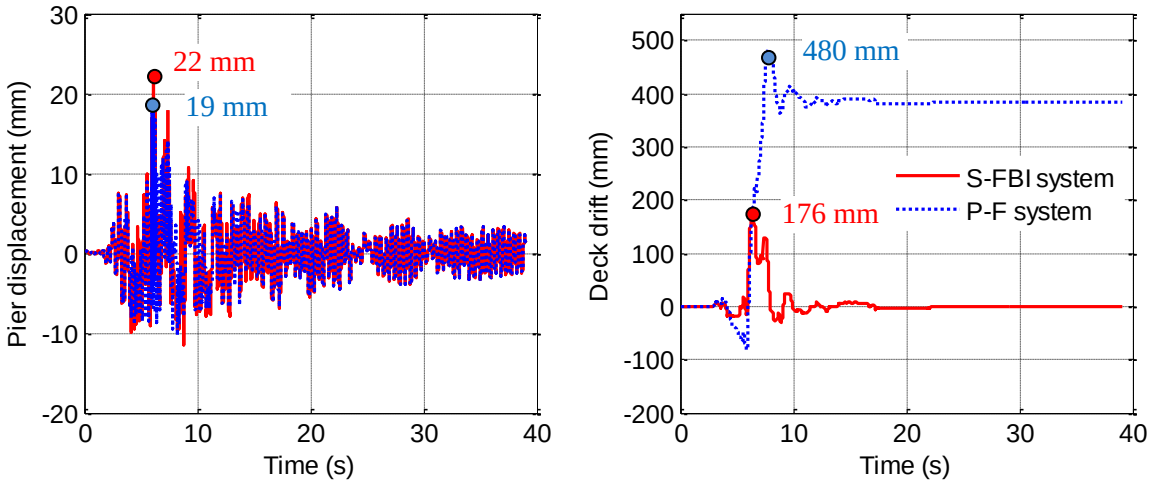

Figure 5-12 Time histories of pier displacement and deck drift for a bridge isolated by the S-FBI system or the P-F system under Imperial Valley earthquake

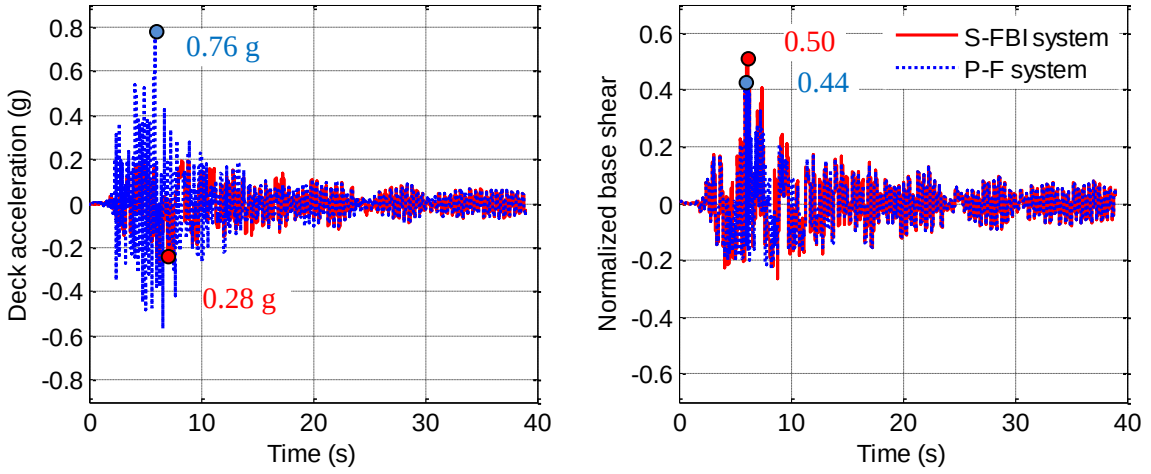

Figure 5-13 Time histories of deck acceleration and normalized base shear for a bridge isolated by the S-FBI system or the P-F system under Imperial Valley earthquake

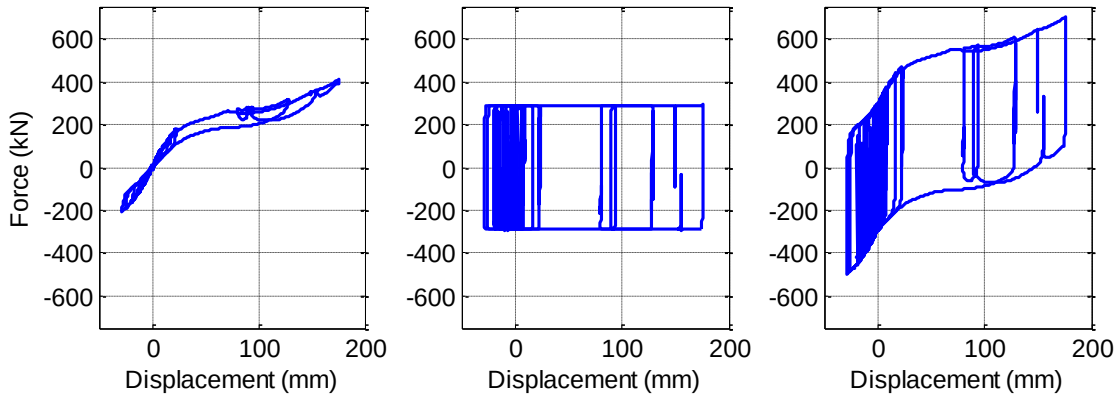

Figure 5-14 Force-deformation curves of the S-FBI system and its sub-components under Imperial Valley earthquake

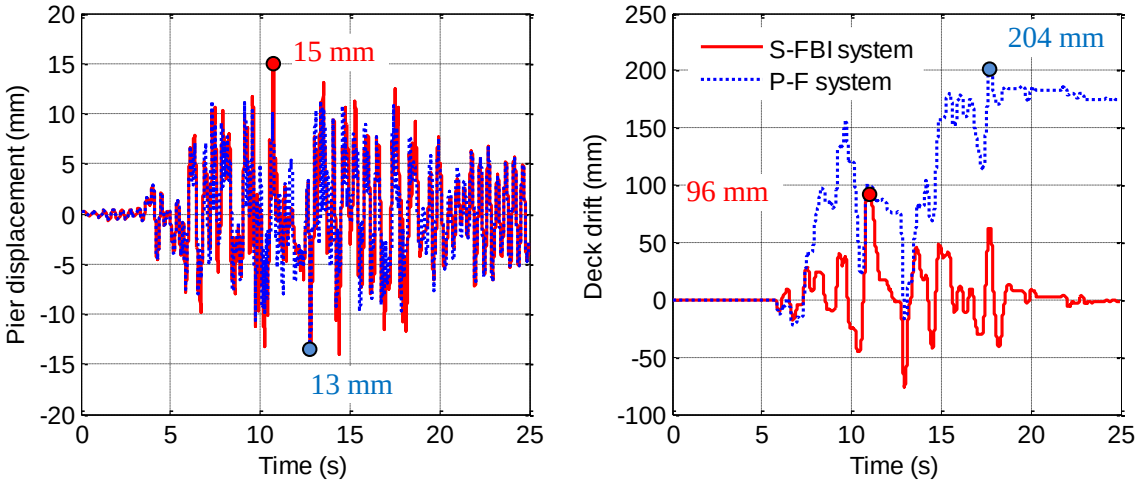

Figure 5-15 Time histories of pier displacement and deck drift for a bridge isolated by the S-FBI system or the P-F system under Loma Prieta earthquake

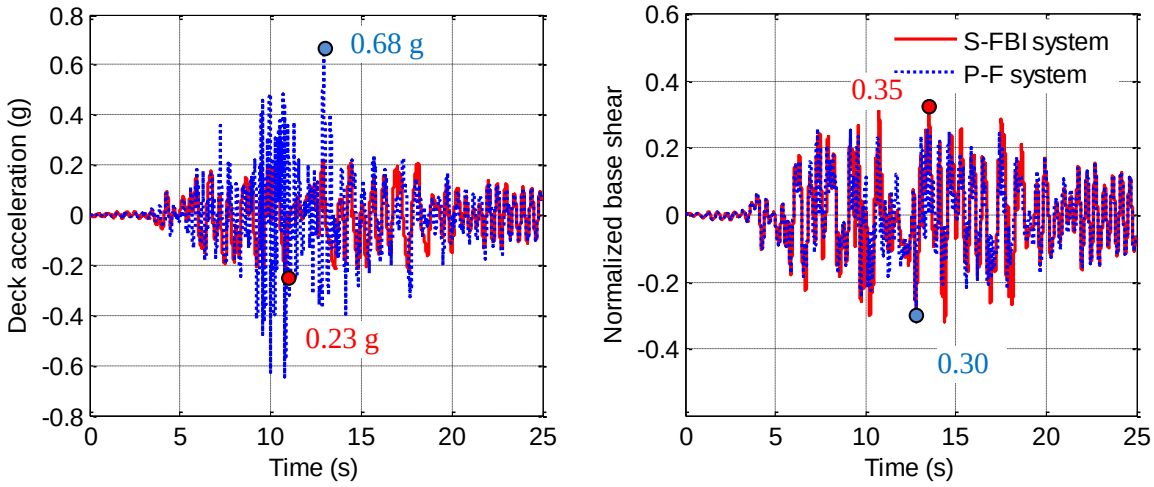

Figure 5-16 Time histories of deck acceleration and normalized base shear for a bridge isolated by the S-FBI system or the P-F system under Loma Prieta earthquake

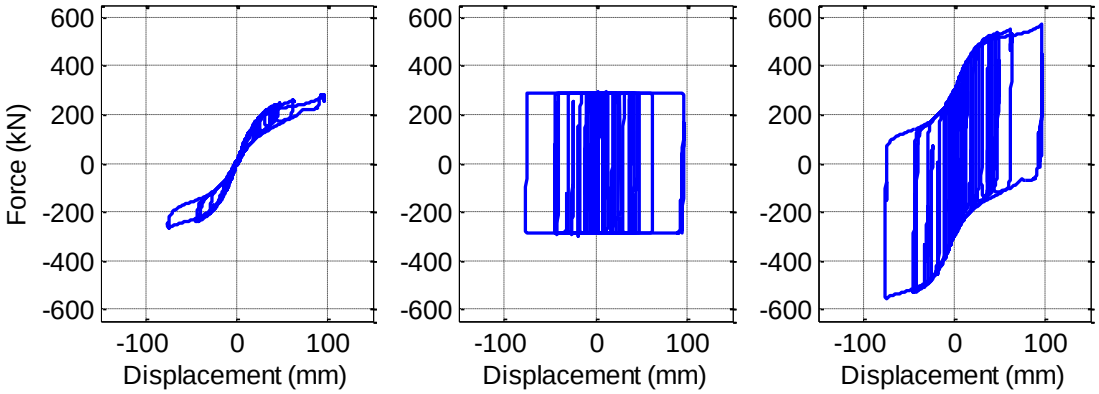

Figure 5-17 Force-deformation curves of the S-FBI system and its sub-components under Loma Prieta earthquake

Table 5-3 Peak response quantities for the non-isolated bridge

Responses of non-isolated bridge	Imperial Valley	Loma Prieta
Peak deck drift (mm)	73	86
Peak deck acceleration (g)	1.92	2.27
Peak normalized base shear	1.62	1.99

5.6 Closure

In this section, the optimum design parameters of a superelastic-friction base isolation system are explored for seismic protection of highway bridges subjected to near-field earthquakes. The S-FBI system consists of a steel-Teflon sliding bearing and an SMA device. While the sliding bearing decouples the superstructure of the bridge from its piers and dissipates energy through friction, the SMA device provides restoring force and additional damping. The design parameters of the S-FBI system chosen for the investigation includes the natural period of the isolated bridge T_b, the forward transformation displacement of the SMA device u_y, and the friction coefficient of sliding bearings μ. In order to generate ground motions used in the simulations, a time domain method which employs wavelets to adjust real accelerograms to match a target response spectrum with minimum changes on the other characteristics of ground motions is used. Time-history analyses of the isolated bridge are performed to evaluate the variation of peak response quantities with the design parameters of the S-FBI system.

It is found that the optimum value of T_b based on restraining both displacement and acceleration response of the deck is in the range of 3.5 s - 4.0 s under near-field

earthquakes. Also, it is observed that peak response quantities are not much influenced by the variation of the forward transformation displacement of the SMA device. Therefore, smaller values are recommended for u_y in order to reduce the length of the SMA elements used for the device. It is also noted that increasing the friction coefficient ameliorates peak displacement response of the deck while adversely affecting the peak acceleration response of the deck. It can be said that selecting a value between 0.10 and 0.15 for μ yields optimum results for isolated bridges subjected to near-field motions. Finally, it is shown that there is not a significant change in the response of the bridge isolated by the S-FBI system as temperature varies in the range of 0 - 40°C. The results indicate that the S-FBI system can effectively mitigate the response of highway bridges against near-field earthquakes when the design parameters of the S-FBI system are judiciously selected.

6. SHAPE MEMORY ALLOY/RUBBER-BASED ISOLATION SYSTEM

6.1 Introduction

Among various isolation systems that have been proposed, rubber isolation systems have been widely studied and used throughout the world (Tyler, 1991). Laminated-rubber bearings have considerable lateral flexibility, vertical load-carrying capacity and restoring force capability. The commonly used rubber isolation systems combine laminated-rubber bearings and some mechanical dampers such as hydraulic dampers, viscous dampers, steel bars or lead-plugs within the bearing itself. Laminated-rubber bearing with lead core, known as lead-rubber bearing, is the most popular rubber isolation system. Another widespread rubber isolator is high-damping rubber bearings which increases the damping of the isolation system by incorporating damping in the elastomer itself (Bozorgnia and Bertero, 2004). In recent years, several attempts have been made to combine smart materials with rubber bearings (Yoshioka *et al.*, 2002; Usman *et al.*, 2009). One such material is a shape memory alloy.

In this section, a sensitivity analysis is conducted in order to investigate the effectiveness of an SMA/rubber-based (SRB) isolation system for protecting highway bridges against near-field earthquakes (Ozbulut and Hurlebaus, 2010c). The smart isolation system consists of a laminated rubber bearing that decouples the superstructure from the bridge piers and an SMA device that provides additional energy dissipation and re-centering capacity. First, a three-span continuous bridge is modeled together with laminated-rubber bearings and an auxiliary SMA device. Nonlinear time-history

analyses of the isolated bridge are performed for a total of six excitation cases. A time-domain method, which spectrally adjusts time histories of historical ground motions to match a target spectrum at multiple damping levels, is employed to generate artificial earthquakes that are used for dynamic analyses. The variation of seismic response of the isolated bridge with the normalized forward transformation strength of the SMA device F_o, the forward transformation displacement of the SMA device u_y, the pre-strain level of the SMA wires, the lateral stiffness of the laminated rubber bearings k_b and environmental temperature changes is investigated. The bridge response quantities evaluated in the sensitivity analysis include peak values of deck drift, deck acceleration, and normalized base shear.

6.2 Model of Isolated Bridge Structure

The three-span continuous bridge described in previous section is also used here for the sensitivity analysis. The equations of motion are given as

$$\begin{aligned} &m_1\ddot{u}_1(t)+c_1\dot{u}_1(t)+k_1u_1(t)-F_{IS}(u_1,\dot{u}_1,u_2,\dot{u}_2,t)=-m_1\ddot{u}_g(t) \\ &m_2\ddot{u}_2(t)+F_{IS}(u_1,\dot{u}_1,u_2,\dot{u}_2,t)=-m_2\ddot{u}_g(t) \end{aligned} \tag{6-1}$$

where m_1, m_2 and u_1, u_2 are the masses and displacements of pier and deck, respectively, c_1 and k_1 represent the coefficient of damping and stiffness of piers, and $\ddot{u}_g$ is the ground acceleration. F_{IS} denotes the sum of the restoring force of the laminated rubber bearings and SMA device. Laminated rubber bearings are modeled by linear spring and dashpot elements. The coefficient of damping and stiffness of rubber bearings are

denoted as c_2 and k_2, respectively in Figure 6-1. The equivalent damping ratio of bearings is selected to be 2%. The fuzzy model described earlier is used to compute the instantaneous force from the SMA elements.

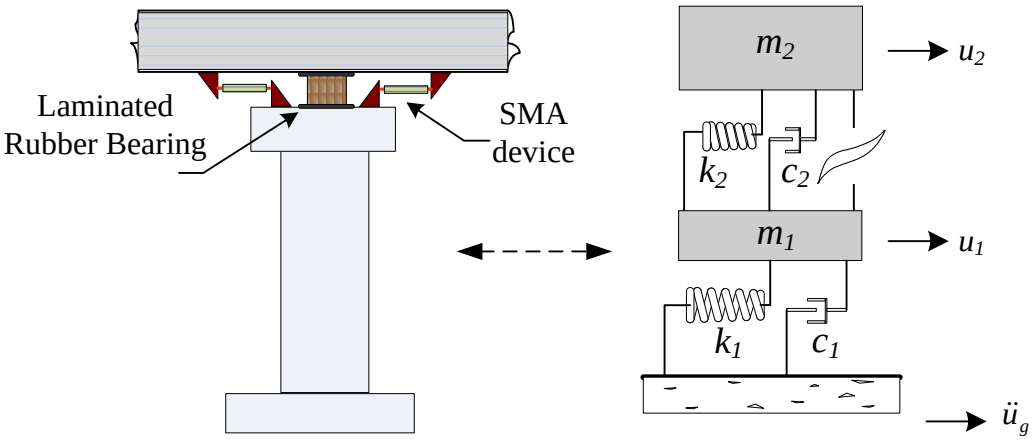

Figure 6-1 Model of an isolated bridge with SMA/rubber isolation system

6.3 Sensitivity Analysis

Several key design parameters for a superelastic SMA device are shown in Figure 6-2 on an idealized force-deformation curve. In the figure, F_y and u_y represent forward transformation force and displacement of the SMA device, respectively; F_d and u_d respectively denote design force and displacement corresponding to the limit of superelastic force-displacement relationship of the SMA device; k_{SMA} and αk_{SMA} denote initial lateral stiffness and post-forward transformation stiffness of the device, respectively. For the NiTi wire considered in this study, α, which represents the ratio of post-forward transformation stiffness and initial stiffness of the SMA device, is observed

to be 0.1; the forward transformation strain of SMA wire ε_y is about 1% and the maximum recovery strain of SMA wire is about 6%. Here, u_y is selected as analysis parameter while u_d can be computed directly for the given u_y. Another parameter for the sensitivity analysis is selected to be the normalized forward transformation strength of the SMA device F_o which is defined as, $F_o = F_y / W_d$ where W_d is the weight of the bridge deck. Note that once u_y and F_y are given, the geometric dimensions of the SMA elements can be computed from

$$u_y = \varepsilon_y \cdot L_{SMA}$$
$$k_{SMA} = \frac{F_y}{u_y} = \frac{A_{SMA} \cdot E_{SMA}}{L_{SMA}}, \tag{6-2}$$

where E_{SMA}, A_{SMA} and L_{SMA} are the Young's modulus, cross-sectional area and length of the SMA wires, respectively.

The effects of the environmental temperature changes on the seismic response of the isolated bridge are also evaluated in this study. Lastly, the pre-strain level of the SMA wires and the lateral stiffness of the laminated rubber bearings k_b are considered as other parameters for the sensitivity study.

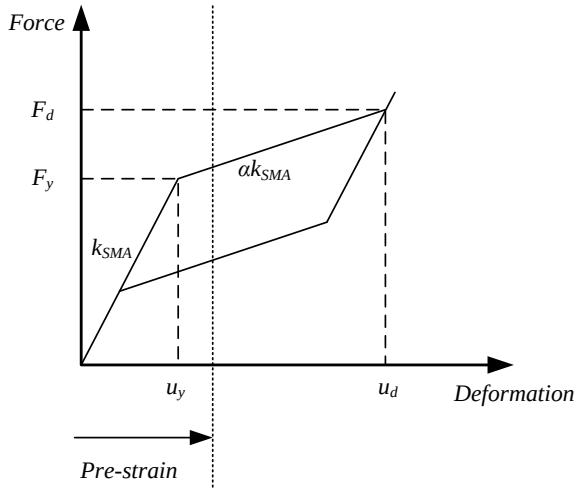

Figure 6-2 Analysis parameters on an idealized force-deformation curve

6.4 Results of Sensitivity Analysis

Numerical simulations of the bridge isolated by the SRB isolation system are conducted in order to assess the influence of the above-described parameters on the seismic response of the isolated bridge. The six spectrally-matched historical ground motion records that are described in previous section are used as external excitations. The response quantities evaluated here are peak relative displacement of the deck, peak absolute acceleration of the deck, and peak base shear normalized by the weight of the deck.

6.4.1 Effect of Normalized Forward Transformation Strength of the SMA Device F_o

Figure 6-3 shows the variation of the peak response quantities with the normalized forward transformation strength of the SMA device. The results are obtained for u_y = 50 mm, T = 20ºC, k_b = 16 kN/cm and without any pre-stress in the SMA wires. It can be seen that initially the peak deck drift almost continuously

decreases for the increasing values of F_o yet the rate of this decrease becomes smaller or even turns to a slight increase when F_o is over 0.30. The peak deck acceleration and the peak normalized base shear take their minimum values in the vicinity of F_o = 0.20-0.25 for most of the excitation cases and then, they start to increases almost constantly for the higher values of F_o. It can be concluded from these observations that the optimal value of F_o which effectively reduces the deck drift and simultaneously controls the superstructure acceleration and demands on the substructure is around 0.25.

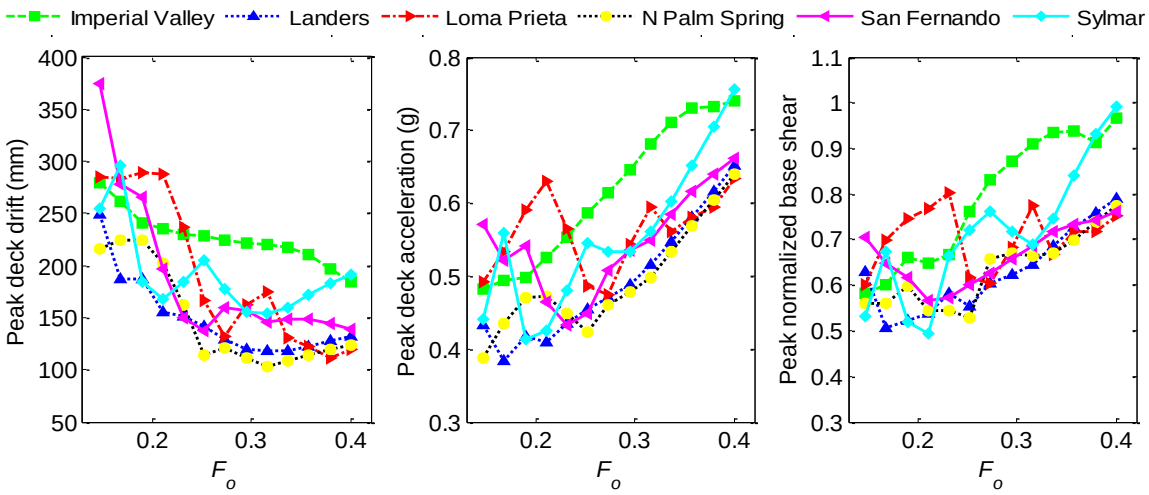

Figure 6-3 Variation of various peak response quantities with the normalized forward transformation strength of SMA device

6.4.2 Effect of Normalized Forward Transformation Displacement of the SMA Device u_y

The variation of the peak deck drift, deck acceleration and normalized base shear with the forward transformation displacement of the SMA device is given in Figure 6-4 for F_o = 0.25, T = 20ºC, and k_b = 16 kN/cm. It is observed that the peak relative

displacement of the deck does not change significantly for the different values of u_y. Since the smaller values of u_y imply shorter length of the SMA wires, it is preferred to choose a small u_y. However, note that the seismic demand on the piers increases with decreasing values of u_y. Specifically, there is an average increase of 39% in the peak base shear for the six excitation cases when u_y is changed from 50 mm to 20 mm. Also, since the stiffness of the SMA device increases when the length of the SMA wires used for the device shortens, the superstructure acceleration increases. In particular, when u_y is decreased from 50 mm to 20 mm, the deck acceleration amplifies by an average factor of 1.3 for all considered cases. It can be concluded from Figure 6-3 and Figure 6-4 that the SRB isolation system amplifies the peak deck acceleration and peak normalized base shear for large values of F_o and small values of u_y. Therefore, one should make a careful selection for these two parameters in order to mitigate the displacement response of the deck and at the same time limit the deck acceleration and base shear.

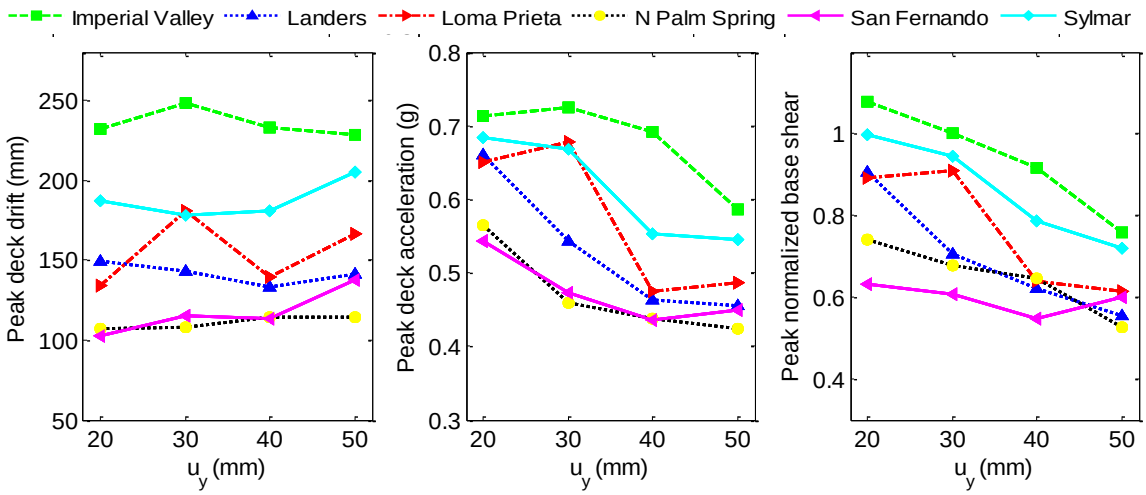

Figure 6-4 Variation of various peak response quantities with the forward transformation displacement of SMA device

6.4.3 Effect of Pre-Strain Level of the SMA Wires

The effect of pre-stressing force on the SMA wires that are used in the auxiliary SMA device of the isolation system is investigated by changing the initial pre-strain level of the SMA wires from 0 to 2.5%. Figure 6-5 presents the variation of the mean of the peak response quantities with the pre-strain level of the SMA wires for the isolated bridge subjected to different earthquakes. The simulations are conducted for three different values of F_o and u_y = 40 mm, T = 20ºC and u_y = 40 mm, and k_b = 16 kN/cm. It is observed that when the SMA wires are pre-stressed about 1% strain, the relative deck displacement decreases compared to the case without any pre-stressing force on the wires. Since the initial behavior of the superelastic SMA wires is almost linear elastic and they start to transform to martensite phase over 1% strain, a larger hysteresis loop, i.e. an increase in dissipated energy, is available when the wires are pre-stressed. This causes a reduction in the peak deck drift. However, when the pre-strain level is increased more than 1%, the corresponding decrease in deck drift is not significant for most of the cases. It is also observed that applying a pre-stressing force over 1% strain tends to increase the peak deck acceleration. Furthermore, the variations in the peak shear force transferred to the piers are small when the pre-strain level is increased from 1% to 2.5%. Overall, these observations imply that applying an initial tensile force to the SMA wires that corresponds to a strain of 1-1.5% increases the effectiveness of the SMA device in reducing the seismic response of the bridges isolated by the SRB isolation system.

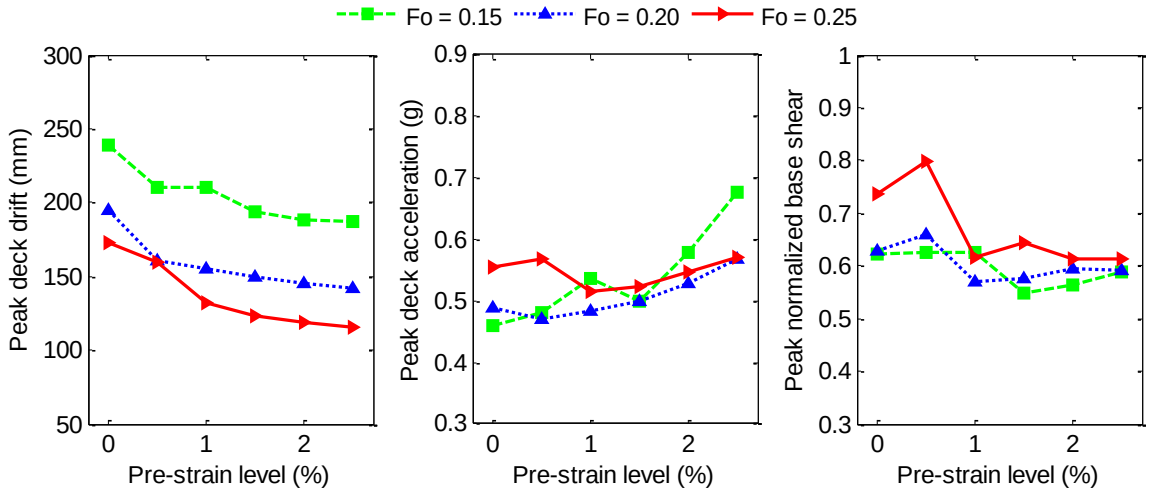

Figure 6-5 Variation of the mean of the peak response quantities with pre-strain level of SMA wires

6.4.4 Effect of Lateral Stiffness of the Laminated Rubber Bearings k_b

The effect of the rubber stiffness on the performance of the SRB isolation system is evaluated. Here, the values chosen for the lateral stiffness of the laminated rubber are k_b = 11, 16, 25, 32, 45, 101 kN/cm. These values of the rubber stiffness correspond to isolation periods of 3.0, 2.5, 2.0, 1.5, and 1.0 s for the bridge isolated by laminated rubber bearings. Figure 6-6 shows the variation of the mean of the response quantities as a function of k_b for the isolated bridge subjected to different earthquakes. The results are given for u_y = 40 mm, T = 20ºC and F_o = 0.10, 0.15 and 0.25. For different design values of F_o for the SMA component of the SRB isolation system, increasing the stiffness of the rubber bearing decreases the peak deck drift but augments the peak deck acceleration and base shear, which indicates a loss of potential advantages of seismic

isolation. Also, since very low values of k_b results in excessive isolator deformations, k_b = 16 or 25 kN/cm corresponding to isolation periods of 2.5 and 2.0, respectively, provides the best performance for the considered bridge structure.

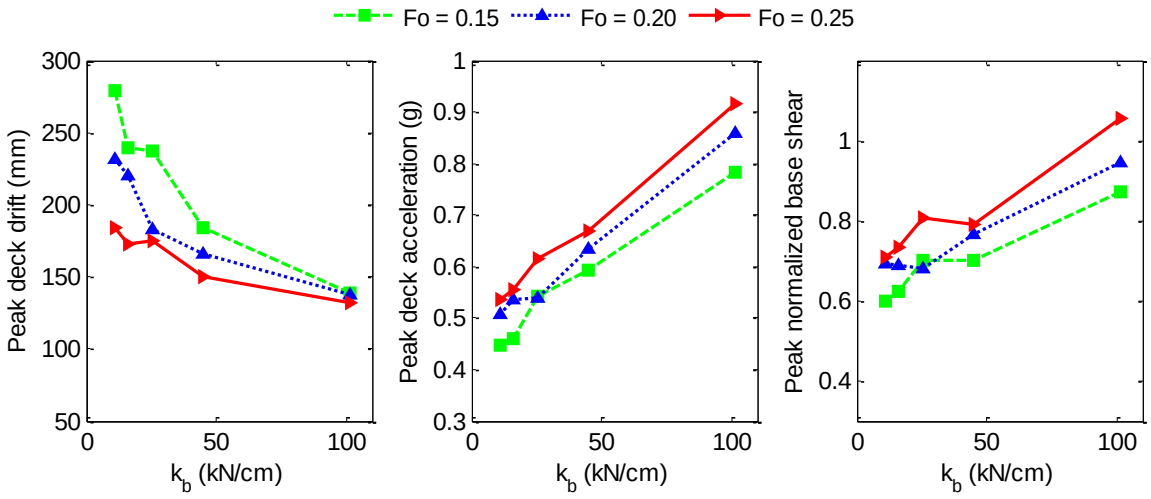

Figure 6-6 Variation of the mean of the peak response quantities with the stiffness of the rubber bearings

6.4.5 Effect of Ambient Temperature

In order to investigate the effect of temperature changes on the performance of the SMA/rubber-based isolation system, a set of time-history analyses is conducted for an environmental temperature range of 0-40ºC. The simulations are performed for F_o = 0.25, u_y = 40 mm, and k_b = 16 kN/cm. No pre-stress is present on the SMA wires. The results are demonstrated in Figure 6-7. It can be seen that there is a reduction in the peak deck drift with the increasing temperature for all excitation cases except the Imperial

Valley earthquake. This decrease can be attributed to the larger re-centering force of the SMA device at high temperatures. It is also observed that the maximum variation of the peak deck drift as the temperature increases 20°C compared to reference temperature of 20°C is only about 9%. However, there is an increase of 62% in the peak deck drift for the N Palm Springs earthquake when the temperature decreases 20°C compared to the reference temperature. Furthermore, the average variation of the peak deck drift for six excitation cases is only 6% when the temperature increases to 40°C, while it is 25% when the temperature decreases to 0°C. This implies deck response is more sensitive to a decrease than an increase in temperature. In addition, as a consequence of the larger SMA force at higher temperatures, the peak deck acceleration and peak normalized base shear increase with the increasing temperature. Specifically, the maximum variation of peak deck acceleration and normalized base shear is $\pm 27\%$ when temperature differs ± 20°C from the reference temperature of 20°C.

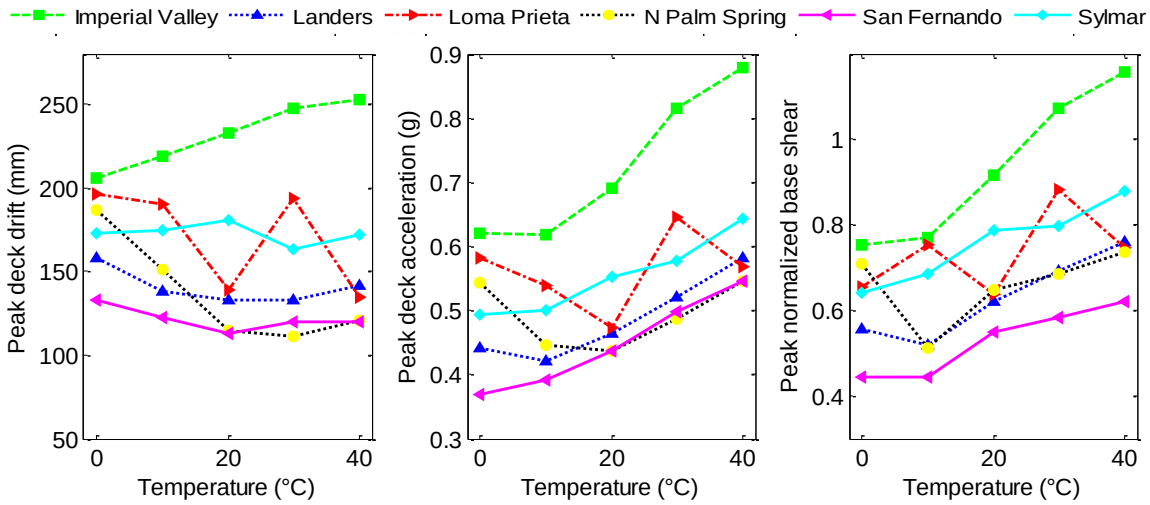

Figure 6-7 Variation of various peak response quantities with environmental temperature changes

6.5 Closure

As an alternative to conventional rubber isolators such as high damping rubber bearing and lead rubber bearing, smart rubber bearing systems with shape memory alloys have been proposed in recent years. As a class of smart materials, shape memory alloys show excellent re-centering and considerable damping capabilities which can be exploited to obtain an efficient seismic isolation system. This section investigates sensitivity of seismic response of a multi-span continuous bridge isolated by an SMA/rubber-based isolation system. The smart isolation system consists of a laminated-rubber bearing and an additional re-centering and energy dissipating device made of NiTi superelastic wires. A temperature- and –rate dependent model is used to characterize the behavior of the SMA device. Six historical ground motion records are

adjusted using the program RspMatch2005 to match a target design spectrum and employed as the external excitation in simulations.

The parameters for the sensitivity analysis are chosen to be the normalized forward transformation strength of the SMA device F_o, the forward transformation displacement of the SMA device u_y, the pre-strain level of the SMA wires, the lateral stiffness of the laminated rubber bearings k_b and environmental temperature changes. A large number of time-history analyses of the isolated bridge are performed to assess the effects of these parameters on the various response quantities of isolated bridges. In particular, the variation of peak deck drift, deck acceleration, and normalized base shear with analysis parameters are evaluated.

It is found that there is a trade-off between the displacement response of the deck and the deck acceleration, as well as the base shear for the increasing values of F_o. The optimum value of F_o is said to be in the vicinity of 0.25. It is also observed that the variation of u_y in the range of 20-50 mm does not significantly change the peak deck displacement response of the isolated bridge. Yet, since a lower value of u_y implies shorter wire lengths for a fixed 1% forward transformation strain, the stiffness of SMA device increases when u_y decreases and, as a consequence, the deck acceleration and normalized base shear increase about 30% and 39%, respectively.

The variation of the seismic response of the isolated bridge with environmental temperature is also evaluated. It is found that the effects of temperature change are more prominent in the case of a decrease in the temperature. Specifically, as temperature decreases 20°C compared to reference temperature of 20°C, peak deck drift experiences

an average of 25% increase with a maximum of 62%, and peak deck acceleration and normalized base shear vary to a maximum of 25% and 27%, respectively, for six excitation cases considered here. On the other hand, peak deck drift increases an average of 6% with a maximum of 9%, while there is a maximum increase of 27% in both peak deck acceleration and normalized base shear for all considered cases when temperature increases to 40°C from the reference temperature. Therefore, the effect of temperature change cannot be neglected during design of the isolation system since it affects the seismic response of the isolated bridge considerably. It is also observed that when the NiTi wires are pre-stressed so that they will have an initial strain in the range of 1-1.5%, the effectiveness of the SRB isolation system improves. The effect of rubber stiffness on the seismic response of the bridge is also analyzed. The results indicate that the SRB isolation systems can improve the performance of multi-span continuous bridges against seismic loadings by judicious selection of the parameters of SRB isolation system.

In the next section, the performance of the SMA/rubber-based isolation systems is compared with superelastic-friction base isolation system that combines a flat sliding bearing with an SMA device.

7. SEISMIC PERFORMANCE ASSESSMENT OF SMA-BASED ISOLATION SYSTEMS USING ENERGY METHODS

7.1 Introduction

In this section, the performance of the superelastic-friction base isolator (S-FBI) system discussed in Section 5 is compared with the SMA/rubber-based (SRB) isolation system introduced in Section 6. The S-FBI system combines superelastic shape memory alloys with a flat steel-Teflon bearing, whereas the SRB isolation system combines SMAs with a laminated rubber bearing rather than a sliding bearing.

Energy-based concepts have been considerably used in the earthquake resistant design of structures since an energy-based design method was introduced by Housner (1956) in the mid 1950s. The basic idea in the energy-based design is that the *energy demand* during a seismic excitation should be less than the *energy supply* of a structural system. In view of energy-based concepts, in seismic isolation, the goal is to reduce the seismic input energy to the system and dissipate the input energy through damping mechanisms. Therefore, an optimal isolation system should minimize the energy transmitted to the structure while dissipating the most of the energy through nonlinear hysteretic deformations in the isolation device with only a small amount of left energy that can cause damage on the main structural system (Austin and Lin, 2004).

In this section, first, the energy balance equations are formulated for non-isolated and isolated bridge structures. Both absolute and relative energy formulations are considered and the relevance of using them for the seismic evaluation of structures subjected to near-field earthquakes is discussed. Then, the effectiveness of the S-FBI

system and SRB isolation system for protecting bridges against near-field earthquakes are assessed by conducting nonlinear time history analyses. The optimum design values for both isolation systems are adopted from the work of the previous sections. For comparison purposes, the results for the bridge structure isolated by pure-friction (P-F) system and natural rubber bearing (NRB) system is also provided.

7.2 Seismic Input Energy Formulations for Non-Isolated Bridge

The three-span continuous bridge described earlier is also used in this section. The conventional non-isolated bridge is modeled as a single-degree-of-freedom system. The equation of motion is given as

$$m\ddot{u}_t + c\dot{u} + f(u) = 0, \tag{7-1}$$

where m is the total mass of the bridge, c is the damping coefficient, and $f(u)$ is the restoring force. For linear piers, the restoring force is given by $f(u) = ku$, where k is the stiffness of the piers. Also, u_t denotes the absolute displacement, u is the relative displacement and $\dot{u}$ is the relative velocity. Note that $u_t = u + u_g$, where u_g is the ground displacement and, the equation of the motion given above can also be written as

$$m\ddot{u} + c\dot{u} + f(u) = -m\ddot{u}_g \tag{7-2}$$

Integration of equations (7-1) and (7-2) with respect to relative displacement u over the entire duration of the seismic input leads to absolute and relative energy balance equations, respectively. Hence, the absolute energy formulation of a non-isolated bridge structure can be expressed as

$$\int_0^t m\ddot{u}_t \mathrm{d}u + \int_0^t c\dot{u}\mathrm{d}u + \int_0^t f(u)\mathrm{d}u = 0 \tag{7-3}$$

Replacing u by (u_t - u_g) in the first term of the equation (7-3) and rearranging the terms gives (Uang and Bertero, 1990)

$$\frac{m(\dot{u}_t)^2}{2} + \int_0^t c\dot{u}\mathrm{d}u + \int_0^t f(u)\mathrm{d}u = \int_0^t m\ddot{u}_t \mathrm{d}u_g \tag{7-4}$$

Equation (7-4) can be written in a general form as follows

$$E_K + E_\xi + E_A = E_I\,, \tag{7-5}$$

where

$$E_K = \frac{m(\dot{u}_t)^2}{2} \tag{7-6}$$

$$E_\xi = \int_0^t c\dot{u}\mathrm{d}u = \int_0^t c\dot{u}^2\mathrm{d}t \tag{7-7}$$

$$E_A = \int_0^t f(u)\mathrm{d}u \tag{7-8}$$

$$E_I = \int_0^t m\ddot{u}_t \mathrm{d}u_g = \int_0^t m\ddot{u}_t \dot{u}_g \mathrm{d}t \tag{7-9}$$

Here, E_K denotes the absolute kinetic energy, E_ξ is the damping energy, E_A is the absorbed energy, which is composed of the recoverable elastic strain energy E_S and the irrecoverable hysteretic energy E_H and, E_I represents the absolute input energy.

Similarly, integrating equation (7-2) with respect to u gives the relative energy equation as follows

$$\frac{m(\dot{u})^2}{2} + \int_0^t c\dot{u}\mathrm{d}u + \int_0^t f(u)\mathrm{d}u = -\int_0^t m\ddot{u}_g \mathrm{d}u\,, \tag{7-10}$$

and equation (7-10) can be expressed as

$$E_K^{'} + E_\xi + E_A = E_I^{'}, \tag{7-11}$$

where

$$E_K^{'} = \frac{m(\dot{u})^2}{2} \tag{7-12}$$

$$E_I^{'} = -\int_0^t m\ddot{u}_g \mathrm{d}u = -\int_0^t m\ddot{u}_g \dot{u} \mathrm{d}t \tag{7-13}$$

In equation (7-11), $E_K^{'}$ denotes the relative kinetic energy and $E_I^{'}$ is the relative input energy. Note that the definition of E_ξ and E_A is the same for both absolute and relative energy formulation.

In previous studies, in order to quantify the energy imparted to the structures, the absolute energy equation was used by some researchers (Park and Otsuka, 1999; Chapman, 1999; Takewaki, 2004), while the relative energy formulation (Fajfar and Vidic, 1994; Ordaz *et al.* 2003; Marano and Greco, 2003; Takewaki and Fujita, 2009) was employed by others. In a recent study, Kalkan and Kunnath (2008) investigated the relevance of using absolute and relative energy formulation in seismic evaluation of structures that are subjected to near-field ground motions. They found that the difference between absolute and relative energy input to structural systems during near-field earthquakes is much larger than that of in the case of far-field earthquakes. They suggested that selection of appropriate energy measure for near-field earthquakes should be based on the shape and period of the dominant pulse in the ground motion record and the vibration properties of the structural system. It was noted that arbitrarily using absolute or relative energy definitions for near-field ground motions can result in overlooking significant information.

In order to illustrate the difference in absolute and relative energy input to non-isolated bridge subjected to a typical far-field or near-field earthquake, Figure 7-1 and Figure 7-2 display the acceleration and velocity time history of a representative far-field (1940 El Centro record) and near-field ground motion (1990 Imperial Valley record), respectively as well as energy response history of the non-isolated bridge computed for selected records. It can be seen that the two different energy formulations result in similar input energy response histories for far field earthquake and input energy gradually builds up and reaches to a maximum near the end of the ground motion. In contrast, for near-field earthquakes, instantaneous energy spikes that have considerably larger values than the energy accumulated at the end are present in the response time history. The values of absolute and relative input energy differ significantly during these energy spikes.

Since the focus of this study is to evaluate the performance of SMA-based isolation systems during near-field earthquakes, both absolute and relative energy balance formulations are considered for the isolated bridge in the next section.

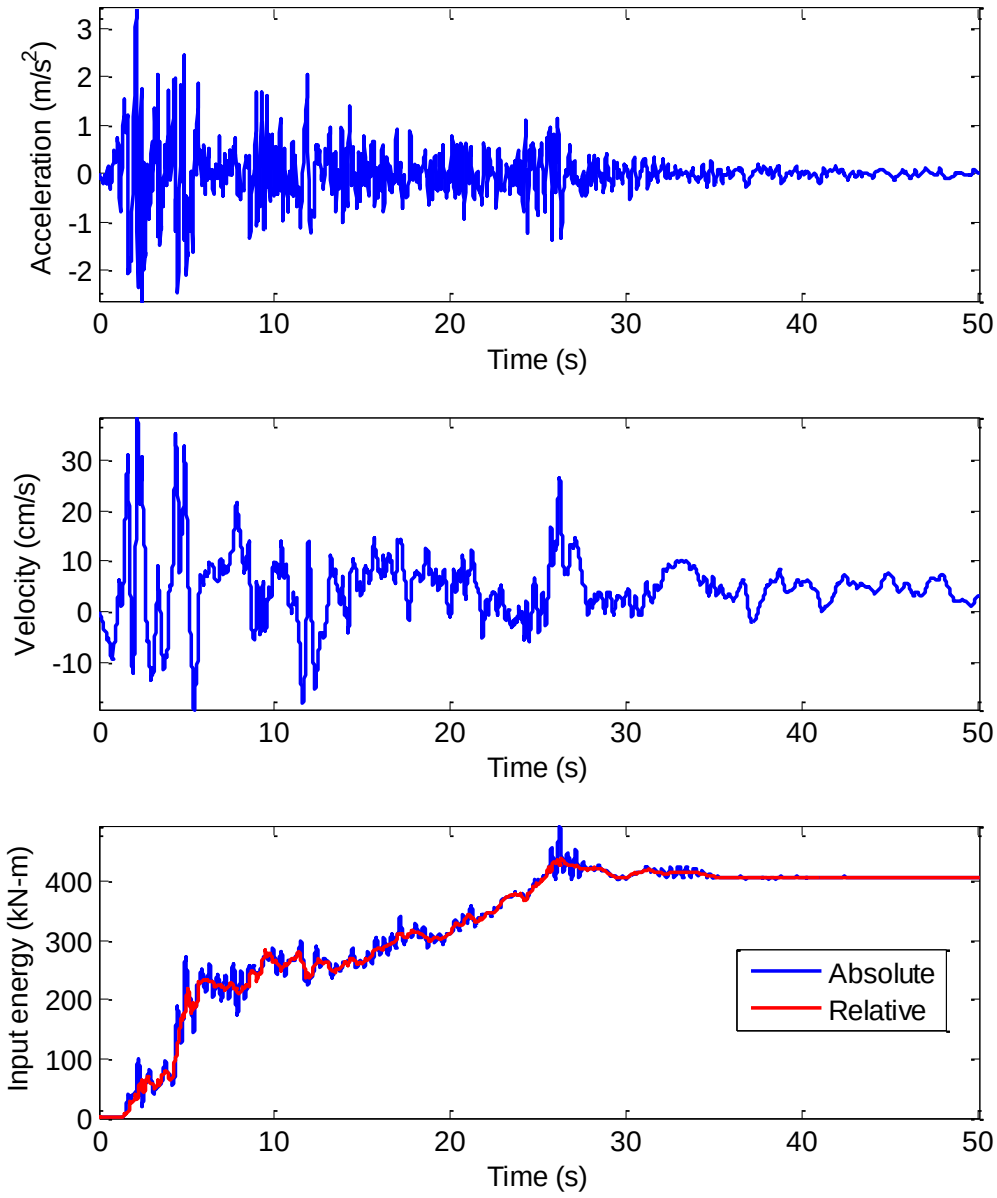

Figure 7-1 Acceleration, velocity and energy response time histories for a typical far-field earthquake

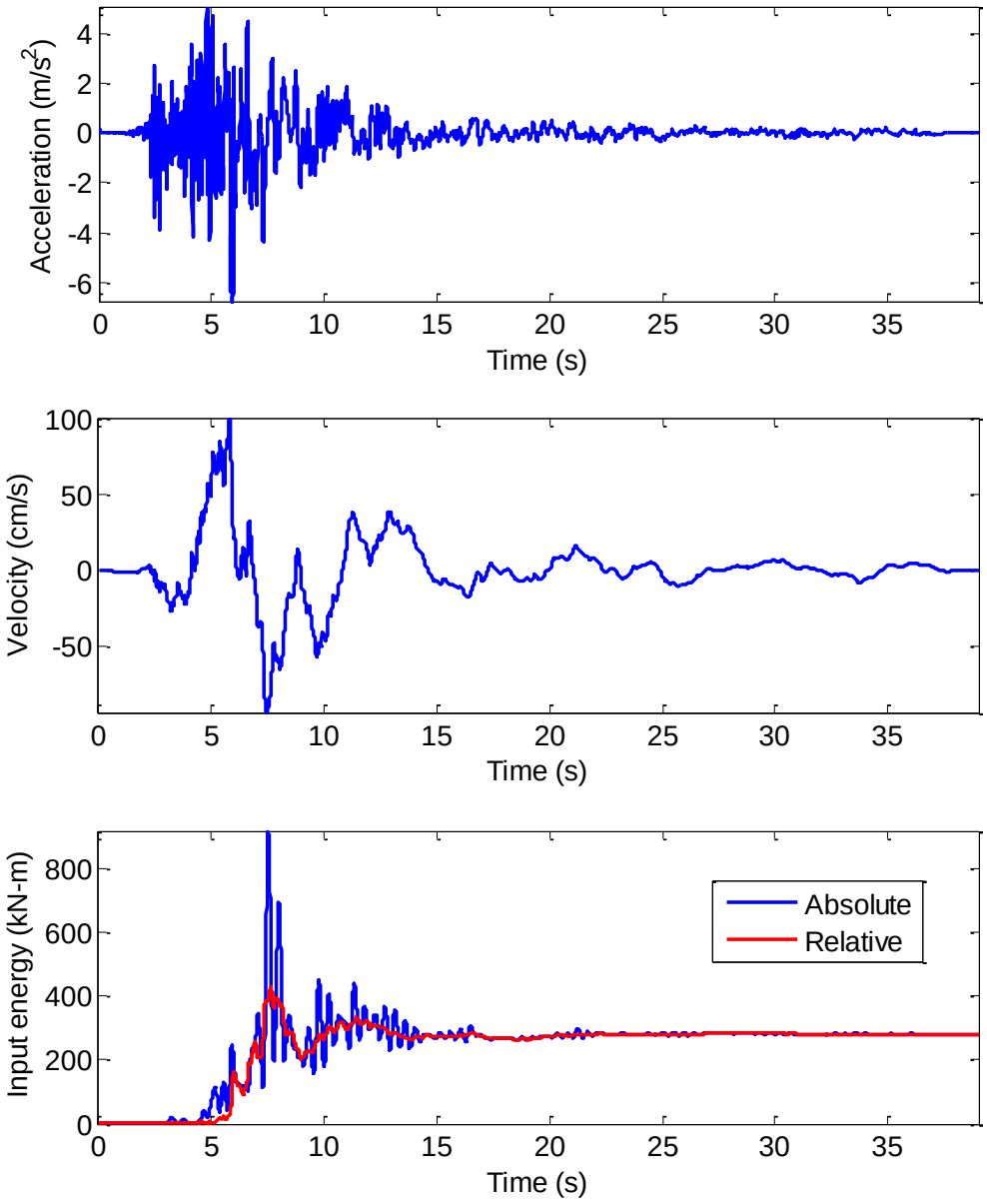

Figure 7-2 Acceleration, velocity and energy response time histories for a typical near-field earthquake

7.3 Seismic Input Energy Formulations for Isolated Bridge

The absolute energy balance equation of an isolated bridge modeled as two-degrees-of-freedom system can be written as

$$\frac{1}{2}\{\dot{u}_t\}^T\mathbf{M}\{\dot{u}_t\}+\int_0^t\{\dot{u}\}^T\mathbf{C}\mathrm{d}\{u\}+\int_0^t\mathbf{F}[u,\dot{u}]\mathrm{d}\{u\}=\int_0^t\{m\}^T\{\ddot{u}_t\}\mathrm{d}u_g(\tau) \tag{7-14}$$

where $\{u_t\}$ is the vector of absolute displacements of the system, $\{u\}$ is the vector of relative displacements of the system, **M** = (2×2) diagonal mass matrix, **C** = (2×2) damping matrix, and $\mathbf{F}[u,\dot{u}]$ = (2×1) vector of restoring forces, $\{m\}$ = (2×1) vector of lumped masses and u_g is the ground displacement. Equation (7-14) can be simply expressed as

$$E_K+E_\xi+E_A=E_I\,, \tag{7-15}$$

where

$$E_K=\frac{1}{2}\{\dot{u}_t\}^T\mathbf{M}\{\dot{u}_t\} \tag{7-16}$$

$$E_\xi=\int_0^t\{\dot{u}\}^T\mathbf{C}\mathrm{d}\{u\}=\int_0^t\{\dot{u}\}^T\mathbf{C}\{\dot{u}\}\mathrm{d}\tau \tag{7-17}$$

$$E_A=\int_0^t\mathbf{F}[u,\dot{u}]\mathrm{d}\{u\}=\int_0^t\{\dot{u}\}^T\mathbf{F}[u,\dot{u}]\mathrm{d}\tau \tag{7-18}$$

$$E_I=\int_0^t\{m\}^T\{\ddot{u}_t\}\mathrm{d}u_g(\tau)=\int_0^t\{m\}^T\{\ddot{u}_t\}\dot{u}_g\mathrm{d}\tau \tag{7-19}$$

Similiarly, the relative energy equation for the isolated bridge can be written as follows

$$\frac{1}{2}\{\dot{u}\}^T\mathbf{M}\{\dot{u}\}+\int_0^t\{\dot{u}\}^T\mathbf{C}\mathrm{d}\{u\}+\int_0^t\mathbf{F}[u,\dot{u}]\mathrm{d}\{u\}=-\int_0^t\ddot{u}_g\{m\}^T\mathrm{d}\{u\} \tag{7-20}$$

or

$$E_K^{'} + E_\xi + E_A = E_I^{'}, \tag{7-21}$$

where

$$E_K^{'} = \frac{1}{2}\{\dot{u}\}^T \mathbf{M}\{\dot{u}\} \tag{7-22}$$

$$E_I^{'} = -\int_0^t \ddot{u}_g \{m\}^T \mathrm{d}\{u\} = -\int_0^t \{m\}^T \{\dot{u}\}\ddot{u}_g \mathrm{d}\tau \tag{7-23}$$

The difference between absolute and relative energy formulations is essentially the difference in the kinetic energy terms and can be computed as

$$E_I - E_I^{'} = E_K - E_K^{'} = \frac{1}{2}\{\dot{u}_t\}^T \mathbf{M}\{\dot{u}_t\} - \frac{1}{2}\{\dot{u}\}^T \mathbf{M}\{\dot{u}\} \tag{7-24}$$

7.4 Numerical Study

In this numerical study, an energy-based methodology is used to compare the performances of the S-FBI system described in Section 5 and the SRB isolation system studied in Section 6 for protecting bridge structures against near-field earthquakes. Based on the findings of the previous section, an optimal SRB isolation system with the design parameters of u_y = 40 mm, F_o = 0.25, k_b = 25 kN/cm and a pre-strain level of 1.5%. The optimum design parameters for the S-FBI system are adopted from Section 5. For the S-FBI system, the flat sliding bearings has a friction coefficient of 0.10 and the parameters of the SMA device are u_y = 30 mm and F_o = 0.10. No pre-stress is applied on the SMA wires. Note that for the above design parameters, the volume of the SMA wires used in the S-FBI system is 71% less than the volume of the SMA material employed in the SRB isolation system.

The results from the simulations of the bridge structure isolated by the natural (laminated) rubber bearings (NRB) with a lateral stiffness of k_b = 25 kN/cm and 2% viscous damping, and pure-friction (P-F) bearings with friction coefficient of 0.10 are given to serve as a benchmark in the performance evaluation of the SMA-based isolation system.

7.5 Results

In this section, first, peak structural results are provided for the isolated bridge structure with various isolation systems. Then, the time histories of the various response quantities for the isolated bridges subjected to Imperial Valley earthquake are presented, followed by the results for the energy balance assessment.

7.5.1 Peak Structural Response

Plots illustrating the peak response quantities for different isolation systems subjected to the six different earthquakes are given in Figure 7-3 through Figure 7-5. The mean of the results for these excitations are also presented in the same plots. It is clear that both SMA-based isolation systems successfully reduce the deck drift for all excitation cases. As it can be seen from Figure 7-3, the results for peak deck drift for SRB isolation system and S-FBI system are very close for the individual earthquake cases and the mean of the results for all excitations are the same. However, the SRB isolation system produces higher peak deck accelerations and base shears than the S-FBI system. In particular, for the S-FBI system, the mean of the peak deck acceleration for the considered excitations is as low as 53% of that of the SRB isolation system and the

mean of the peak normalized base shear is 35% lower than that of the SRB isolation system.

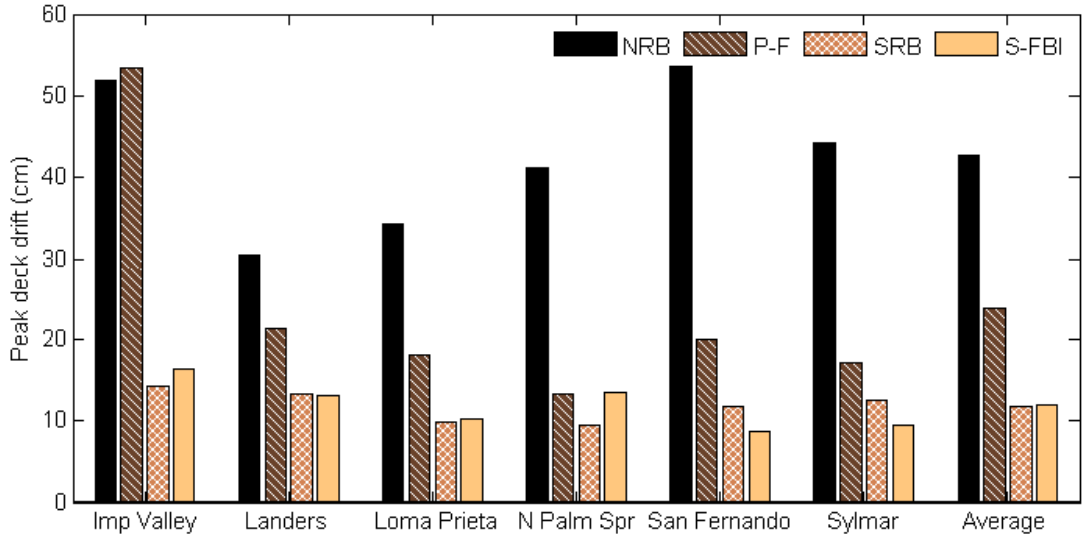

Figure 7-3 Peak deck drift for the various isolation systems subjected to near-field earthquakes

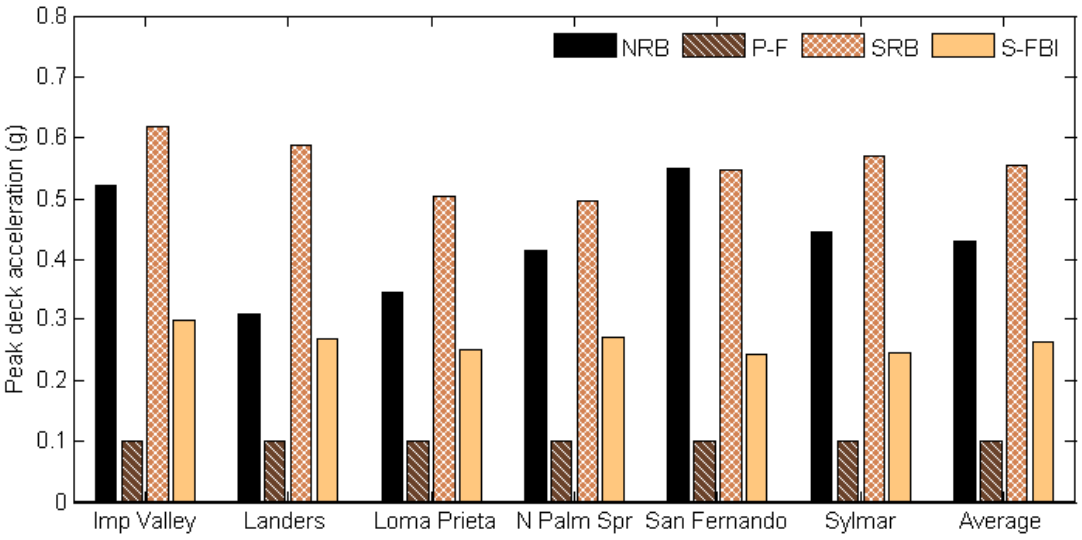

Figure 7-4 Peak deck acceleration for the various isolation systems subjected to near-field earthquakes

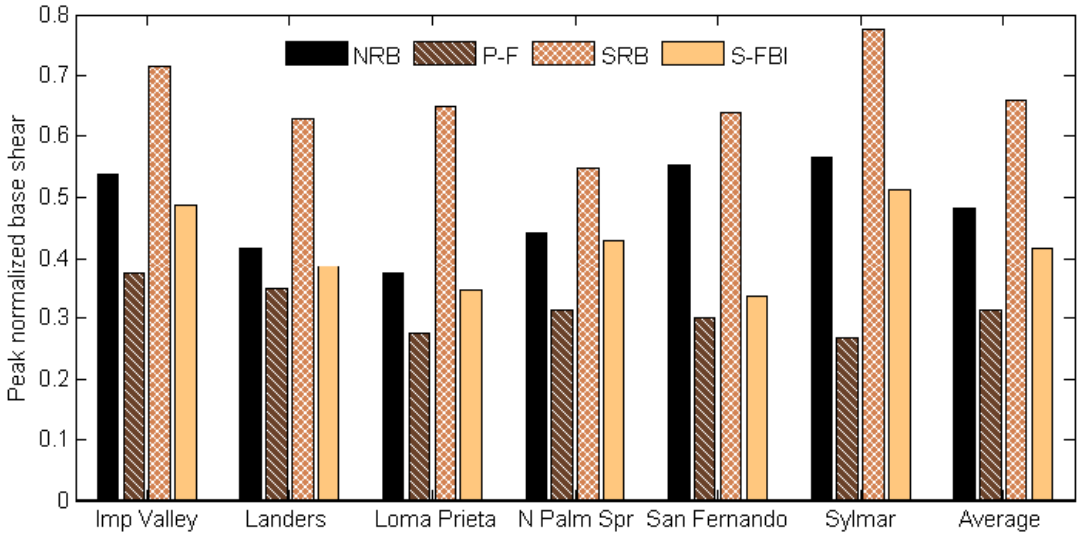

Figure 7-5 Peak normalized base shear for the various isolation systems subjected to near-field earthquakes

7.5.2 Time Histories of Structural Response

In order to further compare the performance of the two different SMA-based isolation systems, Figure 7-6 through Figure 7-8 displays the time histories of the deck drift, deck acceleration and normalized base shear for the Imperial Valley earthquake. The time history results for NRB and P-F isolation systems are also provided in the figures.

It can be seen from Figure 7-6 that the use of either the SRB isolation system or the S-FBI system significantly reduces the deck drift. Also, note that there is no residual displacement for both SMA-based isolation systems at the end of the motion. On the other hand, considerable residual deformations are present in the P-F system which lacks

re-centering force capability and the NRB system damp out the vibrations over much longer time.

It can be observed from Figure 7-7 and Figure 7-8 that the SRB isolation system produce higher deck acceleration and base shear response than the S-FBI system. However, the results for the SRB isolation system are still comparable to those of the NRB system. It should be also noted that the P-F system limits the maximum acceleration transmitted to the superstructure to a certain level that is a function of the friction coefficient. As compared to the P-F system, the S-FBI system to some extent increases the deck acceleration and base shear as a result of the increased stiffness due to the SMA device. However, it can be seen that the responses of the S-FBI system are comparable to those of the P-F system.

The increases in the deck acceleration response and pier base shear for the SRB isolation system as compared to the S-FBI system can be better explained by comparing the hysteretic forces generated in both isolation systems. Figure 7-9 illustrates the force-deformation curves of the SRB isolation system and the S-FBI system for Imperial Valley earthquake. It can be seen that the hysteretic force generated in the SRB isolation system is considerably larger than that of the S-FBI system. This higher isolator force that is transmitted to the piers from deck results in larger base shears for the SRB isolation system.

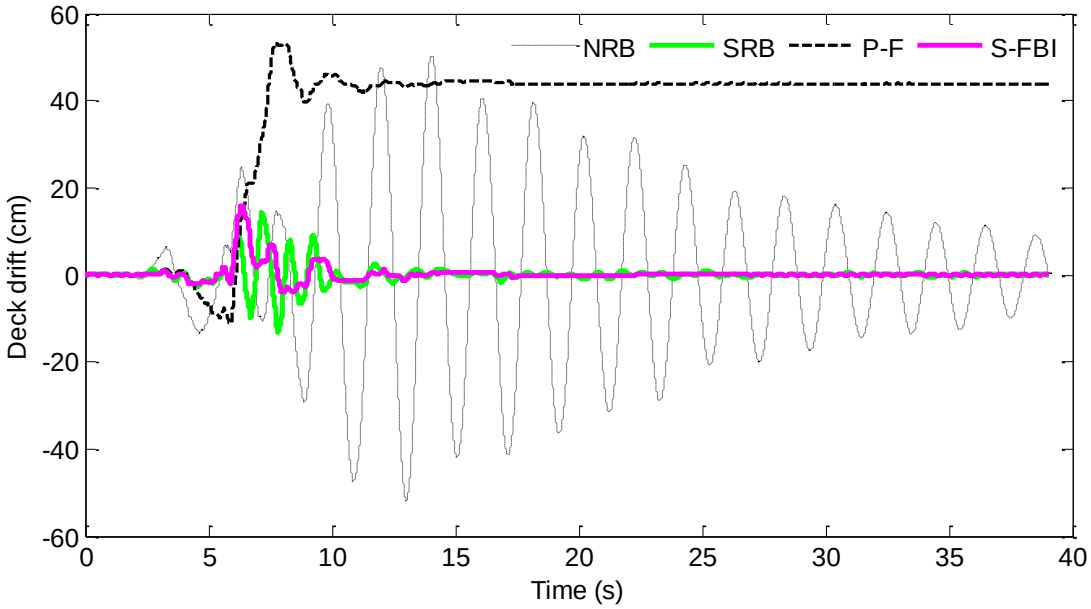

Figure 7-6 Time histories of deck drift of the isolated bridge subjected to Imperial Valley earthquake

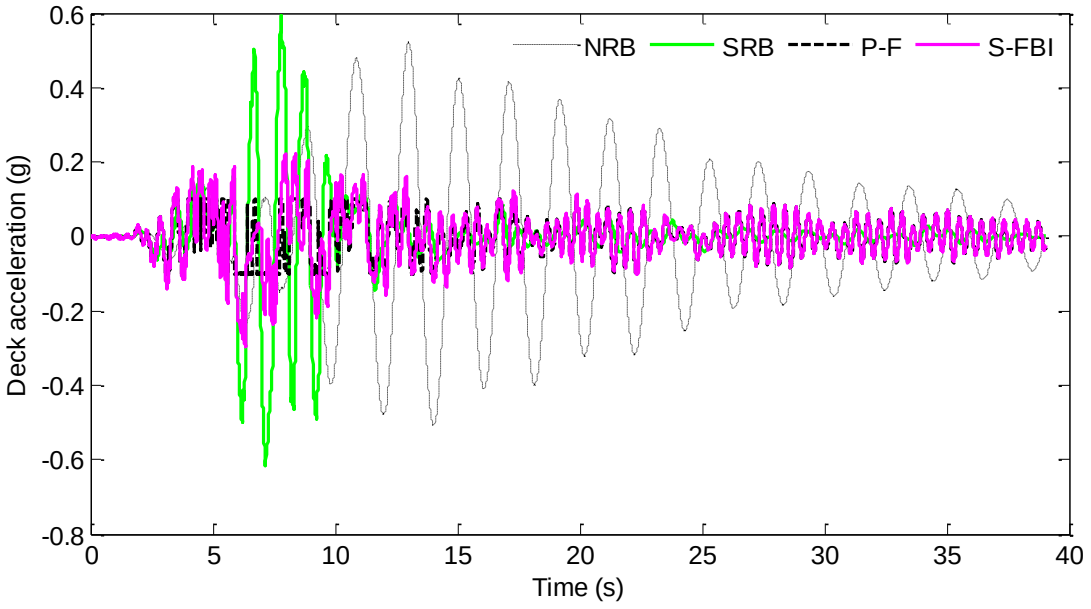

Figure 7-7 Time histories of deck acceleration of the isolated bridge subjected to Imperial Valley earthquake

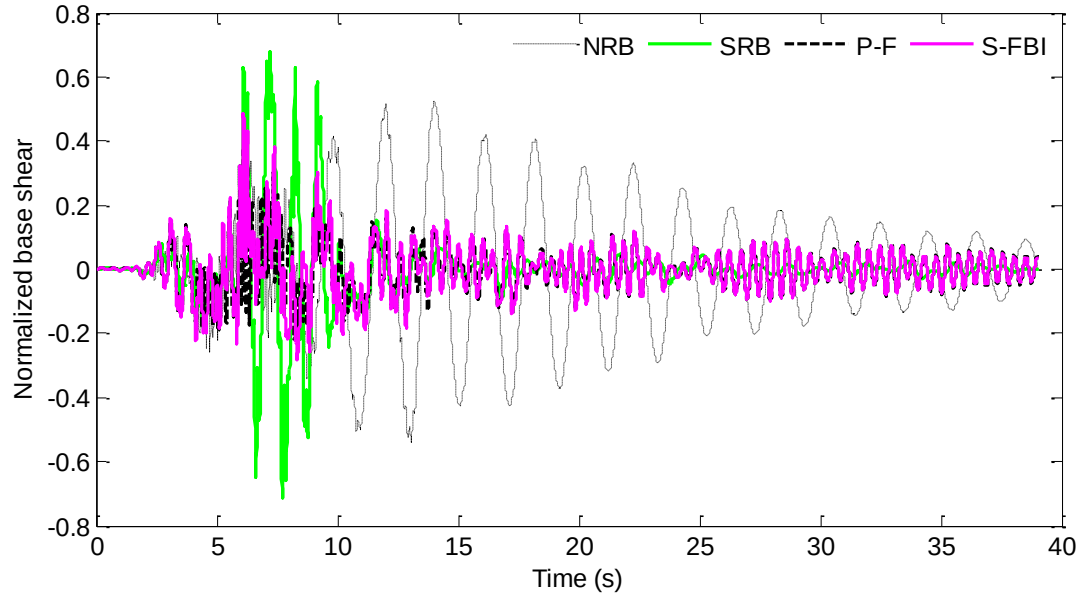

Figure 7-8 Time histories of normalized base shear of the isolated bridge subjected to Imperial Valley earthquake

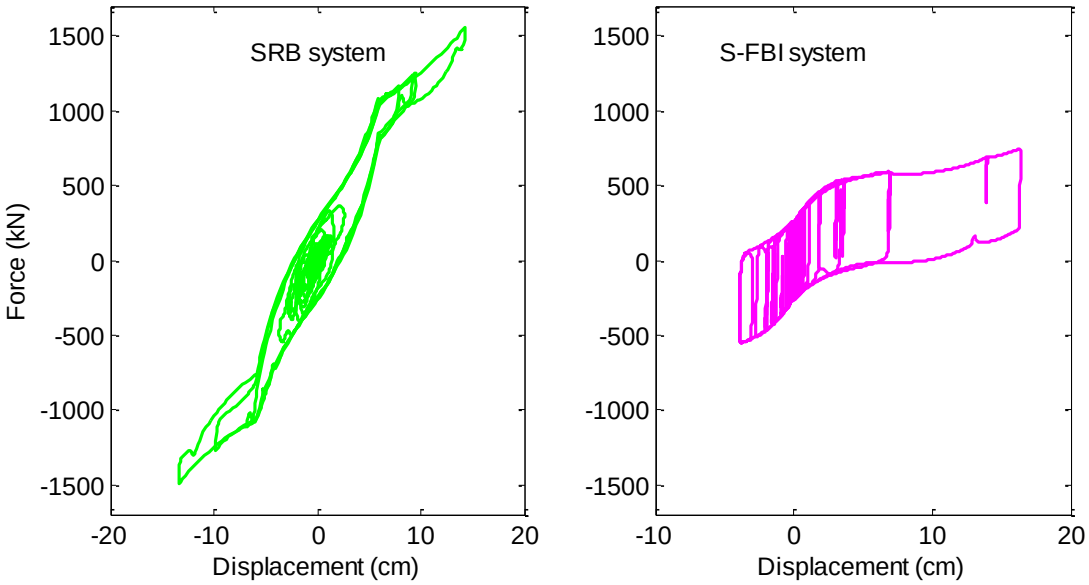

Figure 7-9 Force-deformation curves of the SRB isolation system and the S-FBI system subjected to Imperial Valley earthquake

7.5.3 Energy Response

Energy quantities are evaluated using all response quantities; hence, they can be good indicators for the evaluation of the performance of different isolation systems. Absolute and relative energy balance equations for non-isolated and isolated bridge structure are summarized below.

Absolute energy balance equation:

$$E_K + E_\xi + E_S + E_H = E_I, \tag{7-25}$$

Relative energy balance equation:

$$E_K^{'} + E_\xi + E_S + E_H = E_I^{'}, \tag{7-26}$$

where E_K and $E_K^{'}$ denote the absolute and relative kinetic energy, respectively; E_ξ is the damping energy; E_S is the recoverable elastic strain energy; E_H is the irrecoverable hysteretic energy; and E_I and $E_I^{'}$ represent the absolute and relative input energy, respectively.

Time-histories for each component of the absolute and relative energy balance equations are shown in Figure 7-10 and Figure 7-11 for the non-isolated bridge subjected to the Imperial Valley earthquake. Similar plots are provided in Figure 7-12 through Figure 7-19 for the bridge structure isolated by the NRB system, P-F system, SRB system and S-FBI system. In the figures, besides the time histories for E_K (or $E_K^{'}$), E_ξ, E_S, E_H (if applicable), and E_I (or $E_I^{'}$), the left-hand side (LHS) of the equation (7-25) (or equation (7-26)) is illustrated in order to check the computations by comparing it with the right-hand side of the equality, which is the E_I (or $E_I^{'}$). Also, in order to enable easy

comparison of the seismic input energy transmitted to the different systems, Figure 7-20 and Figure 7-21 displays respectively the absolute and relative input energy to the non-isolated bridge and isolated bridge with various isolation systems.

It can be seen that absolute input energy reaches a maximum value at the early stages of the excitation for non-isolated bridge and all the isolation systems except P-F system. On the other hand, the relative input energy cumulatively increases and reaches a maximum at the end of the motion for isolated bridges, whereas it has a small energy spike for the non-isolated bridge structure. It is clear that the input energy decreases when the bridge is isolated. This decrease is more noticeable for the P-F system and S-FBI system. However, the relative input energy for the NRB system is higher than that for the non-isolated bridge. It should be also noted that the S-FBI system has the minimum energy accumulation at the end of the motion for both absolute and relative energy formulations.

Figure 7-22 shows the time history of recoverable energy (kinetic energy + strain energy) transmitted to the bridge structure isolated by various isolation systems. It can be seen that there is a substantial reduction in recoverable energy, which is the cause of damage in the structure, for the P-F system and S-FBI system in comparison with that of the NRB system and SRB system. This is due to the fact that the force transmitted to the superstructure by the P-F or S-FBI system is considerable smaller than that by the NRB or SRB system. When the SMA-based isolation systems are compared, it can be noticed that the recoverable energy of the bridge structure isolated by S-FBI system is 60% smaller than that of the SRB system.

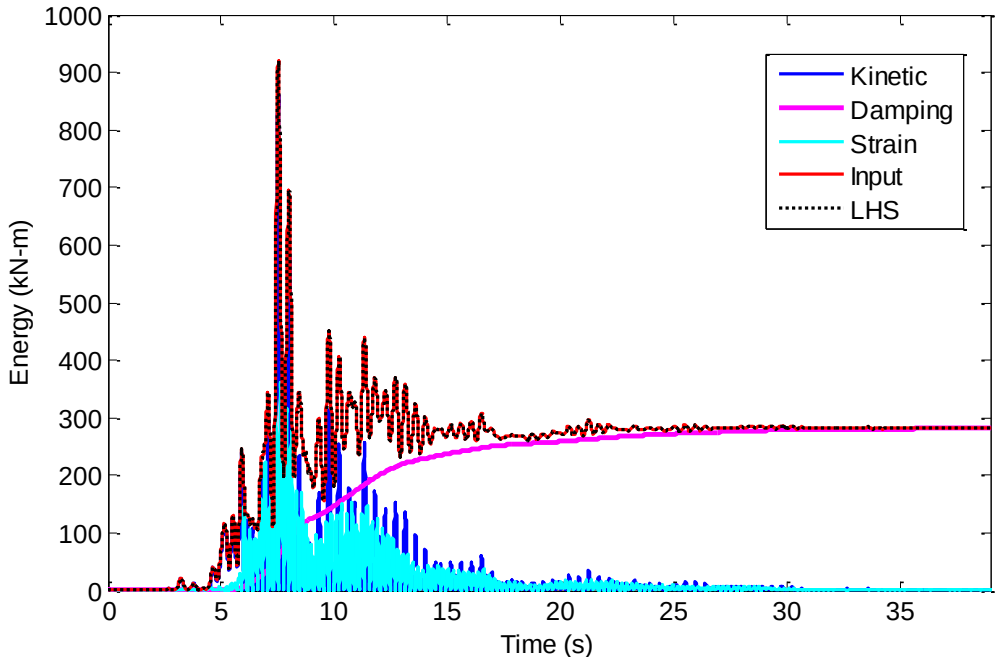

Figure 7-10 Energy time histories for the non-isolated bridge subjected to Imperial Valley earthquake for absolute energy formulation

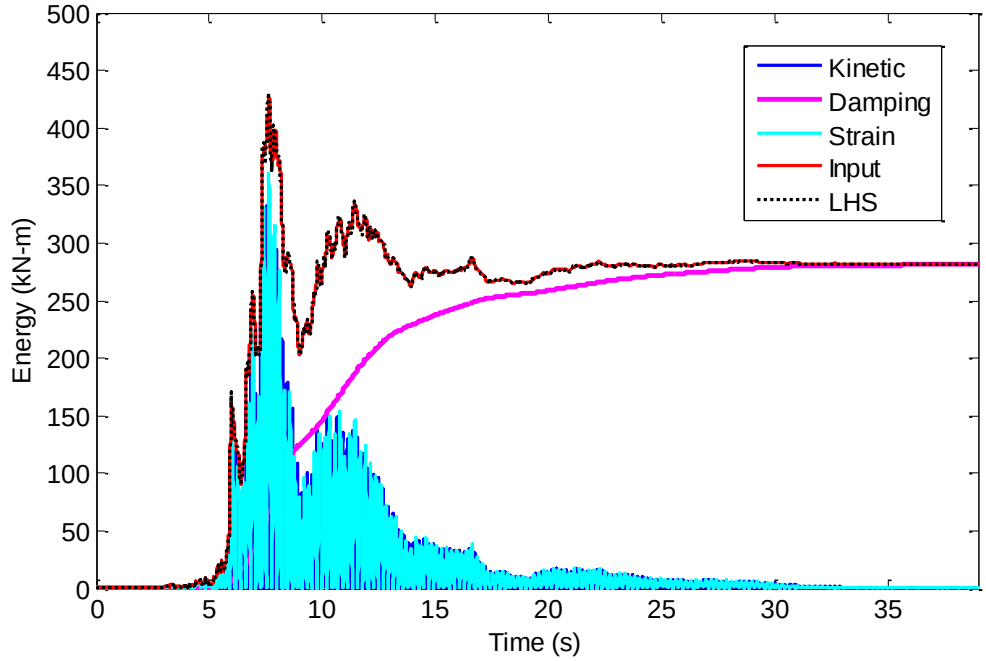

Figure 7-11 Energy time histories for the non-isolated bridge subjected to Imperial Valley earthquake for relative energy formulation

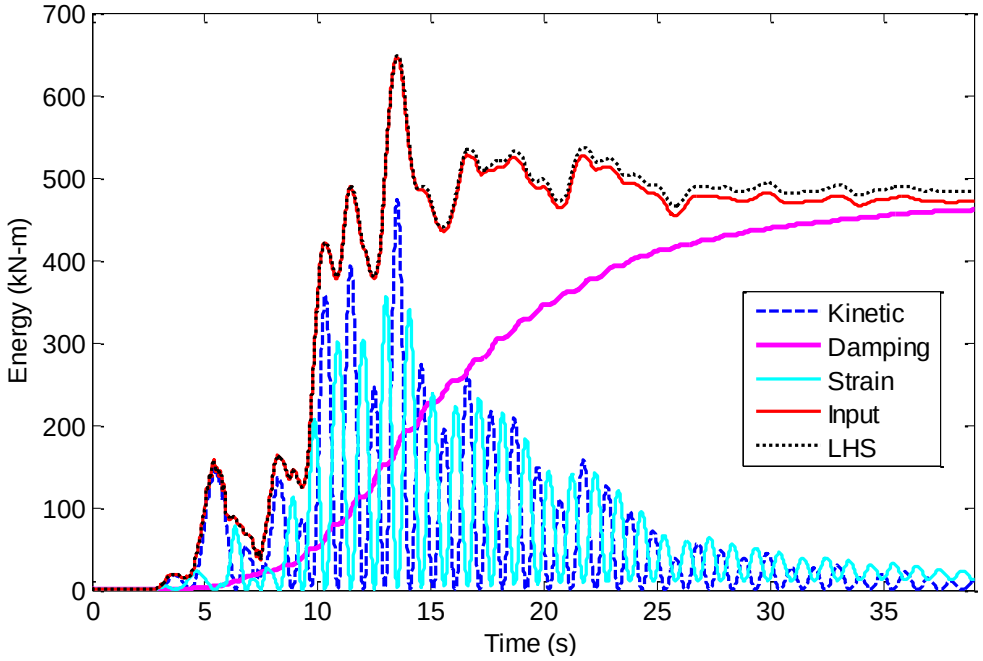

Figure 7-12 Energy time histories for the NRB system subjected to Imperial Valley earthquake for absolute energy formulation

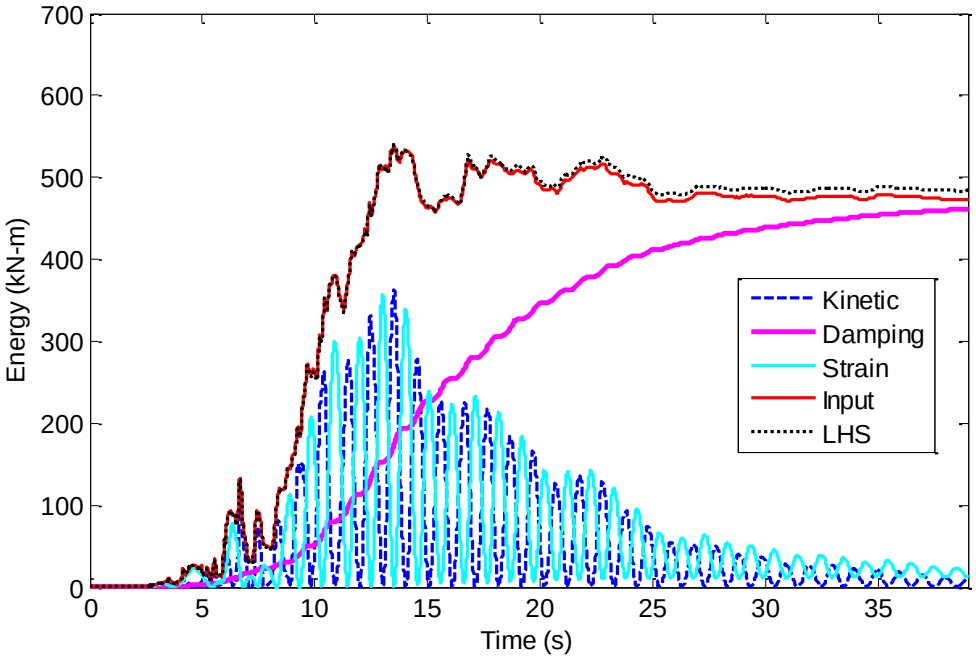

Figure 7-13 Energy time histories for the NRB system subjected to Imperial Valley earthquake for relative energy formulation

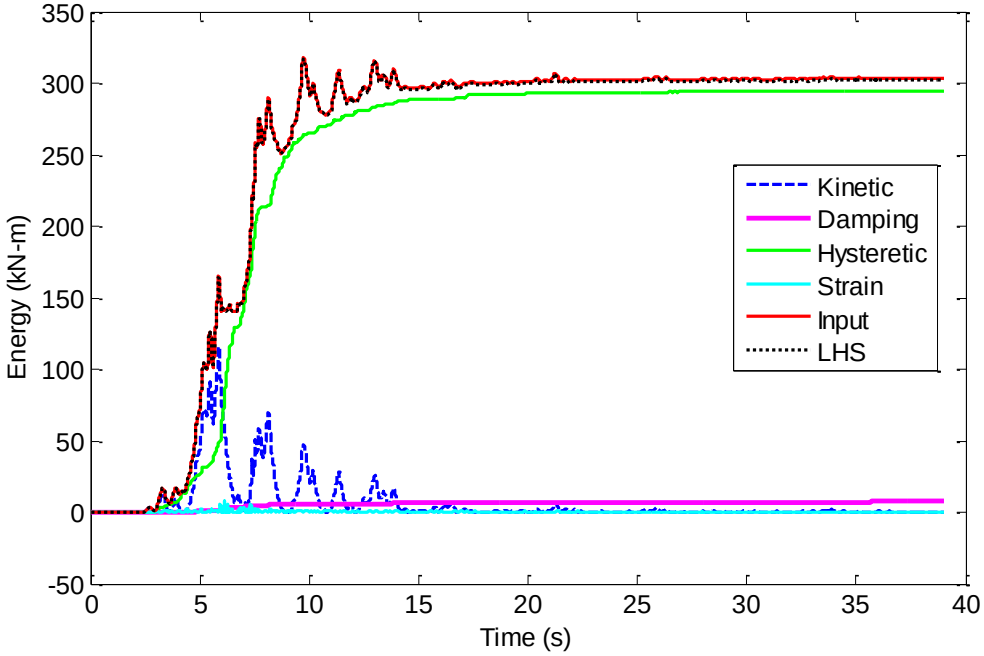

Figure 7-14 Energy time histories for the P-F system subjected to Imperial Valley earthquake for absolute energy formulation

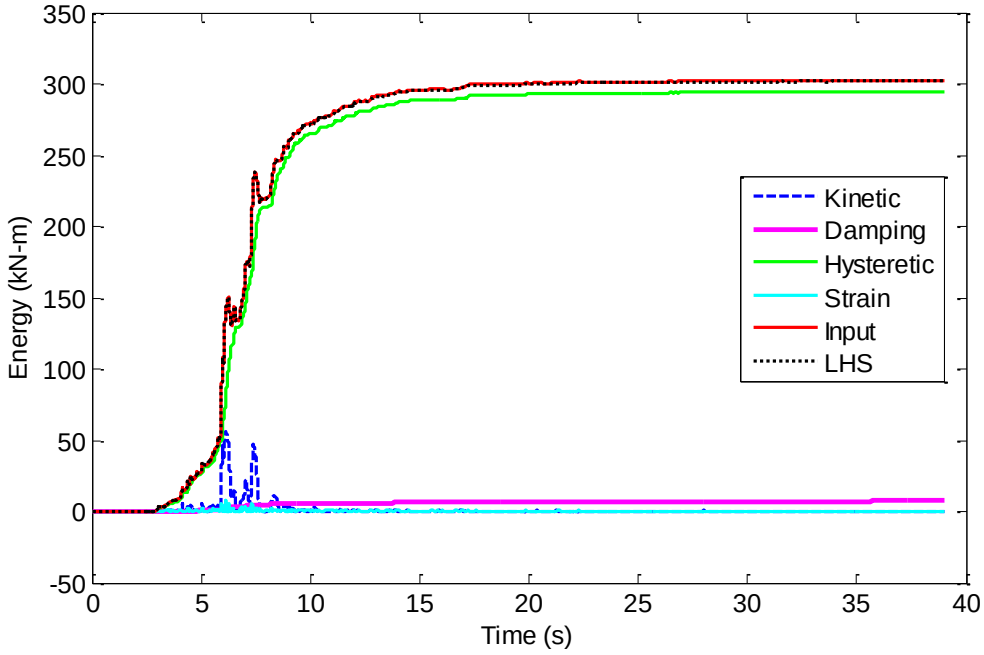

Figure 7-15 Energy time histories for the P-F system subjected to Imperial Valley earthquake for relative energy formulation

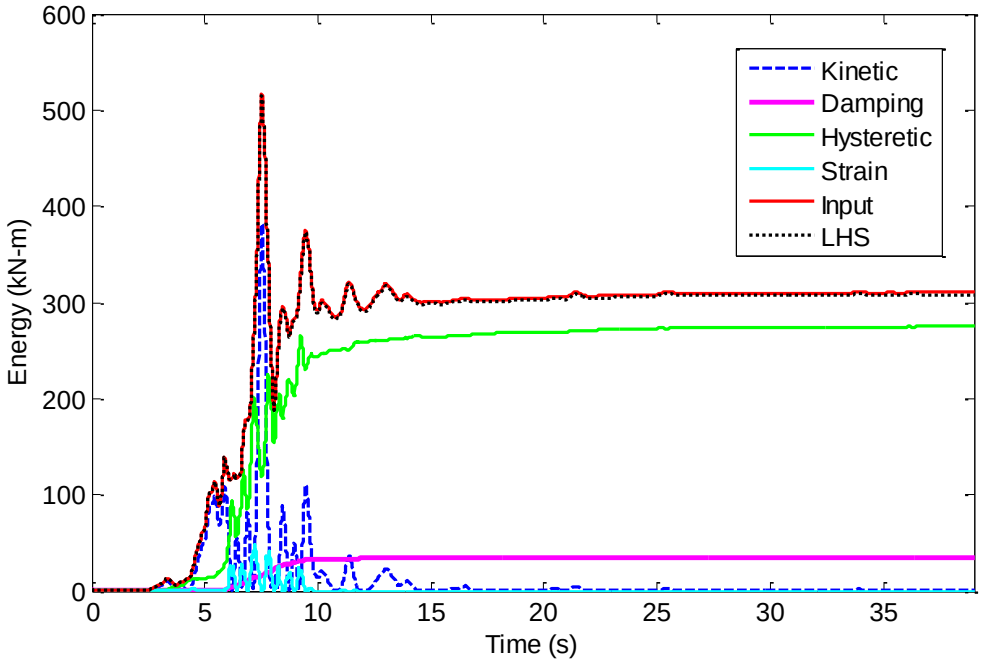

Figure 7-16 Energy time histories for the SRB system subjected to Imperial Valley earthquake for absolute energy formulation

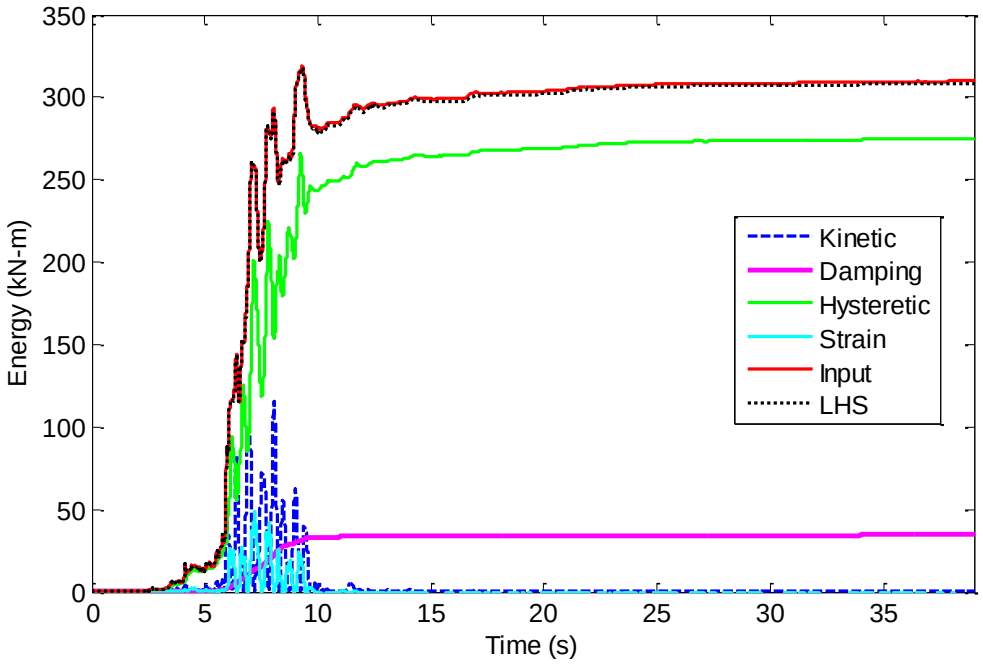

Figure 7-17 Energy time histories for the SRB system subjected to Imperial Valley earthquake for relative energy formulation

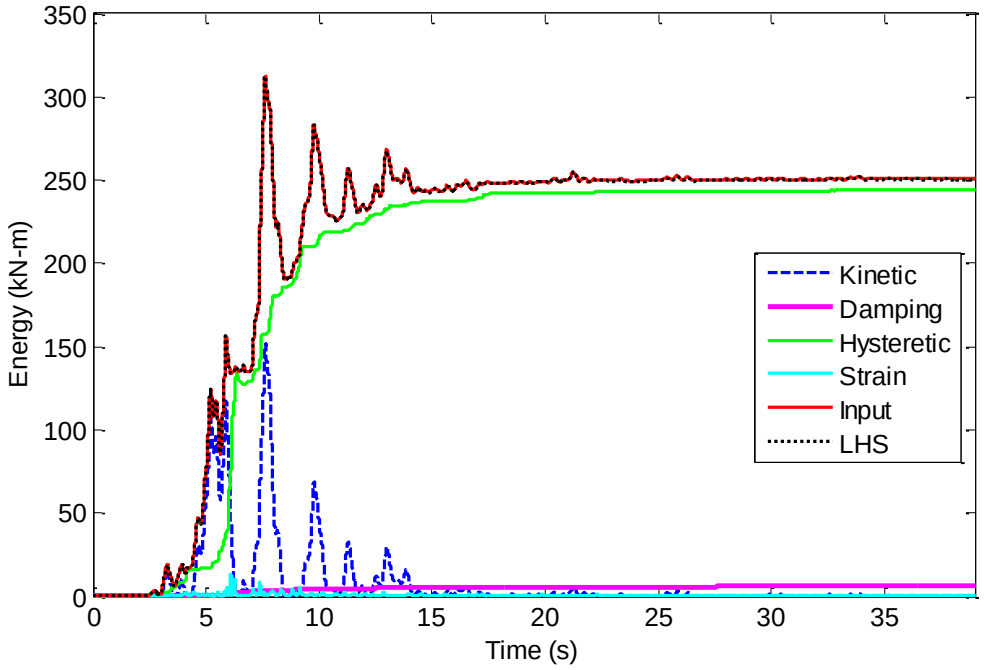

Figure 7-18 Energy time histories for the S-FBI system subjected to Imperial Valley earthquake for absolute energy formulation

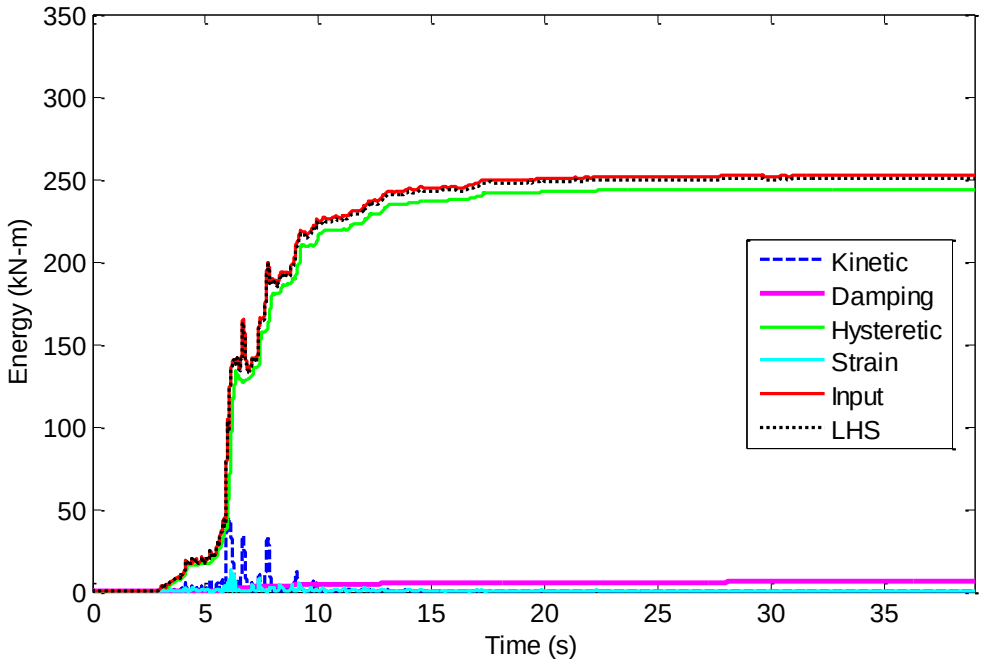

Figure 7-19 Energy time histories for the S-FBI system subjected to Imperial Valley earthquake for relative energy formulation

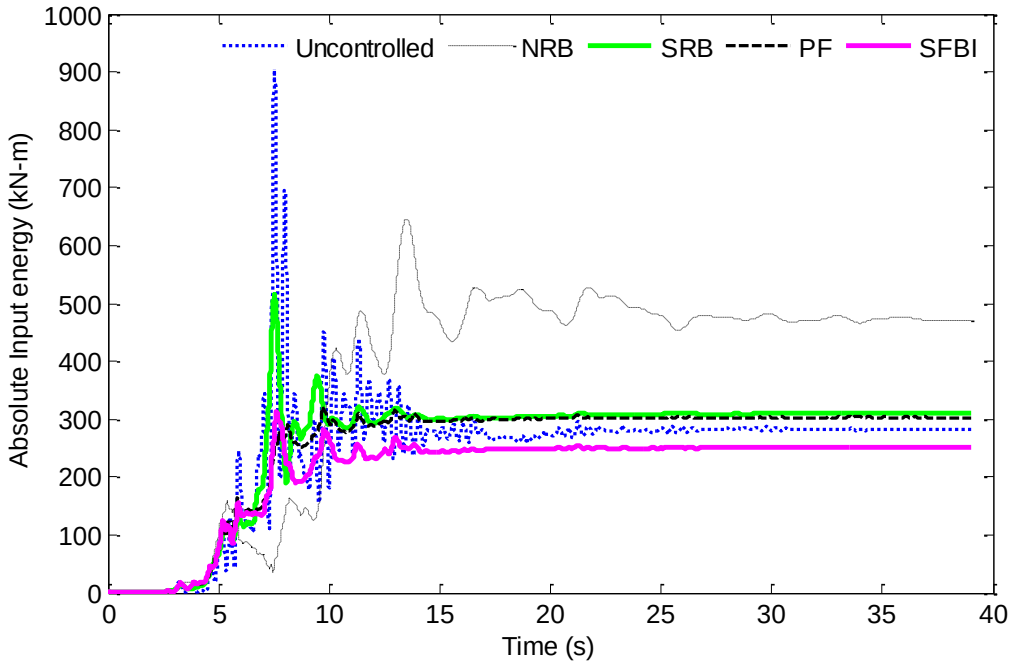

Figure 7-20 Time histories of absolute input energy for the non-isolated and isolated bridge structures subjected to Imperial Valley earthquake

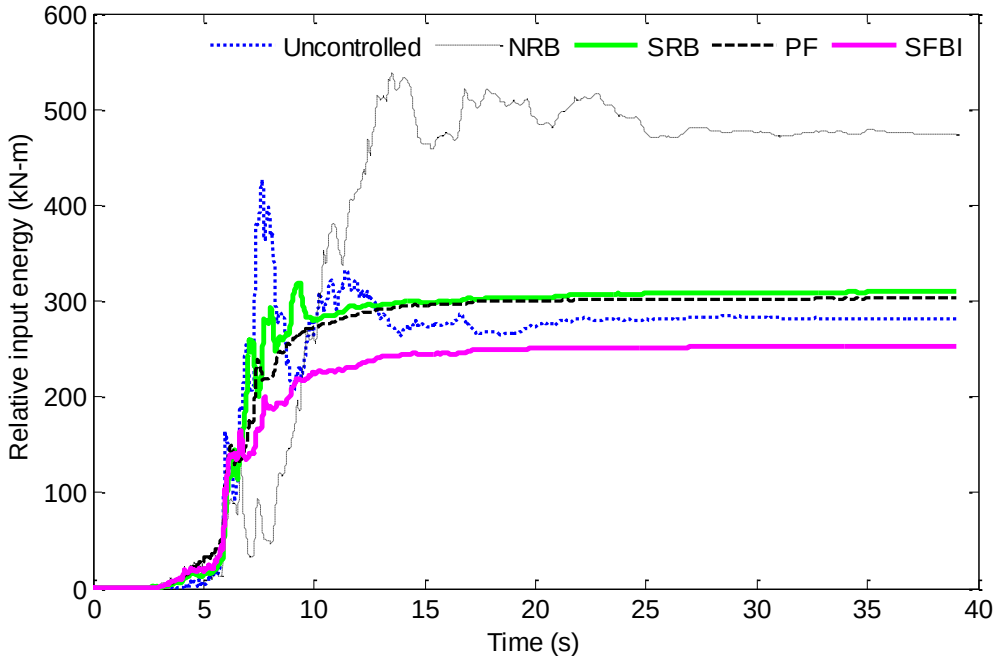

Figure 7-21 Time histories of relative input energy for the non-isolated and isolated bridge structures subjected to Imperial Valley earthquake

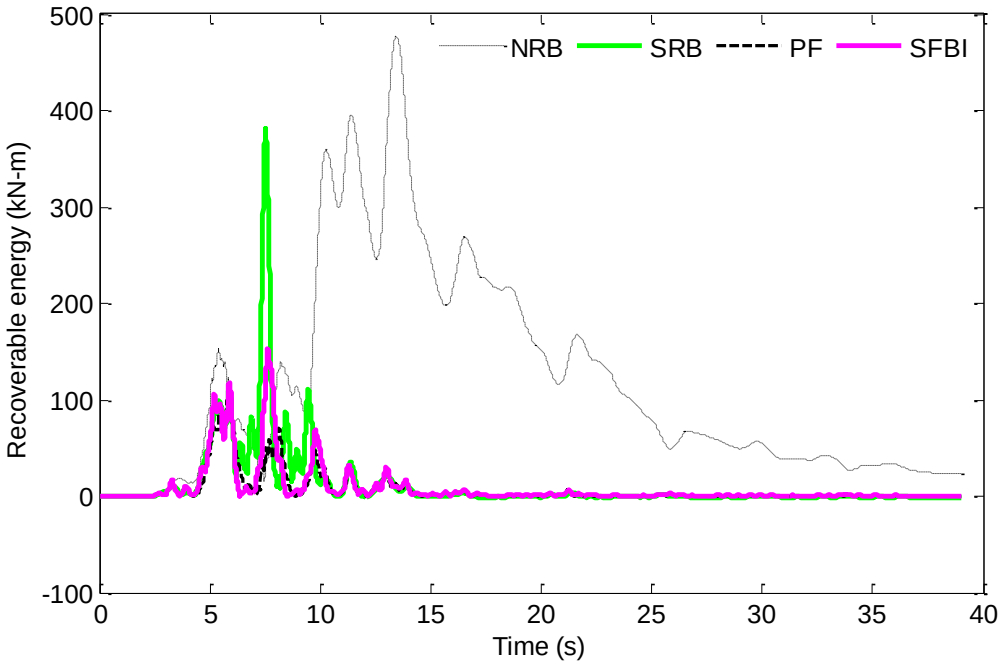

Figure 7-22 Time histories of recoverable energy for various isolation system subjected to Imperial Valley earthquake for absolute energy formulation

Time histories of the absolute and relative input energy and energy absorbed by the subcomponents of SMA-based isolation systems, i.e., the rubber and steel-Teflon bearings and the SMA device are plotted in Figure 7-23 through Figure 7-26 for the S-FBI system and the SRB isolation system subjected to Imperial Valley earthquake. It can be seen that the energy is dissipated mainly by the SMA device for the SRB isolation system whereas the SMA device serves as a re-centering component in the S-FBI system and the energy is dissipated through friction in the sliding surface for the S-FBI system.

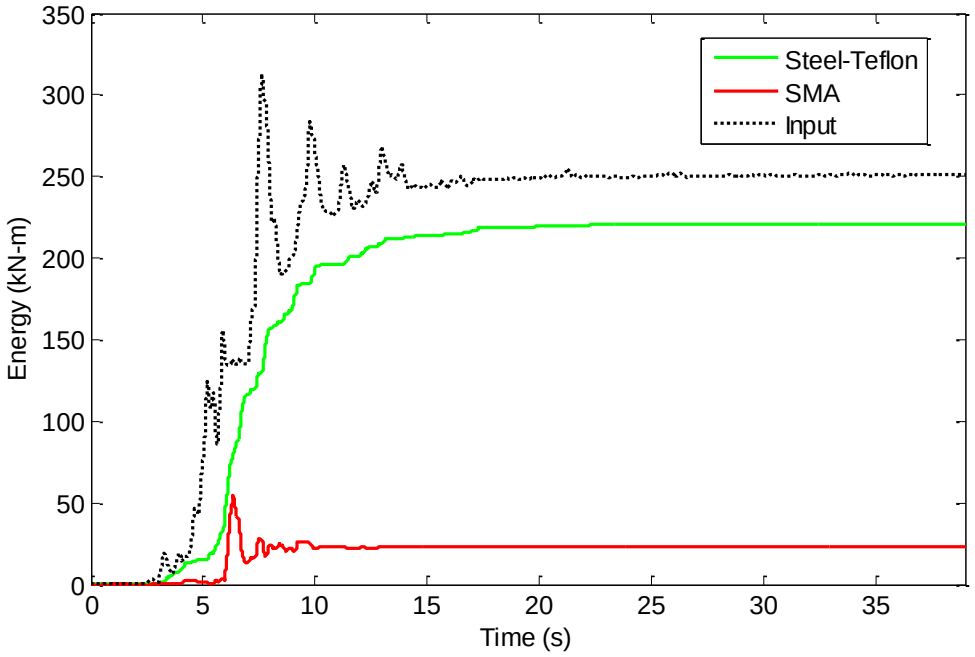

Figure 7-23 Time histories of the absolute input energy and subcomponents of the S-FBI system subjected to Imperial Valley earthquake

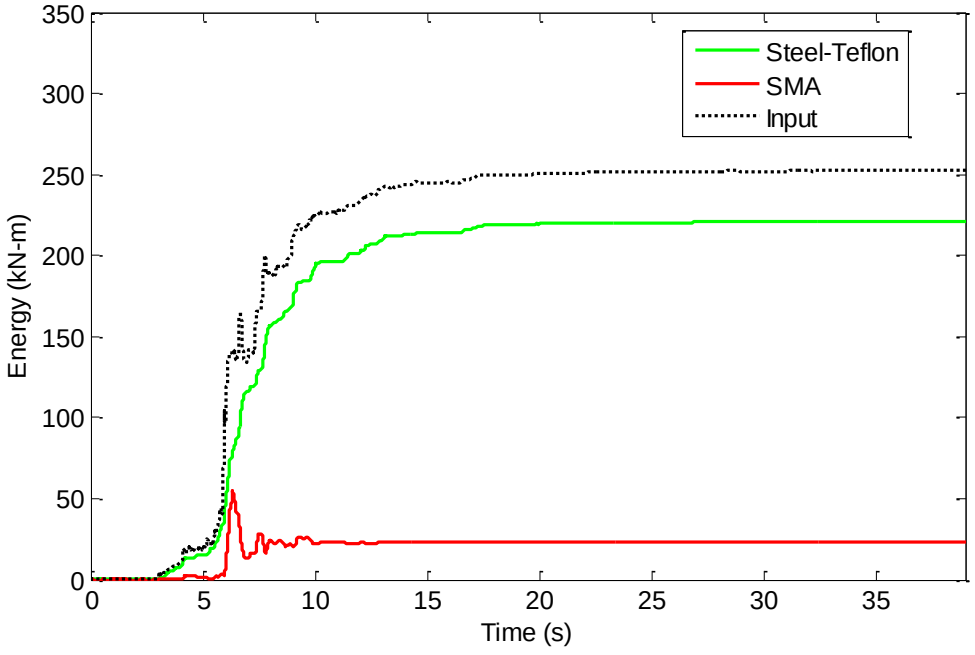

Figure 7-24 Time histories of the relative input energy and subcomponents of the S-FBI system subjected to Imperial Valley earthquake

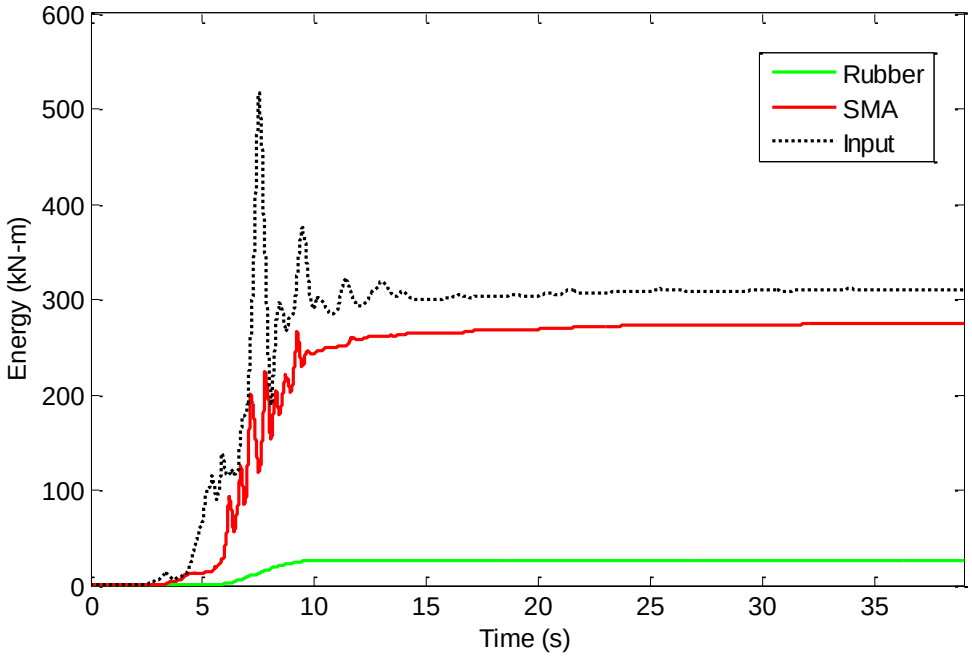

Figure 7-25 Time histories of the absolute input energy and subcomponents of the SRB isolation system subjected to Imperial Valley earthquake

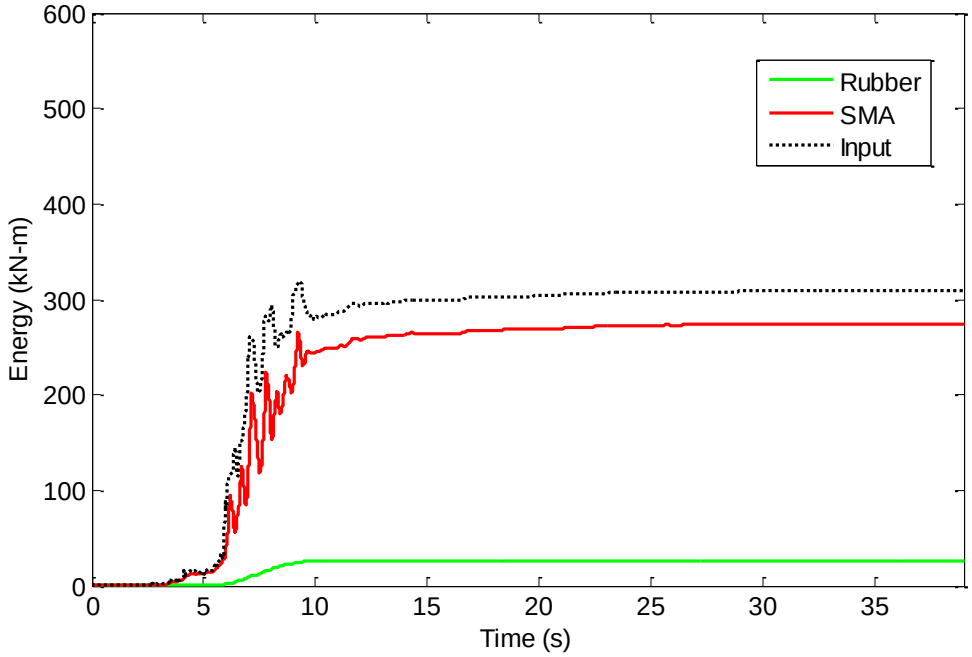

Figure 7-26 Time histories of the absolute input energy and subcomponents of the SRB isolation system subjected to Imperial Valley earthquake

7.6 Closure

In this section, the performances of two different SMA-based isolation systems, namely S-FBI system and SRB isolation system are evaluated by conducting nonlinear time history analyses with energy balance assessment. First, absolute and relative energy balance equations are derived for the non-isolated bridge and isolated bridge. Then, a numerical study is performed to compare the response of a three-span isolated bridge structure with an S-FBI system and that of an SRB isolation system. The results for isolated bridge with a typical pure friction system and a natural rubber bearing are also presented to serve as benchmark.

It is found that the bridge structure isolated by either the SRB isolation system or the S-FBI system has very similar results for the peak deck drift response for considered excitations. However, it is noted that the peak deck acceleration and peak base shear exhibits higher values in the case of the SRB isolation system.

It is also observed that the S-FBI system attracts smaller quantities of input energy than the S-RBI system. It is shown that the energy is mainly dissipated by the SMA components for the SRB isolation system. On the other hand, the energy dissipation in the S-FBI system is through friction, while the SMA component of the isolation system serves as a re-centering device. Since the energy dissipation in the SRB isolation system almost solely relies on the hysteretic behavior of SMAs, and, the energy dissipation capabilities of the superelastic SMAs are limited, larger amount of SMA material is required for the SRB isolation system. To be more specific, the S-FBI system

employs superelastic SMA wires that are 71% less in volume as compared to those used in the SRB isolation system.

Noting that the high cost of the SMA is mostly cited as one of the main barriers that preclude the use of SMAs in a full-scale seismic application and considering superior structural response of the S-FBI system, it can be concluded that the S-FBI system which combines SMAs with flat sliding bearings has more favorable properties than the SRB isolation system which consists of a laminated rubber bearing and an SMA device.

In the next section, the performance of the S-FBI systems on protecting bridge structures against near-field earthquakes is compared with that of traditional isolation systems used in practice.

8. A COMPARATIVE STUDY ON SEISMIC PERFORMANCE OF SUPERELASTIC-FRICTION BASE ISOLATORS

8.1 Introduction

In this section, a comparative study of the performances of various isolation systems such as lead rubber bearings (LRB), friction pendulum system (FPS), resilient-friction base isolators (R-FBI) and the superelastic-friction base isolators (S-FBI) for a multi-span continuous bridge under near-field ground motions is conducted (Ozbulut and Hurlebaus, 2010d). First, the modeling of a three-span continuous isolated bridge is discussed. Then, each seismic isolation system and its analytical model are briefly described. Next, nonlinear time-history analyses are carried out to compute the peak response quantities of the bridge with each seismic isolation system. The results for each isolation system are compared for various excitation cases. Finally, a parametric study for variations in isolation design parameters is conducted to evaluate the effect of these parameters on the effectiveness of the isolation system.

8.2 Model of Isolated Bridge Structure

A three-span continuous bridge studied also in Section 5 is selected for the comparative study. The isolated bridge is modeled as a two-degree-of-freedom system as described earlier.

In the sensitivity analysis, the response quantities of the isolated bridge are normalized with the correspondent value of the non-isolated bridge. Therefore, the conventional non-isolated bridge is modeled as a single-degree-of-freedom system as shown in Figure 8-1. The equation of motion is given as

$$m\ddot{u}(t) + c\dot{u}(t) + ku(t) = -m\ddot{u}_g(t), \tag{8-1}$$

where m is the total mass of the bridge ($m = m_p + m_d$), k is the stiffness of piers, and c is the damping coefficient of the non-isolated bridge. The critical damping in the piers for the non-isolated bridge $\xi_{p\,(ni)}$ is related to the isolated bridge characteristics ξ_p

The critical damping in the piers for the non-isolated bridge $\xi_{p\,(ni)}$ is related to the isolated bridge characteristics ξ_p

$$\xi_{p(ni)} = \xi_p \sqrt{\frac{1}{1 + m_d / m_p}}\,. \tag{8-2}$$

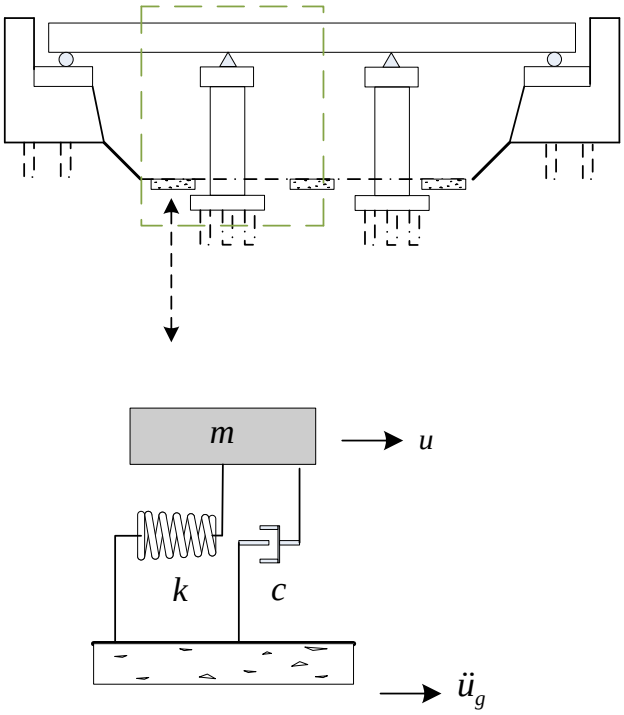

Figure 8-1 The analytical models of a non-isolated bridge

8.3 Modeling of Seismic Isolation Systems

8.3.1 Lead Rubber Bearings

A conventional elastomeric bearing consists of alternate layers of low damping rubber and steel bonded together and provides horizontal flexibility and sufficient vertical rigidity. A lead rubber bearing (LRB) is an elastomeric bearing with a lead-plug that provides hysteretic energy dissipation. The schematic diagram and bilinear force-deformation behavior of LRB are shown in Figure 8-2.

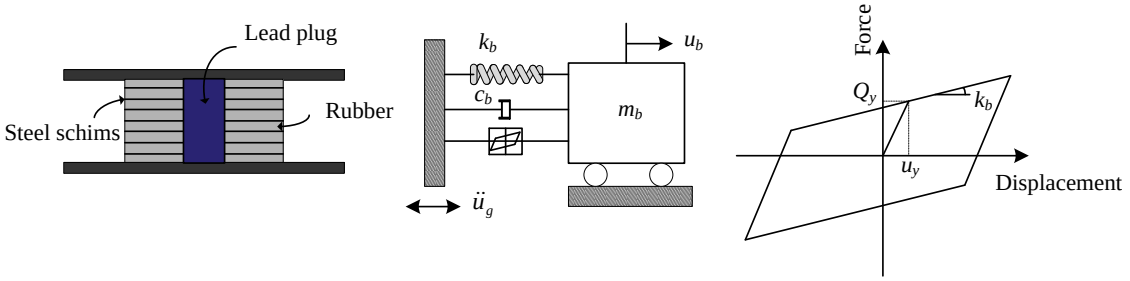

Figure 8-2 Lead rubber bearing with its schematic diagram and force-deformation curve

Here, the restoring force of the bearing is modeled using a Bouc-Wen model and given by

$$F_{LRB} = c_b\dot{u}_b + \alpha k_b u_b + (1-\alpha)F_y z, \tag{8-3}$$

where c_b and k_b are the viscous damping and initial stiffness of the bearing; $\dot{u}_b$ and u_b are the velocity and deformation of the bearing; α is the ratio of the post yielding to the elastic stiffness; F_y is the yield strength; and z is a hysteretic dimensionless quantity governed by the following differential equation

$$u_y\dot{z} + \gamma|\dot{u}_b||z|z|^{n-1} + \beta\dot{u}_b|z|^n - \dot{u}_b = 0 \tag{8-4}$$

where dimensionless parameters γ, β and n are taken as 0.5, 0.5, and 2, respectively, and the yield displacement of the LRB, u_y, is specified to be 2.5 cm. Also, the damping ratio of the LRB is taken to be 5% in the simulations. The design parameters considered here to characterize the LRB system are the fundamental isolation period T_b and the normalized yield strength F_o, which are defined as

$$T_b = 2\pi\sqrt{\frac{m_d}{\sum \alpha k_b}} \tag{8-5}$$

$$F_o = \frac{\sum F_y}{W_d}, \tag{8-6}$$

where W_d is the weight of the deck and $\sum \alpha k_b$ and $\sum F_y$ are the total yield stiffness and yield strength of the bearings.

8.3.2 Friction Pendulum Systems

The friction pendulum system (FPS) is a form of sliding bearing which consists of two curved steel plates that slide on each other because of an articulated slider. The concave geometry of the bearing enables a mechanism for restoring force, and the friction between slider and concave surface provides damping. The schematic diagram and force-deformation response of the FPS are shown in Figure 8-3.

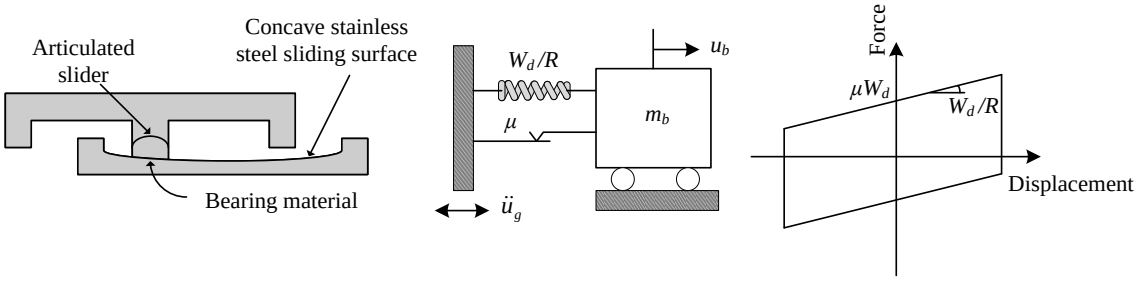

Figure 8-3 Friction pendulum system with its schematic diagram and force-deformation curve

The frictional force of the sliding systems is mainly described by either a conventional friction model or continuous hysteretic model in the past studies. In the conventional model, the frictional force of the sliding system is evaluated by solving different sets of equations for sliding and non-sliding phases, while the hysteretic model is a based on the principles of the theory of viscoplasticity and uses the Bouc-Wen

equations to model the frictional force. Jangid (2005a) found that both models predict the seismic response of sliding isolation systems similarly. Therefore, here, the continuous hysteretic model is used to define the frictional force in the FPS as follows

$$F_{FPS} = \mu W_d Z + \frac{W_d}{R} u_b, \tag{8-7}$$

where μ represents the coefficient of friction, R is the radius of the concave surface, and Z is a hysteretic dimensionless quantity computed from the equation (8-4). In the equation (8-4), the term u_y represents the yield displacement of the sliding bearing and chosen as 0.0005 m. Also, the dimensionless parameters γ, β, and n, have the values of 0.9, 0.1 and 1, respectively.

The design parameters of the FPS are the friction coefficient μ and the isolation period T_b which is expressed by

$$T_b = 2\pi\sqrt{\frac{R}{g}}, \tag{8-8}$$

where g is the acceleration due to gravity.

8.3.3 Resilient-Friction Base Isolators

Another method to provide restoring force to sliding isolation systems is to use the sliding bearing in combination with a central rubber core. The resilient-friction base isolator (R-FBI) combines the resiliency of the rubber and the friction of Teflon-coated steel plates in parallel. The schematic diagram and the force-deformation response of the R-FBI system are illustrated in Figure 8-4. The restoring force developed in the isolator is given by

$$F_{RFBI} = \mu W_d Z + c_b \dot{u}_b + k_b u_b, \tag{8-9}$$

where c_b and k_b are the viscous damping and initial stiffness of the bearing, respectively. The continuous hysteretic model described in the above section is used to model the friction force of the bearings. The viscous damping ratio of the rubber bearing is chosen to be 10%. The friction coefficient μ and the isolation period T_b are selected as two design parameters. The isolation period of the R-FBI system can be determined using the equation (8-5).

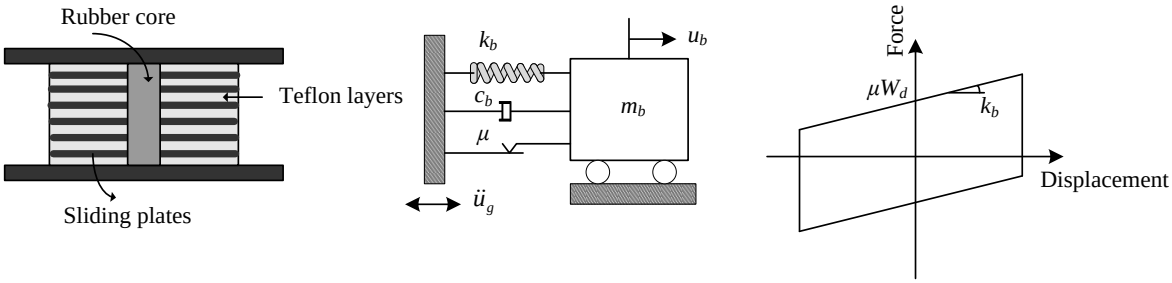

Figure 8-4 Resilient-friction base isolator with its schematic diagram and force-deformation curve

8.3.4 Superelastic-Friction Base Isolators

The superelastic-friction base isolator (S-FBI) consists of a flat steel-Teflon sliding bearing and a superelastic SMA device. The sliding bearings decouple the superstructure from the substructure and limit the transmission of the seismic force to a certain level according to the friction coefficient of the sliding surface. The SMA device mainly provides restoring force capability to the isolation system. It also offers additional energy dissipation through hysteresis of SMA elements even though the seismic energy is essentially dissipated via friction in the sliding surface of the bearings.

Here, the SMA device simply consists of multiple loops of superelastic NiTi wires wrapped around low-friction wheels. Figure 8-5 shows the schematic diagram of the S-FBI system and the force-displacement curve of the S-FBI system. The restoring force of the S-FBI system is given as

$$F_{SFBI} = \mu W_d Z + F_{SMA}, \tag{8-10}$$

where F_{SMA} denotes the nonlinear force of the SMA device. A neuro-fuzzy model developed by Ozbulut and Hurlebaus (2010a) is used to simulate the force-deformation behavior of NiTi wires. This model is capable of capturing rate- and temperature-dependent material response while it remains simple enough to carry out numerical simulations.

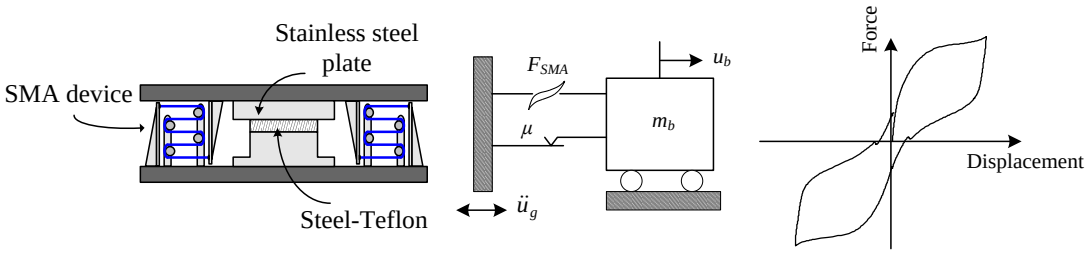

Figure 8-5 Superelastic-friction base isolator with its schematic diagram and force-deformation curve

The S-FBI system is characterized by the natural period of the isolated bridge T_b and the friction coefficient of sliding bearings μ. The natural period of the isolated bridge can be computed as

$$T_b = 2\pi \sqrt{\frac{m_d}{\sum \alpha k_{SMA}}}, \tag{8-11}$$

where αk_{SMA} denotes post forward transformation stiffness of the SMA device. Here, α which represents the ratio of post forward transformation stiffness and initial stiffness of the SMA device is taken as 0.1 and the forward transformation strain of SMA wires is chosen to be 1%, which are typical values for NiTi shape memory alloy wires. Also, the forward transformation displacement of the SMA device u_y is chosen to be 30 mm.

8.4 Ground Motions Used for Analyses

In the next section, the mean values of the peak response quantities are computed. Therefore, four more ground motions are added to the six historical earthquakes described earlier and the mean of the results is computed for a total of ten excitation cases. Table 8-1 gives the characteristics of the selected ground motions.

The selected records are adjusted using RspMatch2005 in order to simultaneously match 5%, 10% and 25%-damped response spectra as discussed in Section 5. The right subplot of Figure 8-6 shows the spectrally matched response spectra of all earthquakes for different damping levels. The use of the RspMatch2005 significantly reduces the spectral misfit for all damping levels.

Table 8-1 Description of the ground motions used in the analyses

Record No	Earthquake	Station	M_w	Distance (km)	PGA (g)	PGV (cm/s)
1	Imperial Valley, CA 1979/10/15	El Centro Array #6	6.5	1.0	0.44	109.8
2	N. Palm Springs, CA 1986/07/08	North Palm Springs 5070	6.0	8.2	0.59	73.3
3	San Fernando, CA 1971/02/09	Pacoima Dam 279	6.6	6.1	0.56	94.8
4	Landers, CA 1992/06/28	Lucerne 24	7.3	2.8	1.22	112.5
5	Loma Prieta, CA 1989/10/18	GPC 16	6.9	1.1	0.72	97.6
6	Northridge, CA 1994/01/17	Sylmar 74	6.7	6.2	0.90	102.8
7	Northridge, CA 1994/01/17	Rinaldi 77	6.7	7.1	0.85	50.7
8	Northridge, CA 1994/01/17	Tarzana, Cedar Hill 24436	6.7	17.5	1.05	75.4
9	Kobe, Japan 1995/01/16	Nishi-Akashi	6.9	11.3	0.51	37.3
10	Kocaeli, Turkey 1999/08/17	Sakarya	7.4	3.1	0.38	79.5

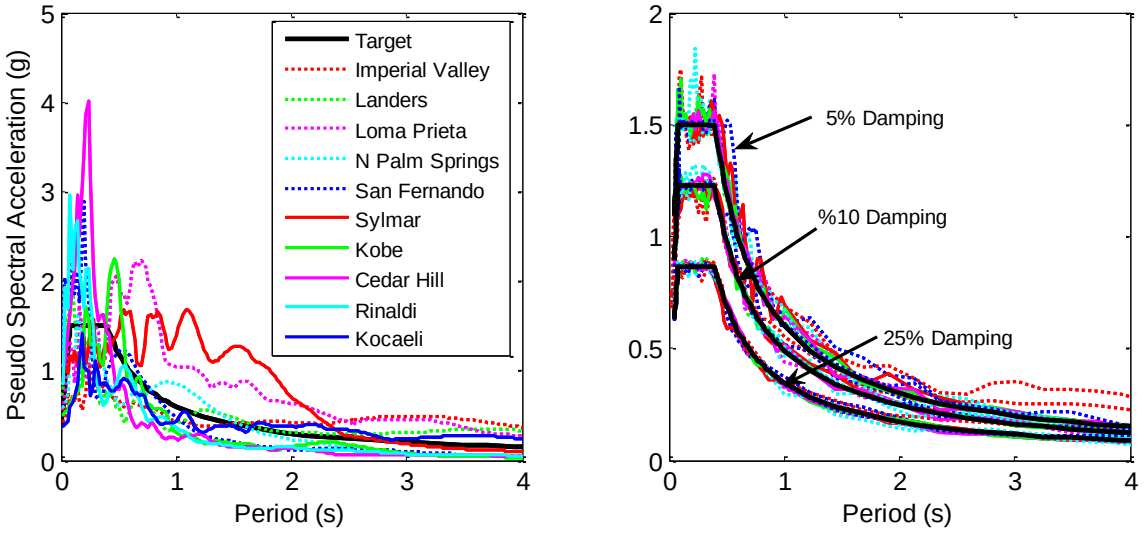

Figure 8-6 Target response spectrum compared to response spectra of selected ground motions and the spectrally matched response spectra of all earthquakes for different damping levels

8.5 Parametric Study

In this section, first, a comparative performance study is presented for the recommended values of parameters for different isolation systems. Then, a sensitivity analysis is performed to evaluate the variations of the response quantities with design parameters of each isolation system.

8.5.1 Comparative Performance Study

The seismic response of the isolated bridge against ten ground motions described above is computed by performing nonlinear time history analyses for various isolation systems. The design parameters for the isolation systems are selected as given in Table 8-2 based on the suggestions in previous studies in order to effectively isolate the

considered bridge structure (Jangid, 2007; Jangid, 2005b; Iemura *et al.*, 2007; Ozbulut and Hurlebaus, 2010b).

Table 8-2 Selected design parameters for various isolation systems

Isolation system	Isolation period T_b (s)	Damping coefficient ξ	Friction coefficient μ	Normalized yield strength F_o
LRB	3.0	0.05	-	0.15
FPS	3.0	-	0.10	-
R-FBI	4.0	0.10	0.10	-
S-FBI	4.0	-	0.10	-

Figure 8-7 shows the peak deck drift of the isolated bridge for various isolation systems subjected to different ground motions. It can be seen that the S-FBI system constantly has the smallest peak deck drift for all excitation cases. Among the other three isolation systems, the peak deck drift attains its minimum value at a certain isolation system for a given earthquake. For example, the LRB system produces the smallest value for peak deck drift when the isolated bridge is subjected to the Imperial Valley (record #1) earthquake. However, for the San Fernando (record #3) and Loma Prieta (record #5) earthquakes, the FPS and the R-FBI systems, respectively outperform the other two isolation systems.

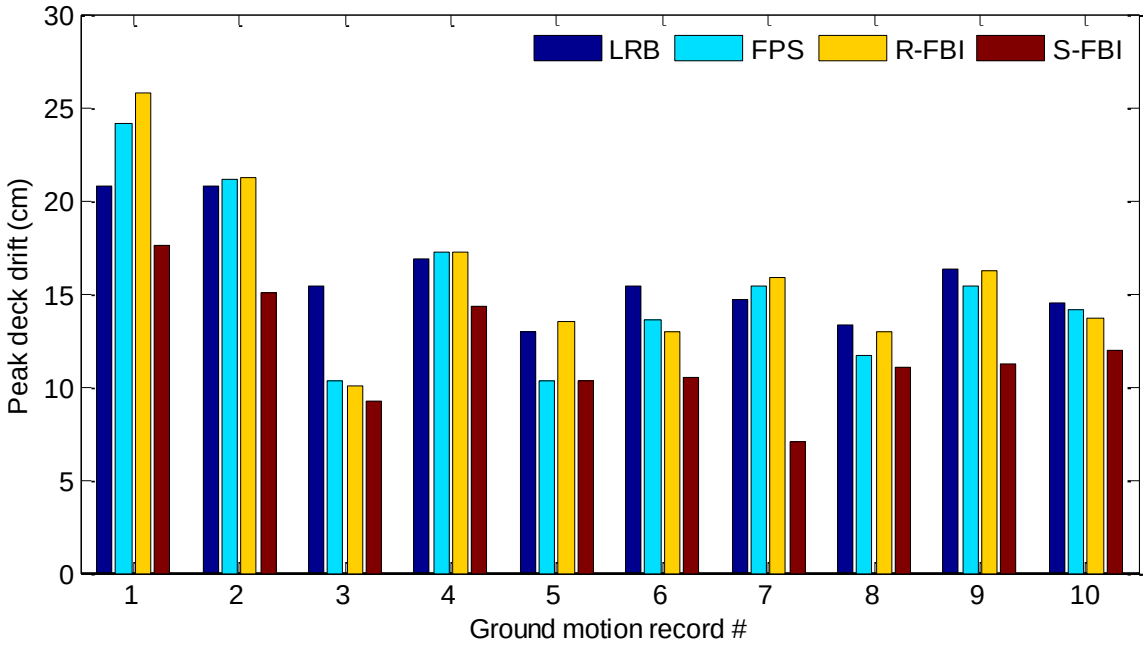

Figure 8-7 Peak deck drift for the various isolation systems subjected to near-field earthquakes

The sufficient restoring force capacity of isolation systems is a fundamental requirement in current codes for the design of seismically isolated structures. One indication of inadequate restoring capability is large residual displacements after the end of the seismic event. Figure 8-8 shows the residual displacement of various isolation systems subjected to different earthquakes. It is observed that the S-FBI system successfully recovers its deformations at the end of earthquake motions. This almost perfect restoring characteristic of the S-FBI system can be explained by the re-centering ability of NiTi shape memory alloys. For the other isolation systems, considerable residual displacements are present for some of the excitation cases. For instance, the residual displacement of the isolator for the San Fernando (record #3) earthquake is

observed to be 46 mm, 26 mm and 16 mm for the R-FBI, FPS and LRB systems, respectively.

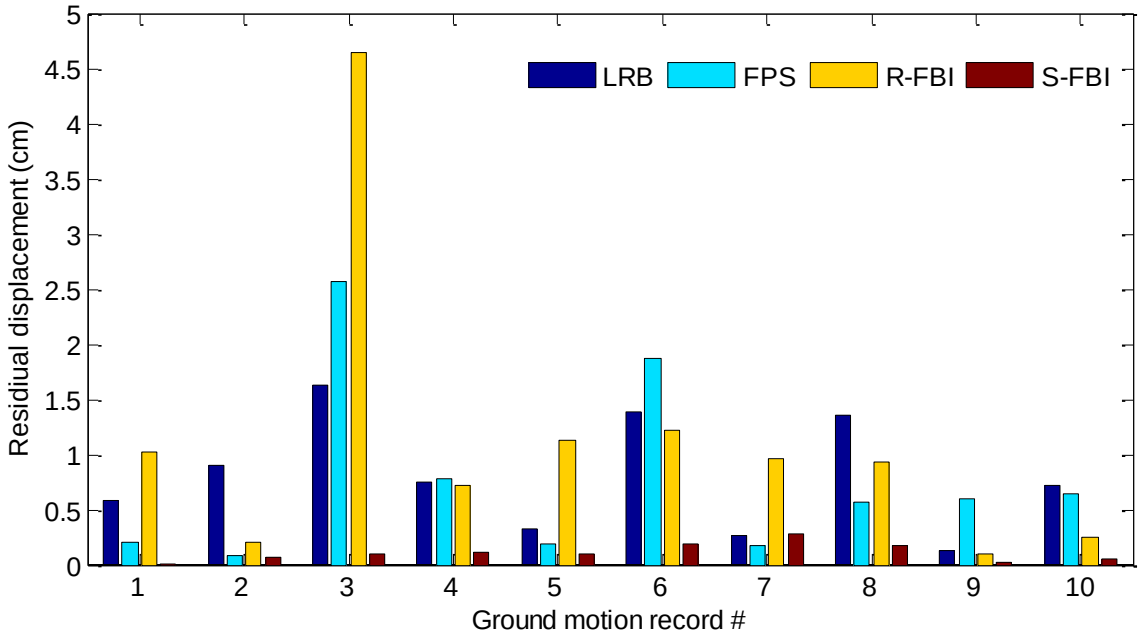

Figure 8-8 Peak residual isolator displacement for the various isolation systems subjected to near-field earthquakes

The peak deck acceleration responses for the various isolation systems subjected to different earthquakes are illustrated in Figure 8-9. In general, larger peak deck accelerations appear with the S-FBI and LRB systems in all excitation cases, while the FPS and R-FBI systems have smaller values for this response quantity. Specifically, the S-FBI system has larger values than the LRB system from 16% to 2% for the ten records included in this study, and the R-FBI system has slightly lower values than the FPS system.

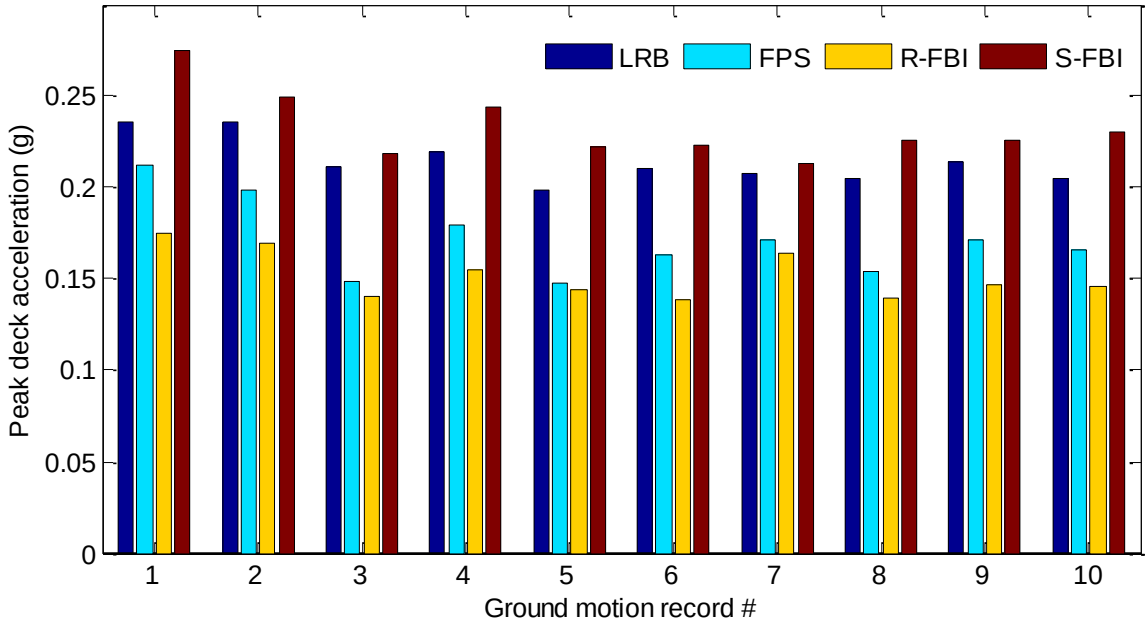

Figure 8-9 Peak deck acceleration for the various isolation systems subjected to near-field earthquakes

Figure 8-10 shows the peak normalized base shear for different isolation systems subjected to near-field earthquakes. The largest values of the peak normalized base shear are mostly observed either in the S-FBI system or in the LRB system for different excitation cases. In general, the peak normalized base shear is similar for the FPS and R-FBI systems, but somewhat larger using the FPS system for several earthquakes. Among sliding-type isolators, the larger base shear observed in the S-FBI system can be explained by the larger forces transmitted to the piers from the deck due to higher stiffness of the SMA device compared to the post-yielding stiffness of the FPS or R-FBI system.

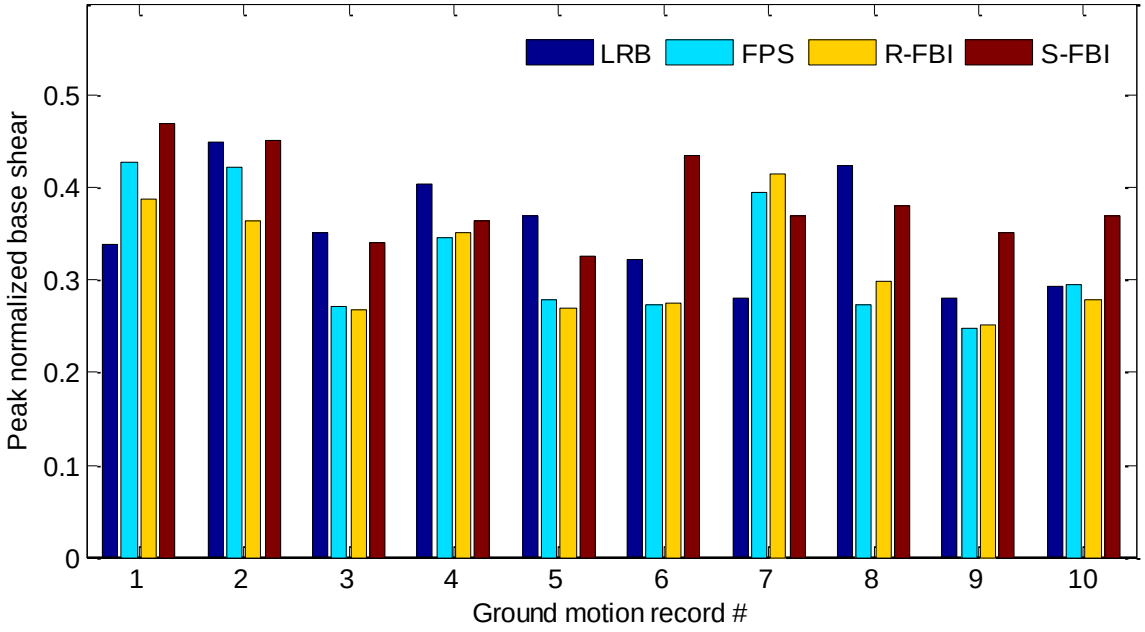

Figure 8-10 Peak normalized base shear for the various isolation systems subjected to near-field earthquakes

8.5.2 Sensitivity Analysis

In this section, a sensitivity analysis is conducted to evaluate the effects of design parameters of each isolation system on the seismic response of the isolated bridge. The response quantities evaluated in the parametric study include: (i) the ratio between peak deck drift of the isolated and non-isolated bridges $u_{d\ max} / u_{d\ max(ni)}$; (ii) residual isolator displacement; (iii) the ratio between peak deck acceleration of the isolated and non-isolated bridges $a_{d\ max} / a_{d\ max(ni)}$; and (iv) the ratio between peak base shear of the isolated and non-isolated bridges $V_{b\ max} / V_{b\ max(ni)}$.

One of the important design parameters for an isolation system is the isolation period since seismic isolation aims to lengthen the fundamental period of the structure in

order to keep the period of structure away from energy containing range of the ground motions. Although the ratio between fundamental periods of isolated T_b and non-isolated structures T_s is usually used to describe the period separation, the additive period shift T_{shift} defined below is used here.

$$T_{shift} = T_b - T_s \tag{8-12}$$

Unlike the period ratio, the additive period shift can characterize the effectiveness of the isolation system for both short period and long period superstructures (Sayani and Ryan, 2009). The values of T_{shift} from 1.5 to 4 are considered in this study.

Figure 8-11 shows the variation of the mean of the response quantities described above as a function of T_{shift} for various isolation systems subjected to different earthquakes. It is clearly shown that utilizing the S-FBI system results in smaller deck drifts compared to other three isolation systems. As expected, increasing period shift produces larger deck drifts for all the isolation systems considered. Also, note that the S-FBI system recovers all the isolator deformations after the seismic event independent from the chosen value of T_{shift}. On the other hand, other isolation systems experience significant residual deformations, especially for large values of T_{shift}. These results indicate again the advantage of employing superelastic SMAs in the isolation system as a re-centering device. In general, it can be seen that the peak deck acceleration and base shear tend to decrease with increasing T_{shift}. It is noticed that the S-FBI system has higher values for peak deck acceleration and peak base shear for most of the cases than other isolators. However, the S-FBI system can achieve similar reductions in peak deck

acceleration and base shear with other isolation systems for large values of T_{shift}, while it still has smallest deck drift and no residual isolator displacements at these values of T_{shift}.

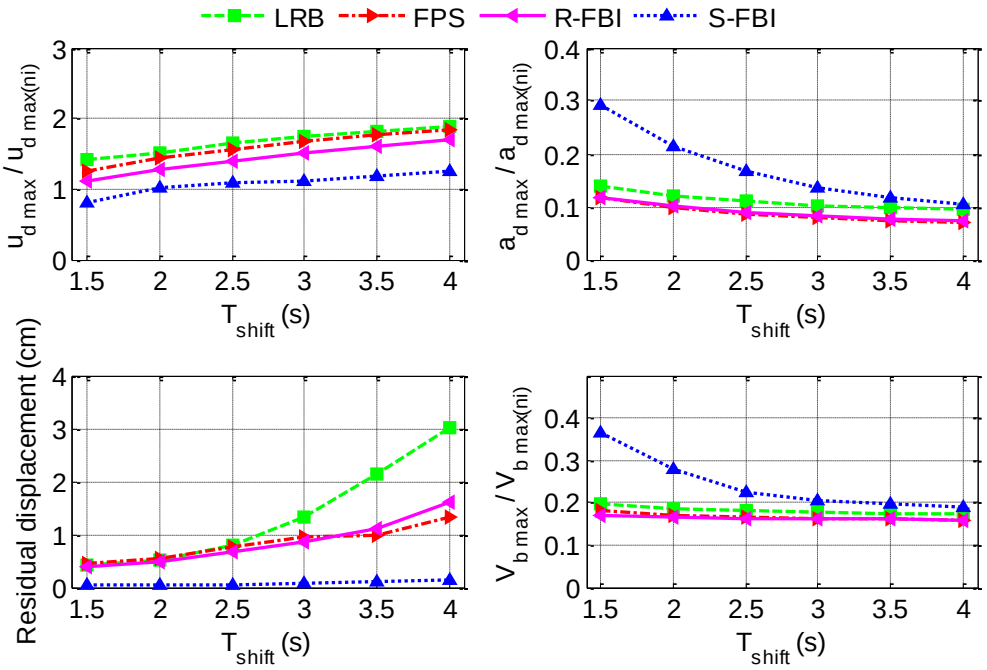

Figure 8-11 Variations of the mean response quantities with T_{shift} for various isolation systems

Another design parameter considered in this study is the yield strength F_o for the LRB system, and the coefficient of friction μ for the other isolation systems. The variations of the mean of the response quantities with F_o or μ for considered isolation systems are shown in Figure 8-12. In general, it is noticed that the peak deck acceleration almost linearly increases with the F_o or μ for all considered isolation systems with the largest values observed for the S-FBI system. The peak deck drift initially decreases with the increasing values of F_o or μ for all isolation systems. However, it remains almost constant for the FPS and R-FBI systems and it experiences

modest decreases for the LRB and S-FBI systems when F_o or μ is increased over 0.15. The S-FBI system has again the smallest bearing displacement without any residual deformation. The other isolation systems tend to have residual deformations for most of the cases with larger values observed for higher values of F_o or μ.

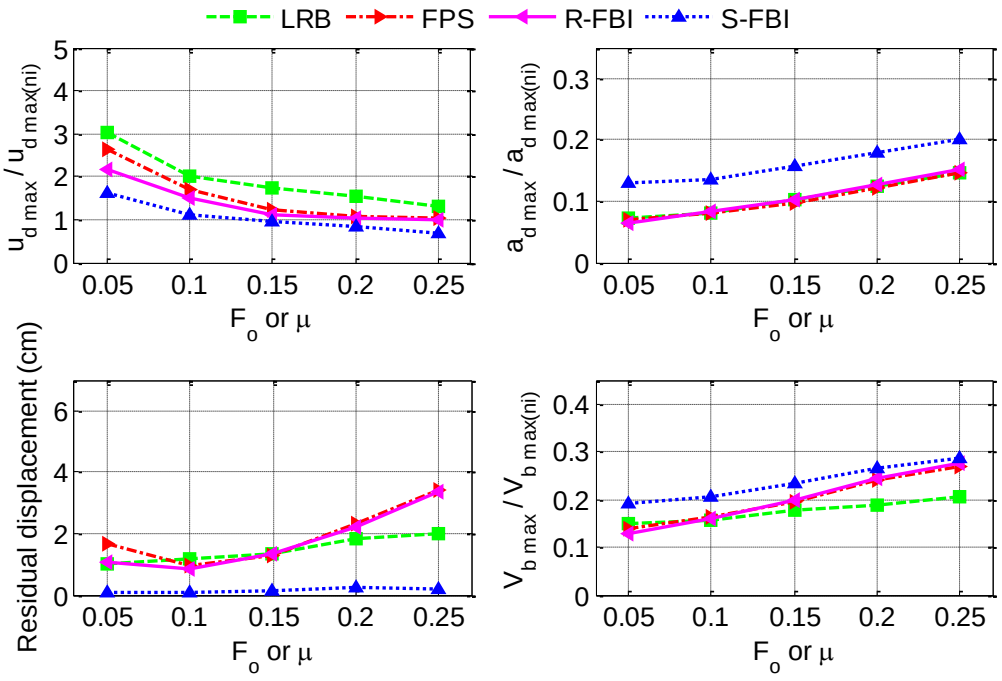

Figure 8-12 Variations of the mean response quantities with F_o or μ for various isolation systems

8.6 Closure

This section aims to evaluate the effectiveness of the S-FBI systems for protecting bridge structures against near-field earthquakes by performing a comparative parametric study. The other isolation systems considered here include the LRB system, the FPS system and the R-FBI system. A three-span continuous bridge is selected for

the numerical studies and modeled as two-degree-of-freedom-system. A total of ten historical near-field earthquakes are modified using the RspMatch2005 to match their response spectra with a target response spectrum and are used in the simulations. Nonlinear time history analyses of the bridge with different isolation systems are performed. First, the peak response quantities of the isolated bridge are presented for the recommended values of design parameters for each isolation system. Then, the sensitivity of the seismic response of the isolated bridge to the design parameters of each isolation system is investigated. The results show that the S-FBI system can successfully protect bridge structures from damaging effects of the near-field earthquakes. In particular, the S-FBI system results in the smallest deck drift compared to the other isolation system, while it can at the same time achieve similar values for the deck acceleration and normalized base shear with the other isolation system if the design parameters of the S-FBI system are judiciously selected. It is also revealed that the S-FBI system has excellent re-centering ability and almost always recovers its deformations after a seismic event, while residual deformations are typically observed for other isolation systems considered in this study.

9. EVALUATION OF THE PERFORMANCE OF THE S-FBI SYSTEM CONSIDERING TEMPERATURE EFFECTS

9.1 Introduction

As discussed in Section 2, there have been several studies that investigate the use of SMAs in seismic isolation systems for protecting buildings or bridges. However, in these studies, the effect of environmental temperature on the performance of SMA components has not been addressed (Zhang *et al.*, 2008). In a study in which the temperature effects was considered, Dolce *et al.* (2007a) compared the performance of three different sliding-type isolation systems that employ rubber, steel or shape memory alloys as auxiliary device. They reported a high sensitivity to temperature for the SMA isolation system. In particular, they found variations in peak displacement response up to 103% and in maximum isolator force up to 33% for a $\pm 30°C$ temperature change.

In this section, the seismic performance of the superelastic friction base isolator (S-FBI) system is investigated at various outside temperatures (Ozbulut and Hurlebaus, 2010e). In order to evaluate the performance of the S-FBI system for a different numerical example, a five-span continuous bridge is selected and modeled as 2-DOF system. Although the effectiveness of the S-FBI system during the near-field earthquakes is studied in the previous sections, the performance of the S-FBI system during the ground motions with far-field characteristics does not evaluated. Therefore, in this section, two far-field and two near-field ground motion records are selected for time history analysis of the isolated bridge. The temperature effects on steel-Teflon sliding bearings are considered by employing a modified viscoplastic model and using

different model parameters for each temperature. An optimization is performed to determine design parameters of the SMA device using a multi-objective genetic algorithm. The structural response of the isolated bridge at different environmental temperatures is studied by conducting nonlinear time history analyses.

9.2 Model of Isolated Bridge Structure

The bridge considered in this study has a five-span continuous deck with a total length of 200 m and a width of 12 m (Lee and Kawashima, 2007). Four reinforced concrete columns that have a height of 12 m and two abutments support the superstructure of the bridge. Here, the bridge is isolated using steel-Teflon sliding bearings that utilize an SMA device to provide re-centering force and additional damping. One of the interior spans is selected as analytical unit and modeled as a two-degree-of-freedom system as shown in Figure 9-1. The effective masses of deck and column are given as 600 and 243.15 ton, respectively. The columns are assumed to be perfect elastoplastic with an initial stiffness of 112700 kN/m and yield displacement of 0.0309 m. Also, 2% viscous damping is assumed for the piers.

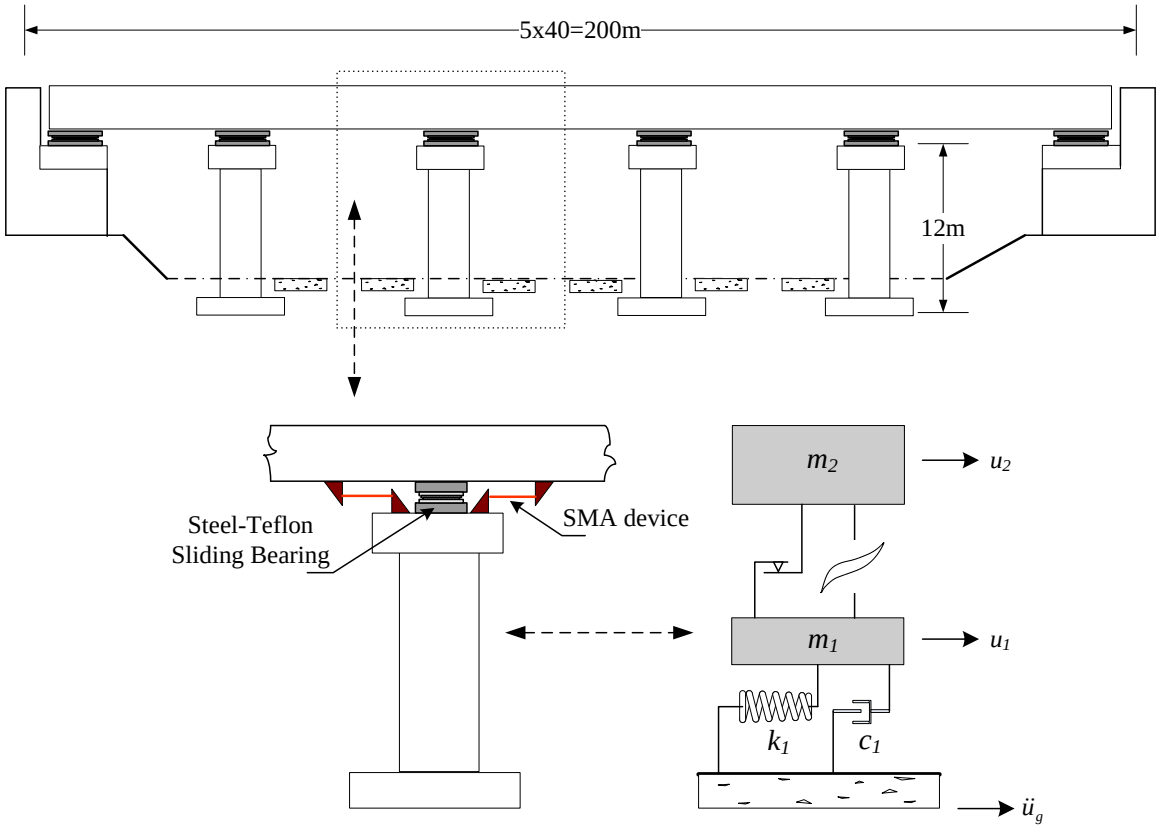

Figure 9-1 Five-span continuous bridge and its model with sliding bearings and SMA device

The equations of motion are

$$\begin{aligned} m_1\ddot{u}_1 + F_p - F_{IS} &= -m_1\ddot{u}_g \\ m_2\ddot{u}_2 + F_{IS} &= -m_2\ddot{u}_g \quad , \end{aligned} \tag{9-1}$$

where m_1, m_2 and u_1, u_2 are the masses and displacements of pier and deck, respectively, and $\ddot{u}_g$ is the ground acceleration. F_p represents nonlinear pier force and computed as

$$\begin{aligned} F_p &= \alpha k_1 u_1 + (1-\alpha) k_1 u_y z + c_1 \dot{u}_1 \\ u_y \dot{z} &+ \gamma |\dot{u}_1| z |z|^{n-1} + \beta \dot{u}_1 |z|^n - \dot{u}_1 = 0 \end{aligned} \tag{9-2}$$

where α is the ratio of the post yielding to the elastic stiffness, u_y is the yield displacement of piers, and z is the hysteretic Bouc-Wen quantity governed by the above differential equation and the dimensionless parameters γ, β and n are taken as 0.5, 0.5, and 1, respectively. F_{IS} denotes restoring force of isolation systems. Hence, F_{IS} is the sum of the nonlinear force of SMA device and frictional resistance force of steel-Teflon sliding bearings.

A hysteretic model is used to simulate the force of the sliding bearings. The frictional force at a sliding interface is given by

$$F_f = \mu_s WZ \tag{9-3}$$

where μ_s represents the coefficient of friction, W is the normal load carried by the bearing interface, and Z is a hysteretic dimensionless quantity computed from following equation

$$Y\dot{Z} + \gamma|\dot{u}_b||Z|^{n-1} + \beta\dot{u}_b|Z|^n - \dot{u}_b = 0, \tag{9-4}$$

where Y is the yield displacement of the sliding bearing chosen as 0.0005 m and, γ, β, and n are dimensionless parameters that control the shape of the hysteretic curve and have the values of 0.9, 0.1 and 1, respectively. Also, $u_b = u_2$-u_1 is the deformation of the sliding bearings.

Experimental studies showed that the coefficient of friction of steel-Teflon sliding bearings tends to decrease with increasing stress and increase with increasing velocity. It may be approximated at sliding velocity $\dot{u}_b$ as

$$\mu_s = \mu_{\max} - \Delta\mu \exp\left(-a|\dot{u}_b|\right), \tag{9-5}$$

where μ_{max} is the coefficient of friction at very high velocities, and $\Delta\mu$ is the difference between the coefficient of friction at very high and very low velocities. Furthermore, a is constant for a given bearing pressure and condition of sliding interface. Dolce *et al.* (2005a) studied the frictional behavior of steel-Teflon sliding bearings, and specified the parameters μ_{max}, $\Delta\mu$, and a for different combination of bearing pressure, condition of interface and temperature. The temperatures considered in their study are -10°C, 20°C and 50°C, and the above mentioned model parameters are specified for these temperatures. Here, a linear interpolation is made to approximate the corresponding parameters for 0°C, 20°C and 40°C. The values of μ_{max}, $\Delta\mu$, and a for three different temperatures and for a 28.1 MPa bearing pressure and non-lubricated bearing interface are given in Table 5-2.

The fuzzy model described earlier is used to predict the instantaneous force from the SMA elements at different temperatures. Since the design parameters of SMA device, i.e., the length and cross-sectional area of NiTi wires, depend on the design earthquake intensity level, the ground motions that are considered in this study are described first. Then, a genetic algorithm-based multi-objective optimization method is introduced for the selection of design parameters of the SMA wires.

9.3 Ground Motions Used for Analyses

In this section, RspMatch2005, introduced in Section 5, is employed to obtain historical accelerograms that are spectrally matched to a given spectrum at multiple damping levels for use in time-history analyses. The target response spectrum is

constructed using the AASHTO LRFD bridge design specifications (AASHTO, 2009) for site class B with peak ground acceleration of 0.40 g and is shown for damping levels of 5%, 10% and 20% in Figure 9-2. In order to start RspMatch2005 process, a suite of initial accelerograms that may be linearly scaled to have an approximate match to the spectral shape of 5% damped target spectrum is needed. Seven historical earthquake records (1940 El Centro, 1968 Hachinohe, 1986 North Palm Spring, 1994 Northridge, 1995 Kobe, 1999 Chi-Chi, and 1999 Bolu) are considered for initial selection, and their match with the target spectrum is assessed using the root mean square (RMS) difference between the normalized spectral acceleration of observed and target spectra (ΔSAn_{RMS}) which is given as (Hancock *et al.*, 2008).

$$\Delta SAn_{RMS} = \sqrt{\frac{1}{N_p}\sum_{i=1}^{N_p}\left(\frac{PSA_0(T_i)}{PGA_0} - \frac{PSA_s(T_i)}{PGA_s}\right)^2}, \qquad (9\text{-}6)$$

where N_p is the number of periods, $PSA_0(T_i)$ is the pseudo spectral acceleration from the record at period T_i, $PSA_s(T_i)$ is the target pseudo spectral acceleration at the same period; PGA_0 and PGA_s are the peak ground acceleration of the accelerogram and zero-period anchor point of target spectrum. After comparing ΔSAn_{RMS} of seven ground motions, 1940 El Centro, 1968 Hachinohe, 1994 Northridge, and 1995 Kobe records are selected as seed accelerograms due to better match of their spectral shape. Note that the El Centro and Hachinohe earthquakes have far-field characteristics and Northridge and Kobe earthquakes are typical near-field ground motions.

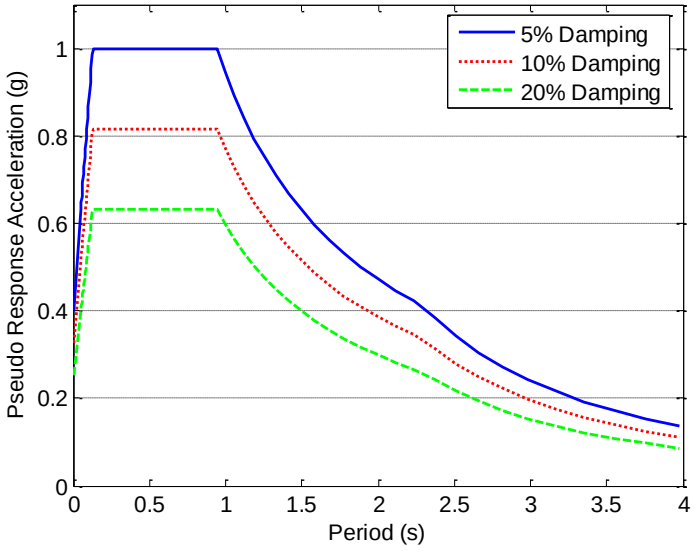

Figure 9-2 Target spectrum at different damping levels

The selected seed accelerograms are matched to the target spectra at multiple damping levels using RspMatch2005. Figure 9-3 illustrates adjusted acceleration time-histories for El Centro, Hachinohe, Kobe, and Northridge earthquakes. These acceleration records are used as seismic input in the time history analyses of the isolated bridge that is discussed in the next section.

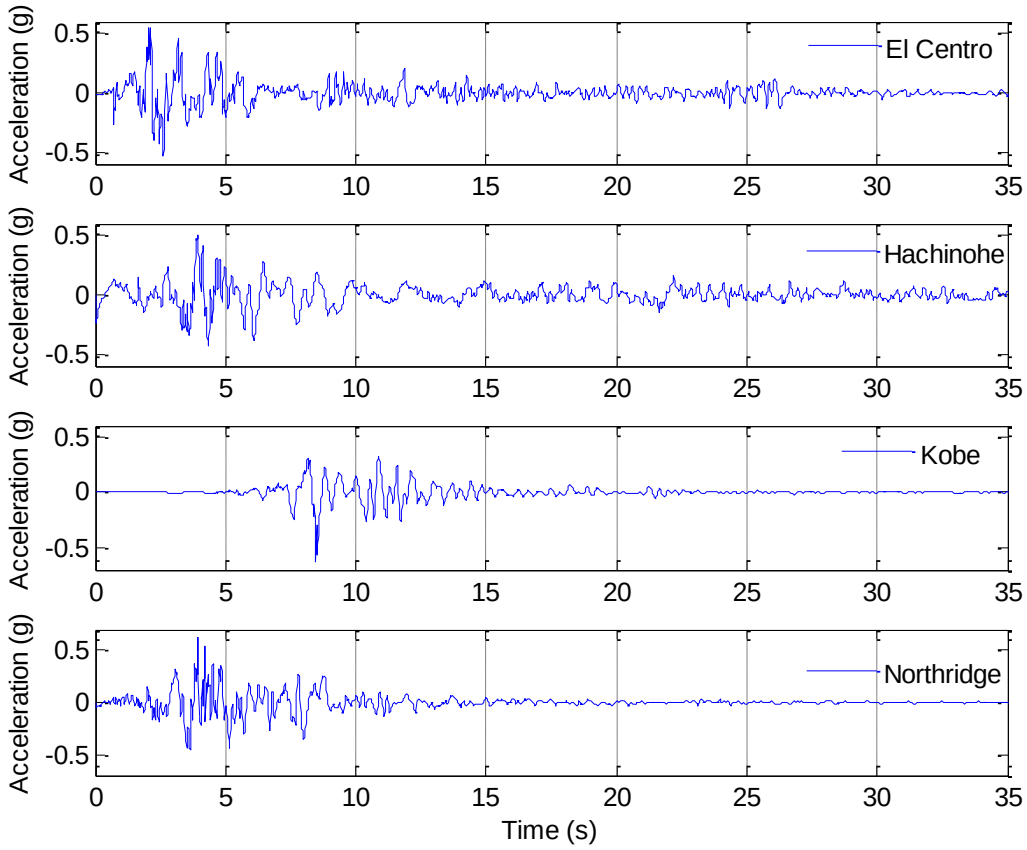

Figure 9-3 Spectrally matched acceleration time histories used in simulations

9.4 Design of SMA Device

In order to choose the design parameters of SMA re-centering damping device, a trial and error is usually required. It is possible alter the nonlinear stiffness and damping added to the system by changing the geometry of the SMA elements. One of the main concerns in design is to keep the maximum strain of SMA wires during the strongest motion within the recoverable superelastic strain range (up to 6-7% for NiTi wires) of the material. That requires long wire length. Also, the cross-sectional area of the SMA

wires should be large enough to develop the required re-centering force for the isolation system. Other objectives in design are to limit the shear force transferred to the piers and minimize the total volume of the material that is used for the device.

In this study, a multi-objective genetic algorithm optimizer, namely NSGA-II, is used in order to determine the optimum length and area of NiTi wires. NSGA-II is a computationally fast and elitist evolutionary algorithm based on a non-dominated sorting approach. Among a pool of initial random candidate values that reside within a user-defined range, NSGA-II generates a set of Pareto-optimal solutions through an iterative process. The detailed description of the NSGA-II algorithm can be found in Deb *et al.* (2002). Here, three objective functions, namely, peak deck relative displacement, peak deck acceleration, and peak base shear, are considered. All three have to be minimized simultaneously. In order to avoid training with several historical ground motions during the optimization process, the spectrally matched Northridge accelerogram is used as seismic input. A population of size 50 is selected and each simulation is run for 100 generations. In order to discourage Pareto-optimal solutions that cause SMA wires to experience more than 6% strain, a fixed large penalty is added to all objectives if maximum strain of the wires is over 6%. The optimization is devised for an outside temperature of 0°C since it is observed that SMA wires are exposed to larger strains at this temperature during preliminary investigations. The results of genetic algorithm optimization reveal that selecting a wire length of 2.35 m and a cross-sectional area of 620 mm^2 that corresponds to 350 NiTi wires with a diameter of 1.5 mm for each SMA

device gives an optimal solution. Therefore, these values are used for the SMA device in the numerical simulations described below.

9.5 Results

The nonlinear equations of motion given above in equation (9-1) are solved using a fourth-order Runge-Kutta method with variable time step. The response time histories of the bridge isolated by the S-FBI system are obtained against the artificial ground motions described above for different environmental temperatures. In this section, first the results for all excitation cases are summarized, and then displacement and acceleration time histories as well as hysteretic force-displacement curves of the isolation system components for the Northridge earthquake case are presented.

Figure 9-4 shows the results for maximum drift of the pier and deck at 0°C, 20°C, and 40°C for the considered excitations. It can be seen that the maximum pier displacement usually increases with decreasing environmental temperature. The maximum change in peak pier displacement is +10% and -11% when temperature increases or decreases 20°C from reference temperature of 20°C, respectively. The peak relative displacement of the deck has its maximum value at 40°C for all the excitation cases except the Kobe earthquake. One reason for this increase in deck drift at higher temperatures is the lower coefficient of friction of the sliding bearings at these temperatures. Since large portion of energy dissipation is provided by frictional behavior of the sliding bearings, the decrease in the friction coefficient at higher temperatures results in an increase in the deck displacement response. However, the

larger frictional force at low temperatures increases the demand on the piers and causes larger pier drift. The maximum variation of peak deck drift as temperature changes $\pm 20°C$ from the reference temperature is about 13% which is observed for El Centro earthquake.

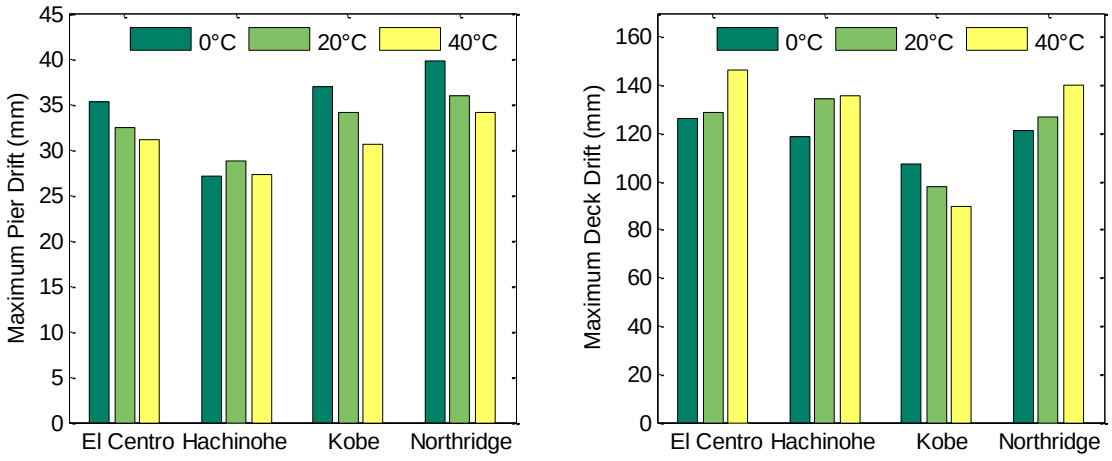

Figure 9-4 Maximum drifts of pier and deck at different temperatures

Figure 9-5 shows the residual pier drift ratio and residual isolation deformation at different temperatures for the considered ground motions. As mentioned above, since the frictional force transferred to piers are larger at low temperatures and SMA re-centering force reduces with decreasing temperature, larger pier drift ratios are observed at 0°C for all cases except the Hachinohe excitation. However, the largest residual pier drift ratio is about 0.12% for the Northridge record and below 0.06% for the other ground motions. The S-FBI system recover almost all deformations for most of the cases. The largest residual deformation observed for El Centro excitation at 0°C is about 2 mm.

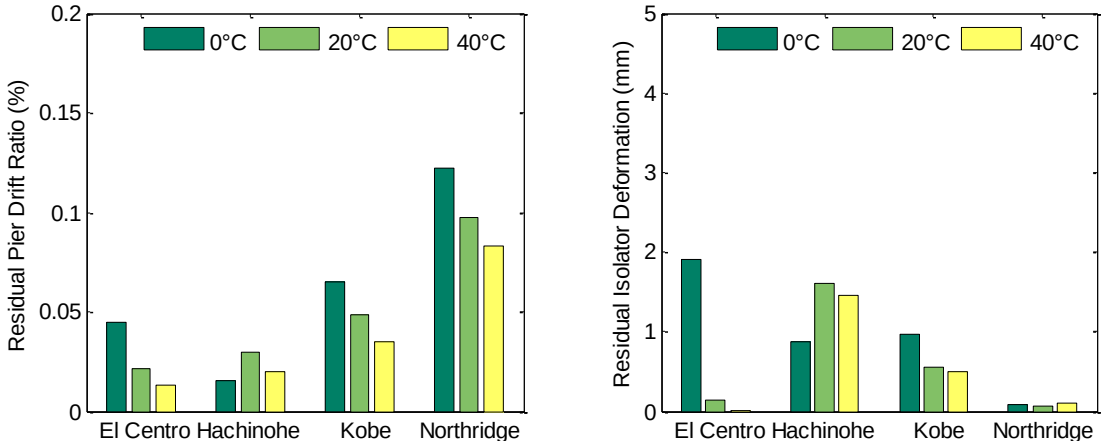

Figure 9-5 Residual pier drift ratio and residual deformation of the isolator at different temperatures

The variations of the maximum deck acceleration and the maximum base shear with temperature are given in Figure 9-6. It can be seen that there is no significant change in peak deck acceleration with the environmental temperature change. In particular, the maximum change in peak deck acceleration is about 1% for the El Centro and Hachinohe excitations, while it is about -4% and -8% for Kobe and Northridge, respectively when temperature decreases to 0°C. The slight increase in deck acceleration for the Kobe and Northridge excitations with increasing temperature can be attributed to the larger SMA re-centering forces at high temperatures. The maximum base shear experiences a highest increase of 6% for the Northridge record if the temperature drops to 0°C, and it reduces a maximum of 6% for the Kobe excitation if the temperature increase to 40°C.

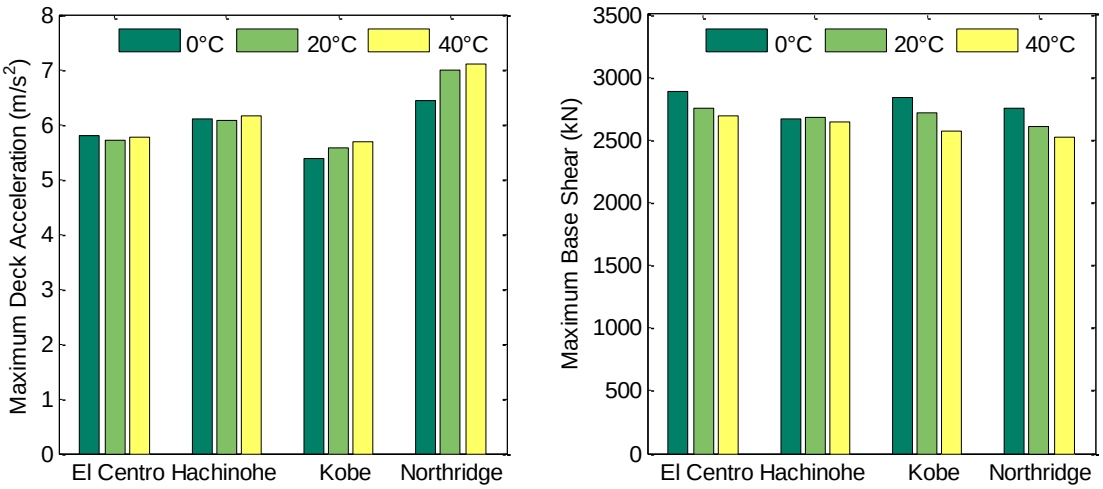

Figure 9-6 Maximum deck acceleration and maximum base shear at different temperatures

The time histories of the relative deck displacement and the absolute deck acceleration are illustrated in Figure 9-7 for the lowest and highest outside temperatures (0°C and 40°C) considered here for the Northridge excitation. As discussed above, the acceleration response of the deck is very similar at both temperatures, whereas the maximum relative displacement of the deck is slightly lower at 0°C.

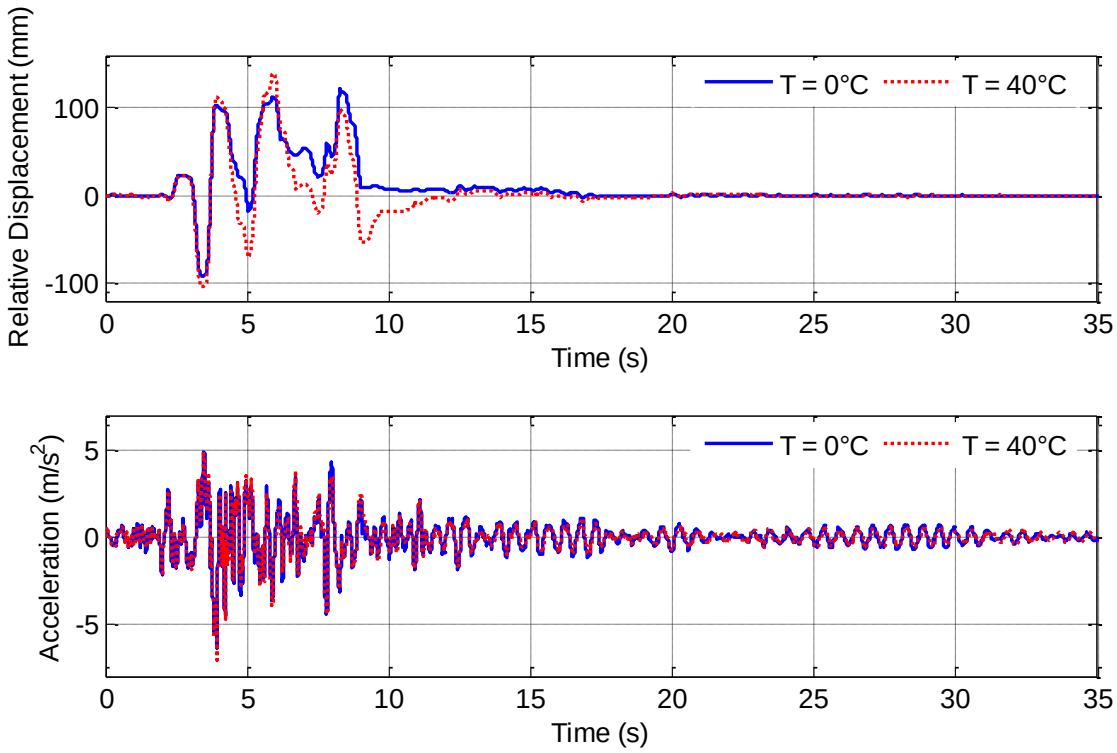

Figure 9-7 Time histories of deck relative displacement and deck acceleration at 0°C and 40°C

Figure 9-8 shows the force-displacement relationships of the isolation system components i.e., sliding bearing (SB) and SMA device together with the combined hysteresis curve at 0°C and 40°C during the Northridge excitation. It can be seen that the re-centering ability of the isolation system improves with increasing temperature while the maximum frictional force, i.e., energy damping capacity of the system decreases. The isolation system mainly dissipates the energy through friction while very modest contribution is available from the hysteretic behavior of the superelastic SMAs.

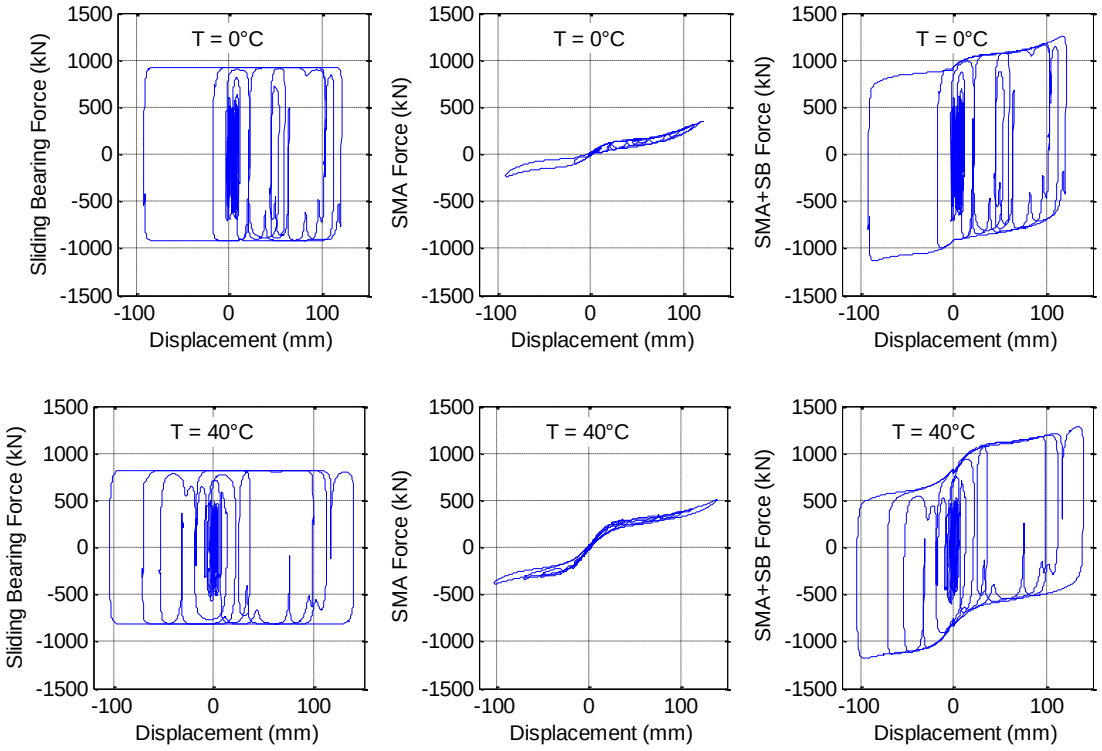

Figure 9-8 Hysteresis curves of isolation system and its components at 0°C and 40°C

Figure 9-9 compares the maximum forces of the sliding bearings, the SMA device, and the combined isolation system for different temperatures. The hysteresis loops of the SMA device are given for each temperature in the figure. It can be seen that the maximum friction force of the steel-Teflon bearings decreases with an increase in temperature due to the lower friction coefficient at higher temperatures. On the other hand, the re-centering force of the SMA device increases with the temperature. The maximum force generated in the SMA device at 0°C and 20°C is almost the same. That is because of significant strain hardening of the SMA wires at 0°C for large deformations. Therefore, the maximum SMA force at 0°C reaches the maximum level

observed at 20°C. However, as it can be seen from the SMA hysteresis curves, the SMA device has a higher stiffness and generates larger re-centering forces at higher temperatures. If the variation of the combined isolation system force with temperature is examined, it can be seen that it remains more stable since the difference in the forces generated on the sliding bearing and the SMA device offset each other. Nevertheless, it is apparent that the stiffness of the isolation system increases and the damping capacity of the isolation system decreases with increasing temperature.

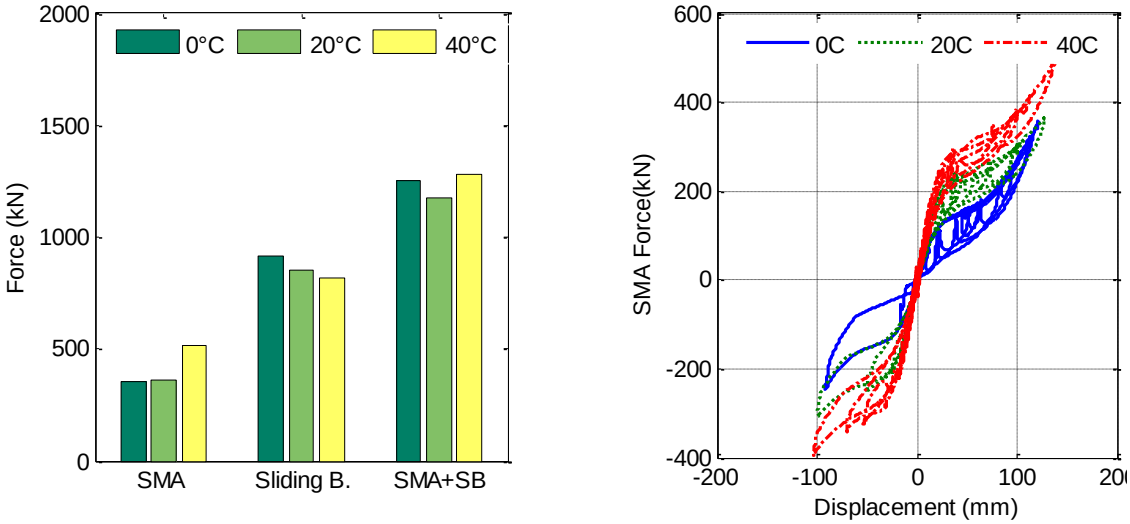

Figure 9-9 The variation of maximum forces of isolation system and its components with temperature

In order to assess whether seismic response of a bridge isolated by the SFBI system is more sensitive to the temperature dependent properties of sliding bearings or those of the SMAs, another set of simulations are performed. First, temperature dependency of the SMA behavior is neglected and the SMAs wires are modeled for an environmental temperature of 20ºC, while sliding bearing properties are changed for

each temperature. Then, the properties of the sliding bearings are assumed to be constant and equal to those at 20ºC, whereas variation of the SMA material response with outside temperature is considered. The spectrally-matched Northridge earthquake is used as an external excitation. The results are summarized in Figure 9-10. It can be seen that the temperature dependence of the frictional properties of the sliding bearing is contributing more to the variation of the seismic response of the isolated bridge. In particular, the higher frictional force of the bearing at low temperatures result in an increase in pier drift, and a reduction in deck relative displacement due to larger energy dissipation. Although, the change of SMA properties with changes in temperature also affects the results, the variation of the seismic response of the bridge is more modest for this case. For instance, as temperature changes $\pm 20°C$, there is only a 5% change in peak deck drift if the SMA properties change with the temperature while the sliding bearing properties are kept constant. However, the same change is 14% for the case of constant SMA material behavior and temperature dependent bearing properties. Also, note that for all cases the S-FBI system has no residual deformations at the end of ground motion.

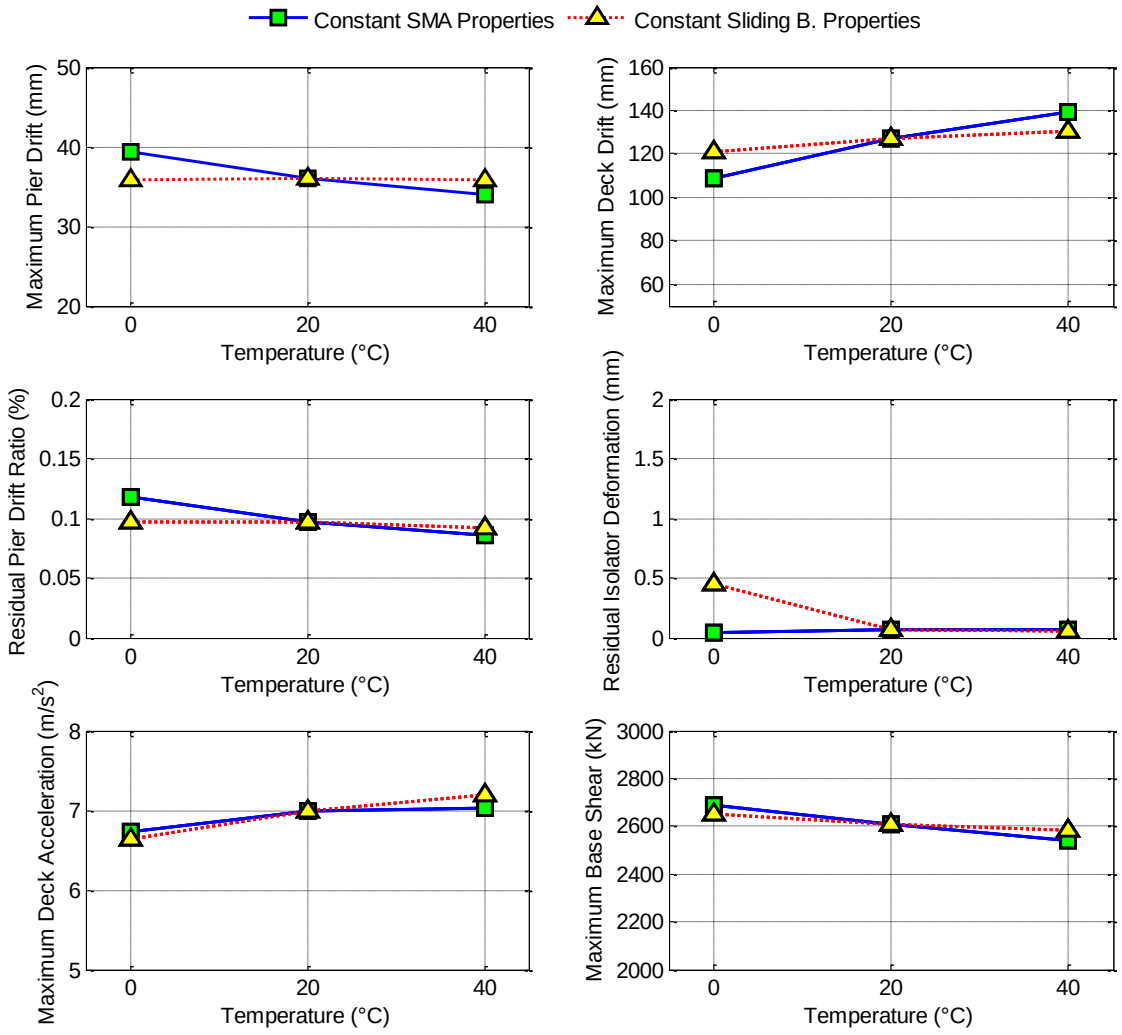

Figure 9-10 The variation of seismic response of the bridge with temperature for constant SMA properties and constant sliding bearing properties

Finally, to evaluate the effectiveness of the SMA-based sliding base isolation system (BIS), the seismic performance of the S-FBI system is compared with two benchmark cases: (i) the seismic response of the bridge incorporating only the pure-friction (P-F) BIS (i.e. sliding-type bearings without SMA devices) and (ii) the seismic response of the bridge incorporating a monolithic connection between the deck and the

top of the piers (i.e. non-isolated bridge). Nonlinear time-history analyses are performed for the temperature range considered in this study and ground motions described above.

Figure 9-11 and Figure 9-12 show the maximum deck drift, residual pier drift ratio and maximum base shear for the bridge isolated by the S-FBI system and the P-F sliding isolator and the non-isolated bridge for different ground motions. Also, the results are presented for outside temperatures of 0°C, 20°C, and 40°C. Note that the response for the isolated bridge cases varies with temperature while the results for the non-isolated bridge are constant for each temperature. As shown from the figure, the use of SMA-based sliding isolators decrease the seismic demand on the piers while simultaneously reducing the displacement demand of the isolators. Although the bridge isolated by the P-F sliding bearings also experience a decrease in the demand on the substructure, it has larger deck drifts than the SMA-based sliding isolators. Also, large residual isolator deformations are observed for the P-F isolation system due to the lack of re-centering force capability while the S-FBI system recovers almost all of its deformations as illustrated above in Figure 9-5.

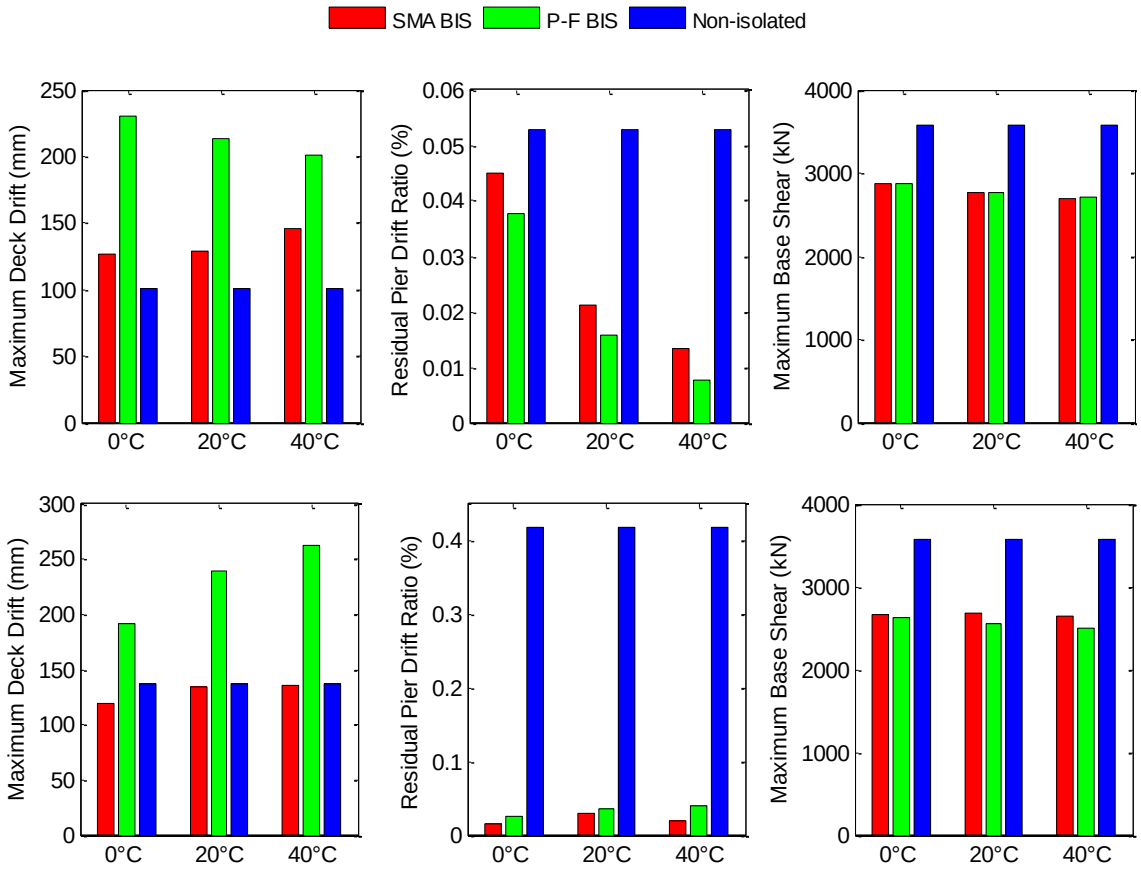

Figure 9-11 Seismic response comparison of different bridge configurations at various temperatures for (a) El Centro and (b) Hachinohe earthquakes

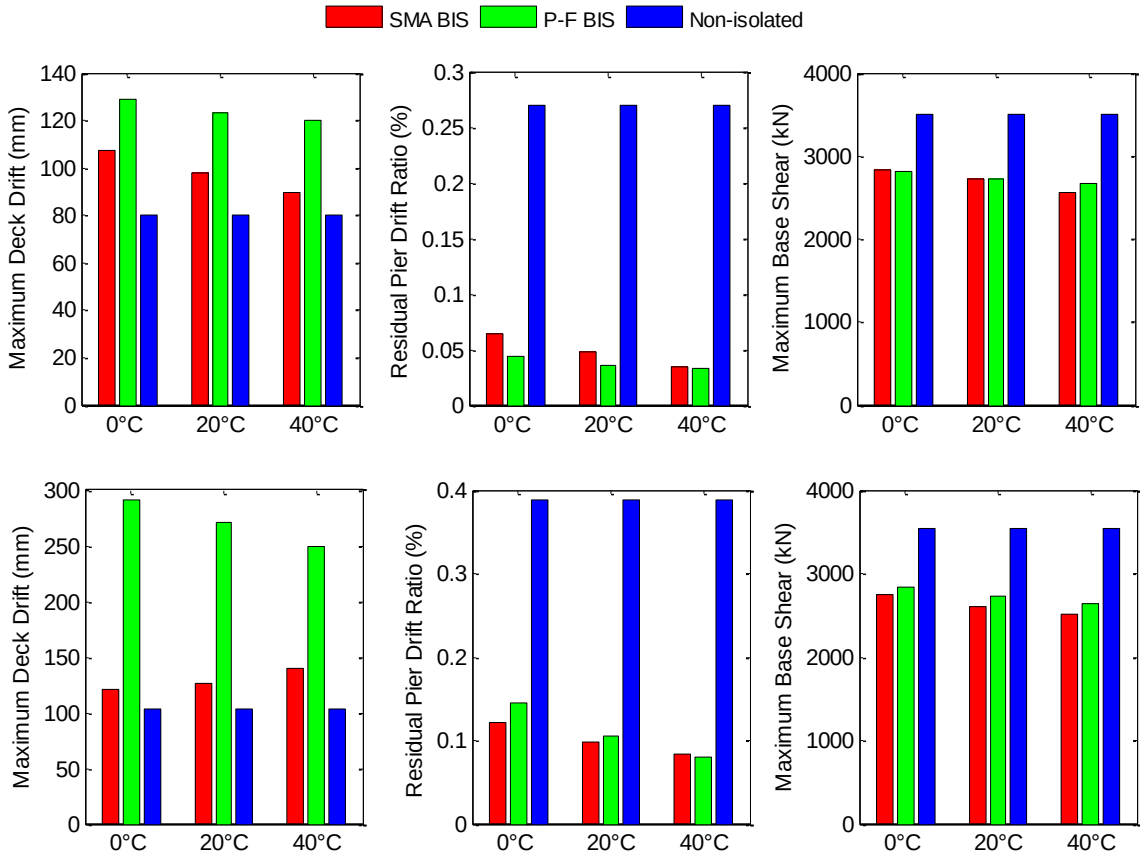

Figure 9-12 Seismic response comparison of different bridge configurations at various temperatures for (a) Kobe and (b) Northridge earthquakes

9.6 Closure

In this section, seismic performance of the S-FBI system is evaluated considering effects of outside temperature changes for a multi-span continuous bridge. Since temperature and loading rate significantly affect the behavior of superelastic NiTi wires, a neuro-fuzzy model that captures material response considering temperature and strain rate effects is first introduced. The temperature effects on steel-Teflon sliding bearings are considered by using a continuous hysteretic model with different model parameters

for each temperature. The length and cross-sectional area of the SMA device is optimized by employing a non-dominated sorting genetic algorithm. The program RspMatch2005 is used to obtain a suite of accelerograms for use in dynamic nonlinear analyses of the bridge.

Nonlinear time history analyses of the isolated bridge are conducted for three different outside temperatures. The results show that the temperature has a modest effect on the performance of bridges isolated by S-FBI systems. Specifically, there is a maximum of 13% difference on the displacement response of the bridges for all considered ground motions when temperature differs $\pm 20°C$ from the reference temperature of 20°C. Similarly, the acceleration response of the bridge varies a maximum of 8% with the temperature change while the difference is below 2% for most of the cases. Also, it is noted that the change in the forces generated in the sliding bearings and the SMA device counterbalance each other. While temperature increases, the frictional force of sliding bearings decreases, i.e., the damping capacity of the isolation system decreases. On the other hand, the initial stiffness and forward transformation strength of the SMA device increase with increasing temperature. Therefore, a larger re-centering force is available for high temperatures.

10. SUMMARY, CONCLUSIONS AND RECOMMENDATIONS

This dissertation presents an analytical study that explores the feasibility of using shape memory alloys in seismic isolation systems for improving the response of bridge structures during near-field earthquakes. First, experimental tests are conducted to characterize the behavior of SMAs at various temperatures and loading frequencies. The results indicate that the temperature and loading rate have significant effects on the behavior of NiTi wires. A neuro-fuzzy model that is capable of simulating temperature- and rate- dependent mechanical response of superelastic SMAs is developed. It is shown that the developed model can successfully emulate the superelastic behavior of SMAs considering dynamic effects at different temperatures.

The performances of two SMA-based isolation systems are investigated for seismic protection of bridges next. The first system, named superelastic-friction base isolator system, consists of a steel-Teflon sliding bearing that filters out the earthquake forces by providing frictional sliding interfaces and a superelastic SMA device that provides a re-centering mechanism and absorbs seismic energy through hysteresis of the SMA elements. The second smart isolation system, called SMA/rubber-based isolation system, consists of a laminated rubber bearing that decouples the superstructure from the bridge piers and an SMA device that provides additional energy dissipation and re-centering capacity. A three-span continuous bridge is modeled as a two-degrees-of-freedom system with the SMA-based isolation systems. In order to generate near-field earthquakes that are used as external excitations in the simulations, the time domain response spectral matching of several historical records is performed with the program

RspMatch2005. Sensitivity analyses are conducted to evaluate optimum values of design parameters of the SMA-based isolation systems for mitigating the response of the highway bridges against near-field earthquakes.

Comparative performance studies are carried out to evaluate the effectiveness of SMA-based isolation systems. The performances of the two SMA-based isolation systems are compared using energy methods. It is observed that the S-FBI system attracts smaller quantities of input energy than the SRB system. It is also shown that the bridge structure isolated by either the SRB isolation system or the S-FBI system has very similar results for the peak deck drift response; however, the S-FBI system offers larger reductions on peak deck acceleration and peak base shear.

After it is shown that the S-FBI system has the superior behavior over the SRB isolation system, the performance of the S-FBI system is further examined. First, the efficacy of the S-FBI system is compared with most commonly used isolation systems. The other isolation systems considered in the comparison include the LRB system, the FPS system and the R-FBI system. The results indicate that the S-FBI system can effectively mitigate the response of highway bridges against near-field earthquakes with excellent re-centering ability when the design parameters are judiciously selected. Then, a detailed analytical investigation is carried out to evaluate the effects of temperature on the performance of the S-FBI system. The results show that the temperature has modest effects on the performance of bridges isolated by the S-FBI system. Also, it is noted that the change in the forces generated in the sliding bearings and the SMA device counterbalance each other.

Overall, the S-FBI system appears to effectively limit the response of the bridges subjected to earthquake ground motions. Also, it is observed that S-FBI isolators recover almost all of their deformations, which eliminates the need of bearing replacement after a strong earthquake.

The NiTi shape memory alloys used in this study completely lose their superelasticity below -10°C. Therefore the results cannot be generalized for the regions with severe winter conditions. This drawback can be eliminated by modifying the composition of the NiTi material to obtain superelastic SMAs with a larger operating temperature range. Also, the ratio of post forward transformation stiffness to initial stiffness of the SMA wires α is taken to be constant. A further study can investigate the effect of α on the response of seismically isolated bridges with SMA-based systems.

The isolated bridge considered in this study is modeled using a simplified structural model. The effects of pounding between deck and abutment are not considered. The interaction of the isolator behavior in two directions is not considered. A future study should be conducted to investigate the validity and accuracy of this model by comparing the results with those obtained from a detailed 3-D model of the isolated bridge structure.

Finally, this study focused only on the seismic protection of bridge structures using SMA-based isolation systems. A future study is still required to explore the efficacy and optimum design parameters of the S-FBI system for improving the seismic response of multi-story building structures subjected to near-field earthquakes.

REFERENCES

AASHTO. (2009). *Guide specifications for LRFD seismic bridge design*. *AASHTO*, 1st Ed., Washington, D.C.

Aizawa, S., Kakizawa, T., and Higasino, M. (1998). "Case studies of smart materials for civil structures." *Smart Materials and Structures*, 7, 617-626.

Alam, M. S., Youssef, M. A., and Nehdi, M. (2008). "Analytical prediction of the seismic behaviour of superelastic shape memory alloy reinforced concrete elements Engineering Structures, 30, 3399-3411.

Andrawes, B. and DesRoches, R. (2005). "Unseating prevention for multiple frame bridges using superelastic restrainers." *Smart Materials and Structures*, 14(3), 60-67.

Andrawes, B. and DesRoches, R. (2007a). "Effect of ambient temperature on the hinge openings in bridges with shape memory alloy seismic restrainers." *Engineering Structures*, 29, 2294-2301.

Andrawes, B. and DesRoches, R. (2007b). "Comparison between shape memory alloy restrainers and and other bridge retrofit devices." *Journal of Bridge Engineering*, 12(6), 700-709.

Andrawes, B., Shin, M., and Wierschem, N. (2010). "Active confinement of reinforced concrete bridge columns using shape memory alloys." *Journal of Bridge Engineering*, 15, 81-89.

Araya, R., Marivil, M., Mir, M., Moroni, O, Sepulveda, A. (2008). "Temperature and grain size effects on the behavior of CuAlBe SMA wires under cyclic loading." *Materials Science and Engineering A* 496, 209-213.

Auricchio, F. (2001). "A robust integration-algorithm for a finite-strain shape memory-alloy superelastic model." *International Journal of Plasticity*, 17(7), 971-990.

Auricchio, D., Fugazza, D., and DesRoches, R. (2006). "Earthquake performance of steel frames with nitinol braces." *Journal of Earthquake Engineering*, 10, 1, 45-66.

Auricchio, F., and Lubliner, J. (1997). "A uniaxial model for shape-memory alloys." *International Journal of Solids and Structures*, 34, 3601-3618.

Auricchio, F., and Sacco, E. (1997). "A one-dimensional model for superelastic shape-memory alloys with different elastic properties between austenite and martensite." *International Journal of Non-Linear Mechanics*, 32, 1101-1114.

Auricchio, F., Fugazza, D., and DesRoches, R. (2007). "A 1D rate-dependent constitutive model for superelastic shape-memory alloys: formulation and comparison with experimental data." *Smart Materials and Structures*, 16, S39-S50.

Auricchio, F., Fugazza, D., and DesRoches, R. (2008). "Rate-dependent thermo-mechanical modelling of superelastic shape-memory alloys for seismic applications." *Journal of Intelligent Material Systems and Structures*, 19, 47-61.

Austin, M. A., and Lin, W. J. (2004). "Energy balance assessment of base isolated structures." *Journal of Engineering Mechanics*, 130(3), 347-358.

Azadi, B., Rajapakse, R. K. N. D., and Maijer, D. M. (2006). "One-dimensional thermomechanical model for dynamic pseudoelastic response of shape memory alloys." *Smart Materials and Structures*, 15, 996-1008.

Bartera, F., and Giacchetti, R. (2004). "Steel dissipating braces for upgrading existing building frames." *Journal of Constructional Steel Research*, 60, 751-769.

Bommer, J. J., and Acevedo, A. B. (2004). "The use of real earthquake accelerograms as input to dynamic analysis." *Journal of Earthquake Engineering*, 8(S1), 43-91.

Boroschek, R. L., Farias, G., Moroni, O., and Sarrazin, M. (2007). "Effect of SMA braces in a steel frame building." *Journal of Earthquake Engineering*, 11, 326-342.

Boyd, J. G., and Lagoudas, D. C. (1996). "Thermodynamical constitutive model for shape memory materials. Part I. The monolithic shape memory alloy." *International Journal of Plasticity*, 12(6), 805-842.

Bozorgnia, Y., and Bertero, V. (2004). *Earthquake Engineering: From Engineering Seismology to Performance-Based Engineering*. CRC Press, Boca Raton, FL.

Bozzo, L., and Barbat, A. H. (1995). "Non-linear response of structures with sliding base isolation." *Journal of Structural Control*, 2, 59-77.

Brailovski, V., Prokoshkin, S., Terriault, P., and Trochu, F. (2003). *Shape memory alloys: Fundamentals, modelling and applications*. Ecole de technologie superieure, Montreal, Que., Canada.

Brinson, L. C. (1993). "One-dimensional constitutive behavior of shape memory alloys: thermomechanical derivation with non-constant material functions and redefined martensite internal variable." *Journal of Intelligent Material Systems and Structures*, 4, 229-241.

Bruneau, M. (1998). "Performance of steel bridges during the 1995 Hyogoken-Nanbu (Kobe, Japan) earthquake--a North American perspective." *Engineering Structures*, 20(12), 1063-1078.

Buragohain, M. and Mahanta, C. (2008). "A novel approach for ANFIS modelling based on full factorial design." *Applied Soft Computing*, 8(1), 609-625.

Cardone, D., Dolce, M., Nigro, D., and Ponzo, F. C. (2006). "The behaviour of SMA isolation systems in a full-scale release tests." *Journal of Earthquake Engineering*, 10(6), 815-842.

Casciati, F., and Faravelli, L. (2004). "Experimental characterization of a Cu-based shape memory alloy toward its exploitation in passive control devices." *Journal of Physics IV*, 115, 299-306.

Casciati, F., and Faravelli, L. (2009). "A passive control device with SMA components: from the prototype to the model." *Structural Control and Health Monitoring*, 16, 751-765.

Casciati, F., Faravelli, L. and Al Saleh. R. (2009). "An SMA passive device proposed within the highway bridge benchmark." *Structural Control and Health Monitoring*, 16, 657-667.

Casciati, F., Faravelli, L., and Fuggini, C. (2008). "Cable vibration mitigation by added SMA wires." *Acta Mechanica*, 195, 141-155.

Casciati, S., and Marzi, A. (2010). "Experimental studies on the fatigue life of shape memory alloy bars." *Smart Structures and Systems*, 6(1), 73-85.

Casciati, F., and van der Eijk, C. (2008). "Variability in mechanical properties and microstructure characterization of CuAlBe shape memory alloys for vibration mitigation." *Smart Structures and Systems*, 4(2), 103-122.

Chang, B. C., Shaw, J. A., and Iadicola, M. A. (2006). "Thermodynamics of shape memory alloy wire: modeling, experiments, and application." *Continuum Mechanics and Thermodynamics*, 18, 83-118.

Chapman, M. C. (1999). "On the use of elastic input energy for seismic hazard analysis." *Earthquake Spectra*, 15(4), 607-635.

Chen, W., and Song, B. (2006). "Temperature dependence of a NiTi shape memory alloy's superelastic behavior at a high strain rate." *Journal of Mechanics of Materials and Structures*, 1(2), 339-356.

Choi, E., Lee, D. H., and Choei, N. Y. (2009). "Shape memory alloy bending bars as seismic restrainers for bridges in seismic areas." *International Journal of Steel Structures*, 9(4), 261-273.

Choi, E., Nam, T. H., Oh, J. T., and Cho, B. S. (2006). "An isolation bearing for highway bridges using shape memory alloys." *Material Science and Engineering A* 438-440, 1081-1084.

Churchill, C. B., Shaw, J. A., and Iadicola, M. A. (2009). "Tips and tricks for characterizing shape memory alloy wire: part 2—fundamental isothermal responses." *Experimental Techniques*, 33(1), 51-62.

Clark, P. W., Aiken, I. D., Kelly J. M., Higashino, M., and Krumme, R. C. (1995). "Experimental and analytical studies of shape memory alloy damper for structural control." *Proceedings of SPIE*, 2445, 241-251.

Constantinou, M., Mokha, A., and Reinhorn, A. (1990). "Teflon bearing in base isolation II: Modeling." *Journal of Structural Engineering*, 116(2), 455-74.

Dayananda, G. N., and Rao, M. S. (2008). "Effect of strain rate on properties of superelastic NiTi thin wires." *Materials Science and Engineering A* 486, 96-103.

Deb, K., Pratap, A., Agrawal, S., and Meyarivan, T. (2002). "A fast elitist non-dominated sorting genetic algorithm for multi-objective optimization: NSGA-II." *IEEE Transactions on Evolutionary Computation*, 6(2), 182–197.

Deb, S. K. (2004). "Seismic base isolation – An overview." *Current Science*, 87(10):, 426-1430.

DesRoches, R., McCormick, C., and Delemont, M. (2004). "Cyclic properties of superelastic shape memory alloy wires and bars." *Journal of Structural Engineering*, 130(1), 38-46.

DesRoches, R., and Smith, B. (2004). "Shape memory alloys in seismic resistant design and retrofit: a critical review of their potential and limitations." *Journal of Earthquake Engineering*, 8(3), 415-429.

DesRoches, R., Taftali, B., and Ellingwood, B. R. (2010). "Seismic performance assessment of steel frames with shape memory alloy connections, part I – analysis and seismic demands." *Journal of Earthquake Engineering*, 14, 471-486.

Dicleli, M. (2007). "Supplemental elastic stiffness to reduce isolator displacements for seismic-isolated bridges in near-fault zones." *Engineering Structures*, 29, 763-775.

Dolce, M., and Cardone, D. (2001). "Mechanical behavior of shape memory alloys for seismic applications 2. Austenite NiTi bars subjected to tension." *International Journal of Mechanical Sciences*, 43, 2657-2677.

Dolce M., Cardone D., and Marnetto R. (2000). "Implementation and testing of passive control devices based on shape memory alloys." *Earthquake Engineering and Structural Dynamics*, 29, 945-968.

Dolce, M., Cardone, D., Croatto, F. (2005a). "Frictional behavior of Steel-PTFE interfaces for seismic isolation." *Bulletin of Earthquake Engineering*, 3, 75-99.

Dolce, M., Cardone D., Ponzo F. C., and Valente C. (2005b). "Shaking table tests on reinforced concrete frames without and with passive control systems." *Earthquake Engineering and Structural Dynamics*, 34, 1687-1717.

Dolce, M., Cardone, D., and Palermo, G. (2007a). "Seismic isolation of bridges using isolation systems based on flat sliding bearings." *Bulletin of Earthquake Engineering*, 5, 491-509.

Dolce, M., Cardone, D., and Ponzo, F. C. (2007b). "Shaking-table tests on reinforced concrete frames with different isolation systems." *Earthquake Engineering and Structural Dynamics*, 36, 573-596.

Ellingwood, B. R., Taftali, B., and DesRoches, R. (2010). "Seismic performance assessment of steel frames with shape memory alloy connections, part II – probabilistic seismic demand assessment." *Journal of Earthquake Engineering*, 14, 641-645.

Erkus, B., Abe, M., and Fujino, Y. (2002). "Investigation of semi-active control for seismic protection of elevated highway bridges." *Engineering Structures*, 24, 281-293.

Fajfar, P., and Vidic, T. (1994). "Consistent inelastic design spectra: hysteretic and input energy." *Earthquake Engineering and Structural Dynamics*, 23, 523–537.

Faravelli, L., Fuggini, C., and Ubertini F. (2010). "Toward a hybrid control solution for cable dynamics: Theoretical prediction and experimental validation." *Structural Control and Health Monitoring*, 17, 386-403.

Fugazza, D. (2005). *Use of shape-memory alloy devices in earthquake engineering: Mechanical properties, advanced constitutive modeling and structural applications*. Ph.D. dissertation. European School for Advanced Studies in Reduction of Seismic Risk. Pavia, Italy.

Gall, K., Sehitoglu, H., Anderson, R., Karaman, I., Chumlyakov, Y.I., Kireeva, I.V. (2001). "On the mechanical behavior of single crystal NiTi shape memory alloys and related polycrystalline phenomenon." *Material Science and Engineering A*, 317, 85-92.

Goo, B. C., and Lexcellent, C. (1997). "Micromechanics based Modeling of two-way memory effect of a single crystalline shape memory alloy." *Acta Metallurgica*, 45, 727-737.

Graesser, E. J., and Cozzarelli, F. A. (1991) "Shape-memory alloys as new materials for aseismic isolation." *Journal of Engineering Mechanics*, 117, 2590-2608.

Guo, A., Li, Z., Li, H., and Ou, J. (2009). "Experimental and analytical study on pounding reduction of base-isolated highway bridges using MR dampers." *Earthquake Engineering and Structural Dynamics*, 38(11), 1307-1333.

Hall, G. J., and Govindjee, S. (2002). "Application of a partially relaxed shape memory free energy function to estimate the phase diagram and predict global microstructure evolution." *Journal of the Mechanics and Physics of Solids*, 50, 501-530.

Han, Y. H., Li, Q.S., Li, A.Q., Leung, A. Y. T., and Lin, P.H. (2003). "Structural vibration control by shape memory alloy damper." *Earthquake Engineering and Structural Dynamics*, 32, 483-494.

Han, Y. L., Xing, D. J., Xiao E. T., and Li, A. Q. (2005). "NiTi-wire shape memory alloy dampers to simultaneously damp tension, compression, and torsion." *Journal of Vibration and Control*, 11(8), 1067-1084.

Hancock, J., Bommer, J. J., and Stafford, P. J. (2008). "Numbers of scaled and matched accelerograms required for inelastic dynamic analyses." *Earthquake Engineering and Structural Dynamics*, 37, 1585-1607.

Hancock, J., Watson-Lamprey, J., Abrahamson, N. A., Bommer, J. J., Markatis, A., McCoy, E., and Mendis, R. (2006). "An improved method of matching response spectra of recorded earthquake ground motion using wavelets." *Journal of Earthquake Engineering*, Special Issue 1, 10, 67-89.

Higashino, M., and Aizawa, S. (1996). "Experimental and analytical studies of structural control system using shape memory alloy." *Second International Workshop on Structural Control*, Hong Kong, 221-232.

Housner, G. W. (1956). "Limit design of structures to resist earthquakes." *Proceedings of the 1st World Conference on Earthquake Engineering*, Berkeley, CA.

Housner, G. W., and Thiel, C. C., Jr. (1995). "The continuing challenge: report on the performance of state bridges in the Northridge earthquake." *Earthquake Spectra* 1995; 11(4): 607-636

Hsu, Y. T., and Fu, C. C. (2004). "Seismic effect on highway bridges in Chi Chi earthquake." *Journal of Performance of Constructed Facilities*, 18(1), 47-53.

IBC. (2000) *International building code*. International Code Council: Falls Church, VA.

Ibrahim, R. A. (2008). "Recent advances in nonlinear passive vibration isolators." *Journal of Sound and Vibration*, 314, 371–452.

Iemura, H., and Pradono, M. H. (2005). "Simple algorithm for semi-active seismic response control of cable-stayed bridges." *Earthquake Engineering and Structural Dynamics*, 34(4), 409-423.

Iemura, H., Taghikhany, T., and Sarvesh, K. J., 2007. "Optimum design of resilient sliding isolation system for seismic protection of equipments." *Bulletin of Earthquake Engineering*, 5, 85-103.

Iervolino, I., Maddaloni, G., and Cosenza, E. (2009). "A note on selection of time-histories for seismic analysis of bridges in Eurocode 8." *Journal of Earthquake Engineering*, 13(8), 1125- 1152.

Iervolino, I., and Manfredi, G. (2009). "A review of ground motion record selection strategies for dynamic structural analysis." *CISM International Centre for Mechanical Sciences*, 502, 131-163.

Ikeda, T., Nae, F. A., Naito, H. and Matsuzaki, Y. (2004). "Constitutive model of shape memory alloys for unidirectional loading considering inner hysteresis loops." *Smart Materials and Structures*, 13, 916–925.

Jang, J. S. R. (1993). "ANFIS: Adaptive-network-based fuzzy inference system." *IEEE Trans Syst, Man, Cybernet*, 23(3), 665–85.

Jang, J. S. R. (1996). "Input selection for ANFIS learning." *Proceedings of the IEEE International Conference on Fuzzy Systems*, 2, 1493-1499.

Jang, J. S. R., Sun, C., and Mizutani, E. (1997). *Neuro-fuzzy and soft computing: a computational approach to learning and machine intelligence*. Prentice Hall, Upper Saddle River, NJ.

Jangid R. S. (2005a). "Computational numerical models for seismic response of structures isolated by sliding sytems." *Structural Control and Health Monitoring*, 12, 117-137.

Jangid, R. S. (2005b). "Optimum friction pendulum system for near-fault motions." *Engineering Structures*, 27, 349-359.

Jangid, R. S., 2007. "Optimum lead-rubber isolation bearings for near-fault motions." *Engineering Structures*, 29, 2503-2513.

Jangid, R. S., and Kelly, J. M. (2001). "Base isolation for near-fault motions." *Earthquake Engineering and Structural Dynamics*, 30, 691-707.

Janke, L., Czaderski, M., Motavalli, M., and Ruth, J. (2005). "Application of shape memory alloys in civil engineering structures – Overview, limits and new ideas." *Materials and Structures*, 38(279), 578-592.

Johnson, R., Padgett, J. E., Maragakis, M. E., DesRoches, R., and Saiidi, M. S. (2008). "Large scale testing of nitinol shape memory alloy devices for retrofitting of bridges." *Smart Materials and Structures*, 17, 1-10.

Kalkan, E., and Kunnath, S. H. (2008). "Relevance of absolute and relative energy content in seismic evaluation of structures." *Advances in Structural Engineering*, 11, 1-18.

Krumme, R., Hayes, J., and Sweeney, S. (1995). "Structural damping with shape-memory alloys: one class of devices." *Proceedings of SPIE*, 2445, 225-240.

Lafortune, P., McCormick, J., DesRoches, R., and Terriault, P. (2007). "Testing of superelastic recentering pre-strained braces for seismic resistant design." *Journal of Earthquake Engineering*, 11, 383-399.

Lagoudas, D. C. (2008). *Shape memory alloys: modeling and engineering applications*. Springer, New York.

Lee, T. Y., and Kawashima, K. (2007). "Semiactive control of nonlinear isolated bridges with time delay." *Journal of Structural Engineering*, 133(2), 235-241.

Levitas, V. I., Idesman, A. V., Stein, E., Spielfeld, J. and Hornbogen, E. (1998). "A simple micromechanical model for pseudoelastic behavior of CuZnAl alloy." *Journal of Intelligent Material Systems and Structures*, 5, 324-334.

Li, H., Liu, M., and Ou, J. (2004). "Vibration mitigation of a stay cable with one shape memory alloy damper." *Structural Control and Health Monitoring*, 11, 21-36.

Li, H., Mao, C. X., and Qu, J. P. (2008). "Experimental and theoretical study on two types of shape memory alloy devices." *Earthquake Engineering and Structural Dynamics*, 37 407-426.

Liang, C., and Rogers, C. A. (1990). "One-dimensional thermo mechanical constitutive relations for shape memory material." *Journal of Intelligent Material Systems and Structures*, 1, 207–234.

Liao, W. I., Loh, C. H., and Lee, B. H. (2004). "Comparison of dynamic response of isolated and non-isolated continuous girder bridges subjected to near-fault ground motions." *Engineering Structures*, 26, 2173–2183.

Liu, M., Li, H., Song, G., and Ou, J. (2007). "Investigation of vibration mitigation of stay cables incorporated with superelastic shape memory alloy dampers." *Smart Materials and Structures*, 16, 2202-2213.

Ma, H., and Cho, C. (2008). "Feasibility study on a superelastic SMA damper with re-centring capability." *Materials Science and Engineering A*, 473, 290-296.

Ma, H., Wilkinson, T., and Cho, C. (2007). "Feasibility study on a self-centering beam-to-column connection by using the superelastic behavior of SMAs." *Smart Material and Structures*, 16, 1555-1563.

Makris, N., and Zhang, J. (2004). "Seismic response analysis of a highway overcrossing equipped with elastomeric bearings and fluid dampers." *Journal of Structural Engineering*, 130(6), 830-845.

Malecot, P., Lexcellent, C., Foltete, E., and Collet, M. (2006). "Shape memory alloys cyclic behavior: experimental study and modeling." *Journal of Engineering Materials and Technology*, 128, 335-345.

Malhotra, P. K. (2003). "Strong-motion records for site-specific analysis." *Earthquake Spectra*, 19(3), 557-578.

Marano, G. C., and Greco, R. (2003). "Efficiency of base isolation systems in structural seismic protection and energetic assessment." *Earthquake Engineering and Structural Dynamics*, 32, 1505-1531.

McCormick, J., DesRoches, R., Fugazza, D., and Auricchio, F. (2007a). "Seismic assessment of concentrically-braced steel frames using shape memory alloy braces." *Journal of Structural Engineering*, 133(6), 863-870.

McCormick, J., Tyber, J., DesRoches, R., Gall, K., and Maier, H.J. (2007b). "Structural engineering with NiTi. II: Mechanical behavior and scaling." *Journal of Engineering Mechanics*, 133(9), 1019-1029.

McGavin, G., and Guerin, G. (2002). "Real-time seismic damping and frequency control of steel structures using Nitinol wire." *Proceedings of SPIE*, 4696, 176-184.

Montecinos, S., Moroni, M. O., and Sepúlveda A. (2006). "Superelastic behaviour and damping capacity of CuAlBe alloys." *Materials Science and Engineering A* 419(1–2), 91–97.

Moroni, M. O., Saldivia, R., Sarrazin, M., and Sepulveda, A. (2002). "Damping characteristics of a CuZnAlNi shape memory alloy." *Materials Science and Engineering A* 335, 313-319.

Motahari, S. A., and Ghassemieh, M. (2007). "Multilinear one-dimensional shape memory material model for use in structural engineering applications." *Engineering Structures*, 29, 904-913.

Naeim, F., and Lew, M. (1994). "Deficiencies of design-spectrum compatible accelerograms." *Structural Design of Tall Buildings*, 3, 275-283.

Nguyen, H.T., Nadipuram, R.P., Walker, C.L., and Walker, E.A. (2003). *A First Course in Fuzzy and Neural Control*. Chaoman & Hall/CRC, Boca Raton, FL.

Ocel, J., DesRoches, R., Leon, R. T., Hess, W. G., Krumme, R., Hayes, J. R., and Sweeney, S. (2004). "Steel beam-column connections using shape memory alloys." *Journal of Structural Engineering*, 130(5), 732–740.

Ordaz, M., Huerta, B., and Reinoso, E. (2003). "Exact computation of input-energy spectra from Fourier amplitude spectra." *Earthquake Engineering and Structural Dynamics*, 32(4), 597-605.

Ozbulut, O. E., and Hurlebaus, S. (2010a). "Neuro-fuzzy modeling of temperature- and strain-rate-dependent behavior of NiTi shape memory alloys for seismic applications." *Journal of Intelligent Materials and Structures*, 21, 837-849.

Ozbulut, O. E., and Hurlebaus, S. (2010b). "Optimal design of superelastic-friction base isolators for seismic protection of highway bridges against near-field earthquakes." *Earthquake Engineering and Structural Dynamics*, doi:10.1002/eqe.1022.

Ozbulut, O. E., and Hurlebaus, S. (2010c). "Performance evaluation of shape memory alloy-based rubber isolation systems for seismic response mitigation of bridges." *Proceedings of SPIE*, Vol. 7647, 76473X, San Diego, CA.

Ozbulut, O. E., and Hurlebaus, S. (2010d). "A comparative performance assessment of superelastic-friction base isolators for seismic protection of bridge structures." *Proceedings of the 5th World Conference on Structural Control and Monitoring*, Tokyo, Japan.

Ozbulut, O. E., and Hurlebaus, S. (2010e). "Evaluation of the performance of a sliding-type base isolation system with a NiTi shape memory alloy device considering temperature effects." *Engineering Structures*, 32, 238-249.

Ozbulut, O. E., Mir, C., Moroni, M. O., Sarrazin, M., and Roschke, P. N. (2007). "A fuzzy model of superelastic shape memory alloys for vibration control in civil engineering applications." *Smart Materials and Structures*, 16, 818-829.

Ozbulut, O. E., and Roschke, P. (2010). "GA-based optimum design of a shape memory alloy device for seismic response mitigation." *Smart Materials and Structures*, 19, 065004.

Padgett, J. E., DesRoches, R., and Ehlinger, R. (2009). "Experimental response modification of a four-span bridge retrofit with shape memory alloys." *Structural Control and Health Monitoring*, doi: 10.1002/stc.351.

Panchal, V. R., and Jangid, R. S. (2008). "Variable friction pendulum system for seismic isolation of liquid storage tanks." *Nuclear Engineering and Design*, 238, 1304-1315.

Park, J. G., and Otsuka, H. (1999). "Optimal yield level of bilinear seismic isolation devices." *Earthquake Engineering and Structural Dynamics*, 28, 941-955.

Patoor, E., Eberhardt, A. and Berveiller, M. (1998). "Micromechanical modeling of shape memory alloys behavior." *Archives of Mechanics*, 40, 775-794.

Piedboeuf, M. C., Gauvin, R., and Thomas, M. (1998). "Damping behavior of shape memory alloys: strain amplitude, frequency, and temperature effects." *Journal of Sound and Vibration*, 214(5), 885-901.

Prahlad, H., and Chopra, I. (2003). "Development of a strain-rate dependent model for uniaxial loading of SMA wires." *Journal of Intelligent Material Systems and Structures*, 14, 429-442.

Preumont, A. (1984). "The generation of spectrum compatible accelerograms for the design of nuclear power plants." *Earthquake Engineering and Structural Dynamics*, 12, 481-97.

Qiang, H., Xiuli, D., Jingbo, L., Zhongxian, L., Liyun, L., and Jianfeng, Z. (2009). "Seismic damage of highway bridges during the 2008 Wenchuan earthquake." *Earthquake Engineering and Engineering Vibration*, 8, 263-273.

Ren, W., Li, H., and Song, G. (2007). "A one-dimensional strain-rate-dependent constitutive model for superelastic shape memory alloys." *Smart Materials Structures*, 16, 191-197.

Roussis, P. C., Constantinou, M. C., Erdik, M., Duruka, E., and Dicleli, M. (2003). "Assessment of performances of seismic isolation system of Bolu viaduct." *Journal of Bridge Engineering*, 8(4), 182-190.

Saadat, S., Noori, M., Davoodi, H., Hou, Z., Suziki, Y., and Masuda, A. (2001). "Using NiTi SMA tendons for vibration control of coastal structures." *Smart Material and Structures*, 10, 695-704.

Saiidi, M., O'Brien, M., and Sadrossadat-Zadeh, M. (2009). "Cyclic response of concrete bridge columns using superelastic nitinol and bendable concrete." *ACI Structural Journal*, 106, 69-77.

Saiidi, M., and Wang, H. (2006) "An exploratory study of seismic response of concrete columns with shape memory alloys reinforcement." *ACI Structural Journal*, 103, 436-443.

Salichs, J., Hou. Z., and Noori M. (2001). "Vibration suppression of structures using passive shape memory alloy energy dissipation devices." *Journal of Intelligent Material Systems and Structures*, 12, 671-680.

Sayani, P. J., and Ryan, K. L. (2009). "Comparative evaluation of base-isolated and fixed-base buildings using a comprehensive response index." *Journal of Structural Engineering*, 135(6), 698-707.

Shahin, A., Alu, R., Meckl, P. H., and Jones, J. D. (1997). "Modeling of SMA tendons for active control of structures." *Journal of Intelligent Material Systems and Structures*, 8(1), 51-70.

Sharabash, A. M., and Andrawes, B. O. (2009). "Application of shape memory alloy dampers in the seismic control of cable-stayed bridges." *Engineering Structures*, 31(2), 607-616.

Shen, J., Tsai, M. H., Chang, K. C., and Lee, G. C. (2004). "Performance of a seismically isolated bridge under near-fault earthquake ground motions." *Journal of Structural Engineering*, 130, 861-868.

Sepulveda, J., Boroschek, R., Herrera, R., Moroni, O., and Sarrazin, M. (2008). "Steel beam–column connection using copper-based shape memory alloy dampers." *Journal of Constructional Steel Research*, 64, 429-435.

Soneji, B. B., and Jangid, R. S. (2007). "Passive hybrid systems for earthquake protection of cable-stayed bridge." *Engineering Structures*, 29(1), 57-70.

Song, M., Ma, N., and Li, H.N. (2006). "Applications of shape memory alloys in civil structures." *Engineering Structures*, 28, 1266-1274.

Soul, H., Isalgue, A., Yawny, A., Torra, V., and Lovey, F. C. (2010). "Pseudoelastic fatigue of NiTi wires: frequency and size effects on damping capacity." *Smart Materials and Structures*, 19, 085006.

Speicher, M., Hodgson, D. E., DesRoches, R., and Leon, R. T. (2009). "Shape memory alloy tension/compression device for seismic retrofit of buildings." *Journal of Materials Engineering and Performance*, 18, 746-753.

Suduo, X., and Xiongyan, L. (2007). "Control devices incorporated with shape memory alloy." *Earthquake Engineering and Engineering Vibration*, 6(2), 159-169.

Sun, Q. P., and Hwang, K. C. (1993). "Micromechanics modelling for the constitutive behavior of polycrystalline shape memory alloys -- I Derivation of general relations, *Journal of the Mechanics and Physics of Solids*, 41(1), 1-17.

Sun, S., and Rajapakse, R. K. N. D. (2003). "Simulation of pseudoelastic behavior of SMA under cyclic loading." *Computational Material Science*, 28, 663-674.

Sutou, Y., Omori, T., Kainuma, R., and Ishida K. (2008). "Ductile Cu–Al–Mn based shape memory alloys: general properties and applications." *Material Science and Technology*, 24(8), 896-901.

Takagi, T., and Sugeno, M. (1983). ''Derivation of fuzzy control rules from human operator's control actions.'' In: *Proceedings of the IFAC Symposium on Fuzzy Information, Knowledge Representation and Decision Analysis*, July, Marseille, France, pp. 55-60.

Takewaki, I. (2004). "Bound of earthquake input energy." *Journal of Structural Engineering*, 130, 1289-1297.

Takewaki, I., and Fujita, K. (2009). "Earthquake input energy to tall and base-isolated buildings in time and frequency dual domains." *Structural Design of Tall and Special Buildings*, 18, 589-606.

Tamai, H., and Kitagawa, Y. (2002). "Pseudoelastic behavior of shape memory alloy wire and its application to seismic resistance member for building." *Computational Material Science*, 25, 218-227.

Tanaka, Y., Himuro, Y., Kainuma, R., Sutou, Y., Omori, T., and Ishida, K. (2010). "Ferrous polycrystalline shape-memory alloy showing huge superelasticity." *Science*, 327, 1488-1490.

Tobushi, H., Shimeno, Y., Hachisuka, T., and Tanaka, K. (1998). "Influence of strain rate on superelastic properties of TiNi shape memory alloy." *Mechanics of Materials*, 30(2), 141-150.

Torra, V., Isalgue, A., Auguet, C., Carreras, G., Lovey, F.C., Soul, H., and Terriault, P. (2009). "Damping in civil engineering using SMA. The fatigue behavior and stability of CuAlBe and NiTi alloys." *Journal of Materials Engineering and Performance*, 18, 738-745.

Torra, V., Isalgue, A., Lovey, F. C., Martorell, F., Molina, F. J., Sade, M. and Tachorie, H. (2004). "Shape memory alloys: From the physical properties of metastable phase transitions to dampers for civil engineering applications." *Journal of Physics IV*, 113, 85-90.

Torra, V., Isalgue, A., Martorell, F., Terriault, P. and Lovey, F. C. (2007). "Built in dampers for family homes via SMA: An ANSYS computation scheme based on mesoscopic and microscopic experimental analyses." *Engineering Structures*, 29(8), 1889-1902.

Tyler, R. G. (1991). "Rubber bearings in base-isolated structures—a summary paper." *Bulletin of the New Zealand National Society for Earthquake Engineering*, 243, 251-274.

Uang, C. M., and Bertero, V. V. (1990). "Evaluation of seismic energy in structures." *Earthquake Engineering and Structural Dynamics*, 19, 77–90.

Usman, M., Sung, S. H., Jang, D. D., Jung, H. J., and Koo, J. H. (2009). "Numerical investigation of smart base isolation system employing MR elastomer." *Journal of Physics: Conference Series*, 149, 012099.

van de Lindt, J. W., and Potts, A. (2008). "Shake table testing of a superelastic shape memory alloy response modification device in a wood shearwall." *Journal of Structural Engineering*, 134(4), 1343-1352.

Wang, Y. P., Chung, L. L., and Liao, W. H. (1998). "Seismic response analysis of bridges isolated with friction pendulum bearings." *Earthquake Engineering and Structural Dynamics*, 27, 1069-1093.

Wilde, K., Gardoni, P., and Fujino, Y. (2000). "Base isolation system with shape memory alloy device for elevated highway bridges." *Engineering Structures*, 22, 222-229.

Wolons, D., Gandhi, F., and Malovrah, B. (1998). "Experimental investigation of the pseudoelastic hysteresis damping characteristics of shape memory alloy wires." *Journal of Intelligent Material Systems and Structures*, 9, 116-126.

Wu, K., Yang, F., Pu, Z., and Shi, J. (1996). "The effect of strain rate on detwinning and superelastic behavior of NiTi shape memory alloys." *Journal of Intelligent Material Systems and Structures*, 7, 138-144.

Yang, C. W., DesRoches, R., and Leon, R. T. (2010). "Design and analysis of braced frames with shape memory alloy and energy-absorbing hybrid devices." *Engineering Structures*, 32, 498-507.

Yoshioka, H., Ramallo, J. C., and Spencer, B. F. (2002). "Smart base isolation strategies employing magnetorheological dampers." *Journal Engineering Mechanics*, 128, 540-551.

Youssef, M. A., Alam, M. S., and Nehdi, M. (2008). "Experimental investigation on the seismic behaviour of beam-column joints reinforced with superelastic shape memory alloys." *Journal of Earthquake Engineering*, 12, 1205-1222.

Zhang, Y., Camilleri, J. A., and Zhu, S. (2008). "Mechanical properties of superelastic Cu–Al–Be wires at cold temperatures for seismic protection of bridges." *Smart Materials and Structures*, 17, 025008.

Zhang, Y., and Zhu, S. (2007). "Shape memory alloy-based reusable hysteretic damper for seismic hazard mitigation." *Smart Materials Structures*, 16, 1603–1613.

Zhu, S., and Zhang, Y. (2007a). "A thermomechanical constitutive model for superelastic SMA wire with strain-rate dependence." *Smart Materials and Structures*, 16, 1696-1707.

Zhu, S., and Zhang, Y. (2007b). "Seismic behaviour of self-centring braced frame buildings with reusable hysteretic damping brace." *Earthquake Engineering and Structural Dynamics*, 36, 1329-1346.

Zhu, S., and Zhang, Y. (2008). "Seismic analysis of concentrically braced frame systems with self-centering friction damping braces." *Journal of Structural Engineering*, 134(1), 121-131.

Zuo, X. B., and Li, A.Q. (2009). "Numerical and experimental investigation on cable vibration mitigation using shape memory alloy damper." *Structural Control and Health Monitoring*, doi: 10.1002/stc.354

Zuo, X. B., Li, A. Q., and Chen, Q. F. (2008). "Design and analysis of a superelastic SMA damper." *Journal of Intelligent Material Systems and Structures*, 19(6), 631-639.

VITA

Osman Eser Ozbulut received his Bachelor of Science degree in civil engineering from Istanbul Technical University in May 2005. He enrolled in the structural engineering program at the Zachry Department of Civil Engineering, Texas A&M University, in August 2005, and obtained his Masters of Science degree in August 2007. He received his Doctor of Philosophy degree in structural engineering from Texas A&M University in December 2010.

Osman Ozbulut may be reached at Zachry Department of Civil Engineering, 3136 TAMU, College Station, TX 77843. His e-mail address is ozbulute@yahoo.com.